

Structured Distributions of Gas and Solids in Protoplanetary Disks

Jaehan Bae

University of Florida
Carnegie Institution for Science

Andrea Isella

Rice University

Zhaohuan Zhu

University of Nevada, Las Vegas

Rebecca Martin

University of Nevada, Las Vegas

Satoshi Okuzumi

Tokyo Institute of Technology

Scott Suriano

Union College
SUNY Corning Community College
The University of Tokyo

Recent spatially-resolved observations of protoplanetary disks revealed a plethora of substructures, including concentric rings and gaps, inner cavities, misalignments, spiral arms, and azimuthal asymmetries. This is the major breakthrough in studies of protoplanetary disks since *Protostars and Planets VI* and is reshaping the field of planet formation. However, while the capability of imaging substructures in protoplanetary disks has been steadily improving, the origin of many substructures are still largely debated. The structured distributions of gas and solids in protoplanetary disks likely reflect the outcome of physical processes at work, including the formation of planets. Yet, the diverse properties among the observed protoplanetary disk population, for example, the number and radial location of rings and gaps in the dust distribution, suggest that the controlling process may differ between disks and/or the outcome may be sensitive to stellar or disk properties. In this review, we (1) summarize the existing observations of protoplanetary disk substructures collected from the literature; (2) provide a comprehensive theoretical review of various processes proposed to explain observed protoplanetary disk substructures; (3) compare current theoretical predictions with existing observations and highlight future research directions to distinguish between different origins; and (4) discuss implications of state-of-the-art protoplanetary disk observations to protoplanetary disk and planet formation theory.

1. Introduction

Since the modern planet formation theory was established (e.g., *Safronov 1972*), many physical processes associated with planet formation (including protoplanetary disk turbulence, dust dynamics, planetesimal formation, assembly and evolution of planetary cores) evolved to active research fields by their own and have been reviewed through previous *Protostars and Planets* series (e.g., *Helled et al. 2014*; *Johansen et al. 2014*; *Raymond et al. 2014*; *Testi et al. 2014*; *Turner et al. 2014*, in *Protostars and Planets*

VI). However, despite the large amount of theoretical efforts, the planet-forming environments and processes have been largely unconstrained by observations until recently.

Over the last few decades, more than 5,000 exoplanets have been discovered¹, and we now know that the solar system planets are not the only planets in our galaxy. Interestingly, a large fraction of the observed exoplanet population has very distinct properties compared with those of solar system planets, potentially suggesting that the typical

¹<https://exoplanetarchive.ipac.caltech.edu/>

planet forming environment may be different from what we had 4.6 billion years ago in the solar nebula. In order to better understand the diversity in the exoplanet population and the potential uniqueness of the solar system, it is crucial to study protoplanetary disks – the birthplace of planets.

With the advent of the state-of-the-art observing facilities, including the Atacama Large Millimeter/submillimeter Array (ALMA) and ground-based telescopes equipped with extreme adaptive optics, we now have the capability of spatially resolving protoplanetary disks at as fine as a $0''.01$ angular resolution, corresponding to a few astronomical unit (au) in linear scale for the disks in nearby star-forming regions. At the time *Protostars and Planets VI* was written, radio interferometric observations could achieve a $\gtrsim 0''.2$ angular resolution with the Submillimeter Array, Combined Array for Research in Millimeter-wave Astronomy, and Plateau de Bure Interferometer (see e.g., [Dutrey et al. 2014](#); [Espaillat et al. 2014](#); [Testi et al. 2014](#) in *Protostars and Planets VI*), so we now have about an order of magnitude better resolving power than back then. Notably, the observations from the 2014 ALMA Long Baseline Campaign revealed multiple sets of concentric bright rings and dark gaps in the protoplanetary disk surrounding the young star HL Tau ([ALMA Partnership et al. 2015](#)). It has long been suggested that protoplanetary disks have structures, inferred based on the spectral energy distribution (SED; [Strom et al. 1989](#), see also review by [Espaillat et al. 2014](#) in *Protostars and Planets VI*) and images taken with ground-based telescopes, the Hubble Space Telescope (e.g., [Grady et al. 1999](#)), and pre-ALMA radio interferometers (e.g., [Andrews et al. 2009](#)). However, the ALMA observation of the HL Tau disk was the first time that au-scale fine structures were imaged in protoplanetary disks. Since then, high-resolution observations have revealed a myriad of disk structures, including rings and gaps, spirals, and crescents which, collectively, are commonly referred to as *protoplanetary disk substructures*.

One of the reasons why protoplanetary disk substructures have been drawing large attention from the community is that their presence could be related to planet formation, although whether substructures are the cause or effect of planet formation is unclear at the time of writing this Chapter (we further discuss this point in Section 10). In either case, the increasingly powerful observational facilities and techniques have led us to the point where planet formation theory can be finally tested by observations. Several Chapters in this book are dedicated to recent high-resolution observations of protoplanetary disks ([Benisty et al.](#), [Pinte et al.](#)) and theoretical studies of protoplanetary disks and planet formation therein ([Drazkowska et al.](#), [Lesur et al.](#), [Paardekooper et al.](#)). In this Chapter, we aim to connect observations and theory, by comparing existing observational data with current theoretical predictions for disk substructures.

This Chapter is organized as follows. In Section 2, we provide an overview of recent high-resolution observations of protoplanetary disks. We provide basic statistics and

discuss whether or not we find any correlation between substructure properties and stellar/disk properties. As we will show in Section 2, a large fraction of substructures observed to date have been detected in radio continuum and/or optical/near-infrared (NIR) scattered light observations, both of which probe dust grains in the disks. When interpreting disk substructures, it is important to keep in mind that the spatial distribution of the gas, which contains about 99% of the total disk mass, and that of the dust can differ due to the aerodynamic drag that exerts on the dust. We discuss the coupling between the gas and the dust in Section 3. We then review various substructure-forming mechanisms from Section 4 to Section 8. There are more than 20 mechanisms that we review in this Chapter, and we group them into hydrodynamic processes (Section 4), magnetohydrodynamic processes (Section 5), tidal interactions with perturbers (Section 6), disk self-gravity and the effects it has on other substructure-forming processes (Section 7), and processes induced by dust particles (Section 8). In each of these sections, we follow a homogenized structure (when applicable) such that we first introduce how each mechanism operates, then describe in which regions of protoplanetary disks it is expected to operate, and finally summarize the properties of substructures it creates. After we have discussed the substructure-forming mechanisms, in Section 9 we compare the properties of the substructures predicted from theories and numerical simulations with those from observations, discuss potential origins of observed disk substructures, and provide future directions to distinguish between different origins. Finally, we discuss the implications of disk substructures to protoplanetary disk and planet formation theory in Section 10 and conclude the Chapter in Section 11.

2. Overview of Observed Protoplanetary Disk Substructures

2.1. Observational Primer

Assuming that protoplanetary disks inherit their composition from the parent molecular clouds, about 99% of their mass is composed of gas, while the remaining 1% is in the form of refractory material, i.e., solid particles. Of the gas mass, about 70% is in the form of hydrogen (both atomic and molecular), about 28% is composed of helium, and only about 2% is composed of heavier elements. However, at densities and temperatures that are typical for protoplanetary disks, hydrogen and helium are hardly observable and our knowledge of protoplanetary disks must therefore rely on observations of much rarer components such as dust particles and tracer molecules.

For dust particles, thermal and scattered continuum emission at a wavelength of λ are dominated by grains with a size $a \sim \lambda/2\pi$. Consequently, optical/near-infrared observations mainly probe sub-micrometer particles, while mm and cm-wave observations probe sand-sized and pebble-size solids. This characteristic, coupled to the fact that the absorption and scattering opacity of dust

grains strongly depends on the grain size (see, e.g., [Draine 2016](#)), results in a strong wavelength dependence of the optical depth of the dust continuum emission. For example, assuming a typical dust composition and grain size distribution (see, e.g., [Birnstiel et al. 2018](#)), the dust opacity κ scales roughly as $\kappa \sim 10^3 (\lambda/1\mu\text{m})^{-2/3} \text{ cm}^2 \text{ g}^{-1}$. Therefore, the continuum emission at $1 \mu\text{m}$ becomes optically thick for dust column densities larger than $\sim 10^{-3} \text{ g cm}^{-2}$, while a much larger dust column density of 0.1 g cm^{-2} is required to have an optical depth of 1 at 1 mm . Assuming a standard gas-to-dust ratio of 100, the transition from optically thin to optically thick continuum emission would happen at a gas column density of 0.1 g cm^{-2} at $1 \mu\text{m}$, and 10 g cm^{-2} at 1 mm .

To understand the importance of the optical depth in detecting substructures in the dust continuum emission, it is useful to put these numbers in the context of the Minimum Mass Solar Nebula (MMSN) model ([Weidenschilling 1977b](#); [Hayashi 1981](#)). Following [Hayashi \(1981\)](#), the gas surface density of the MMSN is given by $\Sigma_g(R) = 1700 (R/1 \text{ au})^{-3/2} \text{ g cm}^{-2}$, where Σ_g is the gas surface density and R is the radial distance from the central star. At a wavelength of $1 \mu\text{m}$, the emission of the MMSN would be optically thick out to a radius of about 660 au (assuming that the MMSN extends that far), while the emission at 1 mm would be optically thick within the inner 30 au only. Due to the difference in optical depth, along with the different vertical distributions for dust particles with different sizes (see Section 3.3), observations at optical/NIR wavelengths typically constrain the scattering properties of small particles floating in the uppermost layers of protoplanetary disks, while mm and cm-wave observations typically probe the column density of larger dust grains located near the disk midplane.

Similar considerations can be done for atomic and molecular line emission. Depending on the abundance and excitation properties, the optical depth of spectral lines typically observed in protoplanetary disks may vary by multiple orders of magnitude. For example, rotational and vibrational transitions of abundant molecules like ^{12}CO are optically thick, and are used to constrain the temperature of the emitting gas, while transitions of rarer compounds are a better probe of the molecular gas density. However, the conversion between the density of a specific gas tracer and that of hydrogen is hampered by the limited knowledge of molecular abundances which are set by complex chemical networks controlled by the spectrum of the incident radiation as well as by the gas density itself (see [Miotello et al. of this book](#)). Furthermore, because wide-band continuum observations achieve a better sensitivity than narrow-band spectral line observations, most disk substructures have been observed in the mm continuum, although there have been an increasing number of substructures observed in the line observations ([Law et al. 2021, e.g.](#)). In this review, we mostly focus on disk substructures observed in scattered/thermal emission from the dust.

2.2. Substructure Occurrence

Before we dive into a discussion of disk substructures, it is important to consider any observational biases that might affect the occurrence of disk substructures. More specifically, we must keep in mind that disk substructures can be observed only if the disk emission is spatially resolved and recorded at a sufficiently high signal-to-noise ratio. To demonstrate this point, we compiled from the literature a sample of 479 young stars that have been observed at NIR and/or mm wavelengths, most of which are located in the Taurus, Ophiuchus, Upper Scorpius, Lupus, and Chameleon I star-forming regions. Figure 1 shows the disk masses and the stellar masses for this sample. The disk mass, M_d , is calculated from measured integrated 1.3 mm fluxes as $M_d = Fd^2/\kappa B(T)$, where F is the flux, d is the distance to the object, $\kappa = 0.023 \text{ cm}^2 \text{ g}^{-1}$ is the opacity, and $B(T)$ is the Planck function for which we adopt $T = 20 \text{ K}$ as in [Pascucci et al. \(2016\)](#) and [Testi et al. \(2022\)](#). When 1.3 mm fluxes are not available, as in the case of Upper Scorpius, we convert fluxes measured at other mm wavelengths, e.g., 0.87 mm, assuming a spectral index of 3.6. Finally, we convert the dust mass to the total disk mass by multiplying by a gas-to-dust mass ratio of 100. Millimeter data and stellar masses were obtained from a number of sources including [Akeson and Jensen \(2014\)](#); [Andrews et al. \(2011b, 2013\)](#); [Ansdell et al. \(2018\)](#); [Barenfeld et al. \(2017\)](#); [Cieza et al. \(2019, 2021\)](#); [Isella et al. \(2009\)](#); [Long et al. \(2018, 2019\)](#); [Pascucci et al. \(2016\)](#); [Testi et al. \(2022\)](#) (see also the references in Table 1, 2, and 3).

Out of the 479 young stars, disks have been detected around 355 objects (circles and crosses in Figure 1). For 124 non-detections (triangles in Figure 1), we put an upper limit to the disk mass. Of the 355 disks, substructures have been found in 73 disks (circles in Figure 1), either in the NIR scattered light emission, mm-wave continuum, or mm-wave molecular line emission, while substructures have not been found in the rest 282 disks (crosses in Figure 1) at the angular resolution and sensitivity of current observations. The data points use different colors to show the different ranges of the *effective* angular resolution θ_D/θ_{res} , where θ_D is the angular diameter containing 90% of the continuum emission (see, e.g., [Hendler et al. 2020](#)) and θ_{res} is the angular resolution of the observation.

In addition to the scatter plot, in Figure 1 we present histograms showing the substructure occurrence as a function of the disk and stellar masses. The histograms show that the fraction of disks with substructures increases steeply with the disk mass: the substructure occurrence rate is below 50% for disks with $M_d \lesssim 0.01M_\odot$ (corresponding to 1.3 mm flux of $\lesssim 50 \text{ mJy}$), while the substructure occurrence rate exceeds 80% for disks with $M_d \gtrsim 0.01M_\odot$. In agreement with previous analyses, the figure shows that the dust disk mass positively correlates with the stellar mass (see e.g., [Andrews et al. 2013](#); [Pascucci et al. 2016](#) and [Manara et al. of this book](#)). As a result, the larger substructure occurrence rate for high-mass disks translates to large sub-

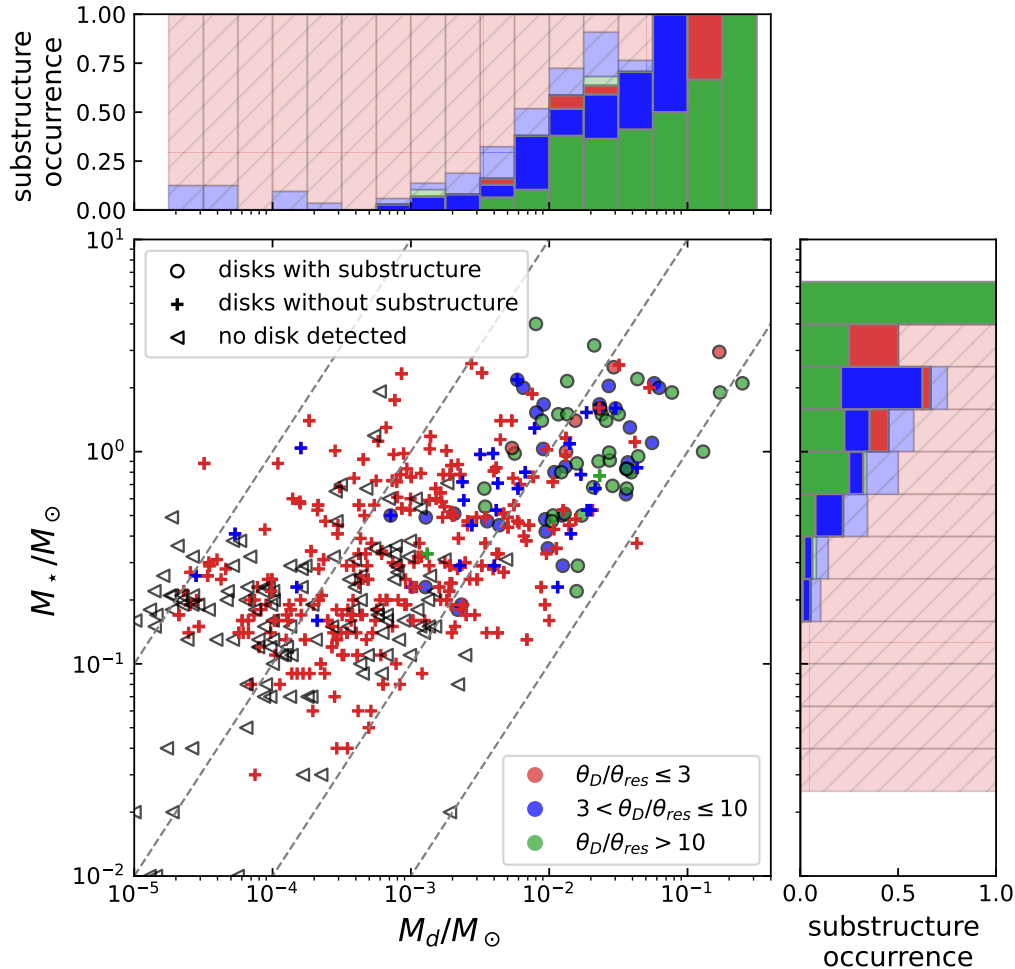


Fig. 1.— Mass of the disk inferred from mm continuum flux vs. mass of the host star for a sample of 479 young stars (see Section 2.2). Solid circles indicate disks with substructures, crosses indicate disks where no substructures were observed, and triangles indicate disks with an upper limit for the continuum flux (i.e., non-detection). Data points are color-coded by the ratio between the angular diameter containing 90% of the continuum emission (θ_D) and the angular resolution of the observations (θ_{res}). See the legend in the lower-right corner. The four diagonal dashed lines show constant disk-to-star mass ratios of $M_d/M_* = 0.0001, 0.001, 0.01,$ and 0.1 (from left to right). The histograms presented in the upper and right panels show the fraction of disks with (solid) and without (hatched) substructures in each (upper panel) disk mass and (right panel) stellar mass bin. The histograms are color-coded by θ_D/θ_{res} in the same way to the scatter plot. The histograms suggest that the fraction of disks with substructures may increase with M_* and M_d ; however, note that the histograms clearly depict that the majority of disks without substructures have been observed at low effective angular resolution of $\theta_D/\theta_{res} \leq 3$ (red hatched regions of the histograms). Future high angular resolution observations are crucial to properly assess whether or not substructure occurrence depends on M_* and/or M_d .

structure occurrence rate for high-mass stars. Taken at face value, the correlation between substructure occurrence and the disk mass (or stellar mass) might offer valuable information for understanding the origin of the substructures. However, caution must be taken because this correlation might instead result from observational biases. In fact, for the 256 disks observed with a low effective angular resolution of $\theta_D/\theta_{res} \leq 3$, substructures have been detected in only 2% of the sample (5 disks). When disks are observed with an intermediate effective angular resolution of $3 < \theta_D/\theta_{res} \leq 10$, substructures are found in about half

of the sample (32 disks with substructures out of total 62 disks). Finally, when disks are observed with a high effective angular resolution of $\theta_D/\theta_{res} > 10$, substructures are found in 95% of the sample (35 disks with substructures out of total 37 disks). As we mentioned at the beginning of this subsection, sufficiently high angular resolution (and sensitivity) is required to detect disk substructures, and it is not surprising that most of the disks with substructures have been observed with high effective angular resolution. The apparent lack of substructures in less massive disks could perhaps be explained with the fact that current observations

have not yet achieved the angular resolution necessary to discover their substructures.

As we will discuss in the subsequent Sections, certain substructure-forming scenarios, such as gravitational instability and companions, favor a large disk mass (or large M_d/M_*). On the other hand, other scenarios favor a small disk mass (e.g., vertical shear instability since it requires rapid cooling) or are expected to be relatively insensitive to the disk mass (e.g., icelines). Future high resolution observations across a range of disk mass bins are highly desirable to obtain more complete statistics on disk substructures, but also to start to answer whether the increasing substructure occurrence rate with disk mass is simply due to the fact that low-mass disks have not been observed at sufficiently high angular resolution or the trend reflects the underlying substructure-forming processes.

2.3. Substructure Morphology

Figure 2 presents some examples of observed disk substructures. It has been customary to group disk substructures into three main classes: rings and gaps, spirals, and crescents. However, it is worth noting that a large variety of properties have been observed and thus any rigid classification is challenging. Also, it turned out that a single disk can have multiple types of substructures, and it is possible that a disk shows different classes of substructures when observed at different wavelengths. For examples, rings, gaps, spirals, and crescents are observed in the mm continuum image of the MWC 758 disk, while only spirals are observed in the IR observations (Figure 2; *Dong et al. 2018b*; *Benisty et al. 2015*).

Keeping in mind these nuances, in Table 1, 2, and 3² we group the 73 disks with substructures introduced above based on the presence of rings, spirals, and crescents. For each object, we list the distance from Earth (d), the stellar mass (M_*), the stellar luminosity (L_*), the infrared SED classification, the disk mass (M_d), the number of substructures, the radial location or extent of the substructures, the main properties of the substructures, and the wavelength (mm or IR) at which the substructures were observed. For binary systems, we also provide the angular separation between the stars. References from which the information is adopted are listed in the captions of the Tables.

Substructures were observed at both infrared and mm wavelengths in 21 disks, while substructures were observed at only mm or infrared wavelengths in the other 49 and 3 objects, respectively. Rings and gaps are observed in 62 disks and are the most common type of substructure, while spirals and crescents are observed in 22 and 13 disks, respectively. Finally, 19 disks have more than one type of substructure. In the following subsections, we discuss the occurrence and properties of each type of substructure. Note that in this section, we mostly focus on reporting the findings from the observational data and defer the discussion as to what those

findings may indicate in terms of their origin to Section 9, after we introduce substructure-forming processes in Sections 4 – 8.

2.3.1. Rings and gaps

Occurrence: Rings are generally defined as being intrinsically circular and azimuthally symmetric. They are the most common type of substructure observed in protoplanetary disks thus far. A total of 120 unique rings (113 at mm and 7 at NIR) have been detected in 62 disks (Table 1) among the 73 disks with substructures compiled in this review. Rings and gaps are far more common in mm observations (61 disks) compared to NIR observations (6 disks, see also *Benisty et al.* in this book). One possible explanation to the apparent discrepancy between mm and NIR observations is that the observed rings coincide with pressure maxima, efficiently trapping large particles and facilitating the detection in mm observations (see Section 3). Disks with large (> 20 au) inner cavities are a noteworthy subset of disks with rings and gaps. At least 15 objects could be included in this class. About half of these objects show an imaged inner disk and/or infrared excess in the SED indicating the presence of a small ($< 3 - 5$ au) dusty disk. An example is MWC 758, where the inner disk is detected but not spatially resolved by existing ALMA observations with angular resolution down to $0''.04$ (corresponding to 6 au linear resolution; *Dong et al. 2018b*). The other half show no or little infrared excess in the SED implying that dust is depleted in the innermost disk regions. These disks are classified as transitional disks (TD; Table 1). We find that the fraction of disks with rings increases with M_d/M_* (Figure 3 (a) and (b)) although we caution that this correlation may be due to the observational bias we discussed in Section 2.2.

Multiplicity: About half of systems with rings show a single ring, but multi-ring systems have been commonly observed (see Figure 3 (c)) particularly at the highest spatial resolution provided by ALMA. Outstanding examples of multi-ring systems include HL Tau and AS 209 with 7 rings each (*ALMA Partnership et al. 2015*; *Andrews et al. 2018a*; *Huang et al. 2018b*), TW Hya with 5 rings (*Andrews et al. 2016*; *Huang et al. 2018a*), and HD 163296, CI Tau, and RU Lup with 4 rings each (*Clarke et al. 2018*; *Isella et al. 2018*; *Huang et al. 2020b*). Some of the single-ring systems have been observed at a relatively coarse resolution, and it is possible that future high-resolution observations may detect additional rings and gaps. As an example, this has been the case for LkCa 15 for which observations at $0''.15 - 0''.25$ angular resolution (corresponding to $\simeq 24 - 40$ au linear resolution) initially revealed a single ring (*Andrews et al. 2011a*; *Isella et al. 2014*; *Jin et al. 2019*), but later ALMA observations at $0''.05$ angular resolution (corresponding to $\simeq 8$ au linear resolution) resolved the previously observed single ring to have at least two, and perhaps three, components (*Facchini et al. 2020*).

Radial location: Rings can be described using a 1-D

²The data presented in the tables are available online at <http://ppvii.org/chapter/12/>.

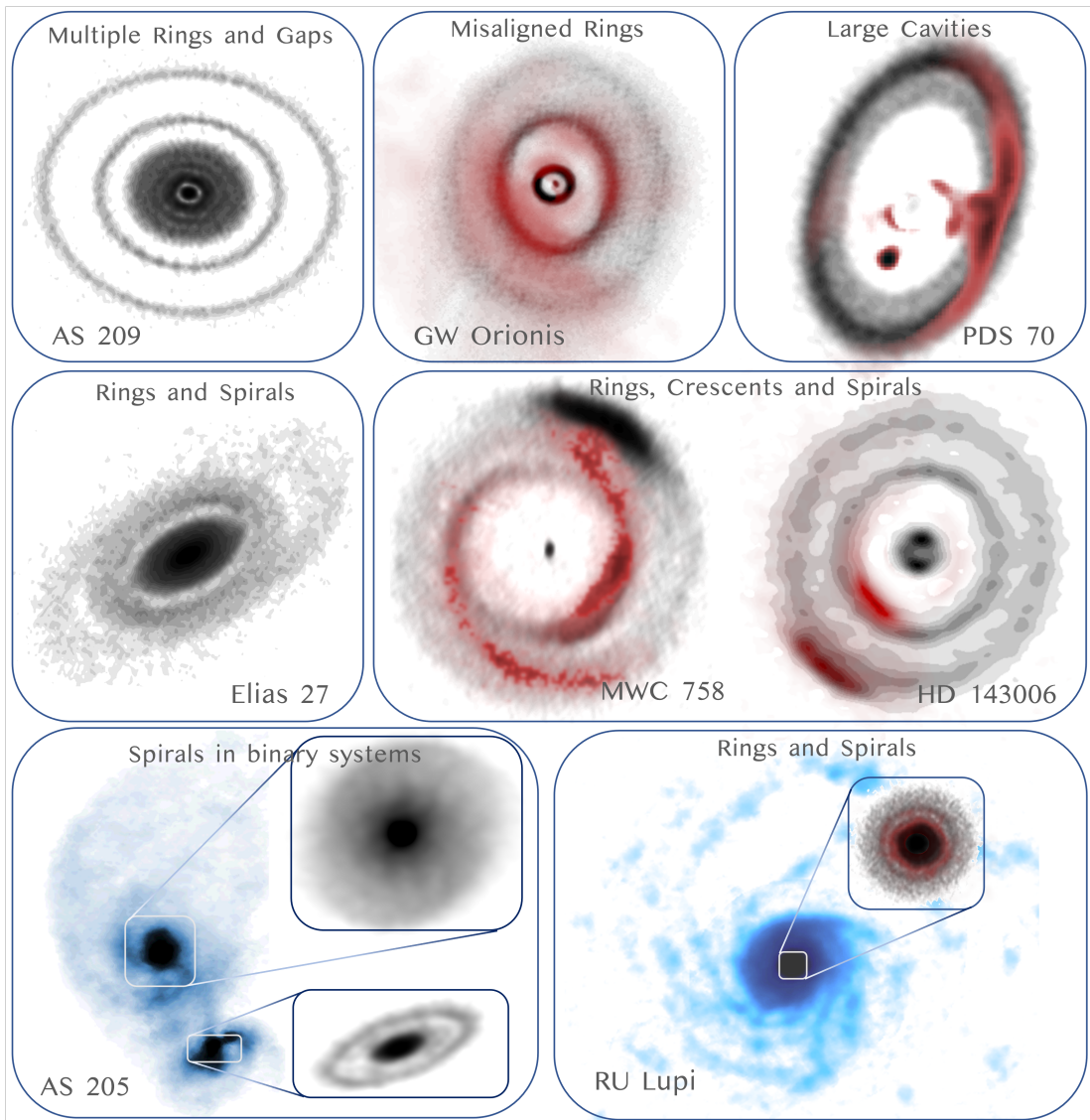


Fig. 2.— Some of the morphological features observed in protoplanetary disks, including concentric rings and gaps, misaligned rings, large cavities, spirals, and crescents. Note that there are some disks which have more than one substructure: Elias 2-27, MWC 758, HD 143006, AS 205, RU Lup. Black and white contours show mm continuum observations, blue contours show mm line observations, and red contours show NIR observations, respectively. The data presented in this figure are originally from: AS 209 – [Andrews et al. \(2018b\)](#), GW Ori – [Bi et al. \(2020\)](#); [Kraus et al. \(2020\)](#), PDS 70 – [Keppler et al. \(2018\)](#); [Benisty et al. \(2021\)](#), Elias 2-27 – [Andrews et al. \(2018b\)](#), MWC 758 – [Benisty et al. \(2015\)](#); [Dong et al. \(2018b\)](#), HD 143006 – [Andrews et al. \(2018b\)](#); [Benisty et al. \(2018\)](#), AS 205 – [Andrews et al. \(2018b\)](#); [Kurtovic et al. \(2018\)](#), RU Lup – [Andrews et al. \(2018b\)](#); [Huang et al. \(2018b\)](#).

Gaussian function $I(R) \propto I_0 e^{-(R-R_0)^2/2\sigma_R^2}$, where R_0 is the radius of the ring and σ_R is its radial width. For mm observations, R_0 and σ_R are often measured by fitting the Gaussian model to visibilities. Rings are observed at essentially all radii from as close as 3 au to the host star (TW Hya) to as far as 205 au (HD 142527) from the host star, with a maximum frequency occurring at 20 – 50 au (Figure 3(d)). The steep drop in frequency at small radii (< 20 au) is due to the limited angular resolution of the observations, while the gradual drop at large radii beyond 50 au likely represents the radial extent of the continuum disks. Besides that,

we do not find any correlation between the radial location of the rings and stellar/disk properties (e.g., Figure 3(e)).

Radial width: Measurements of the radial width of the continuum rings have been obtained for 88 rings out of a total of 113. Ring widths range from a few au, set by the best resolution achieved with ALMA, to about 80 au (Figure 3 (f)). However, some of the widest rings have only been marginally resolved, and it is therefore possible that they might be composed of multiple narrow rings, as in the case of LkCa 15 mentioned above. Similar to the radial location of rings, we do not find any correlation between the

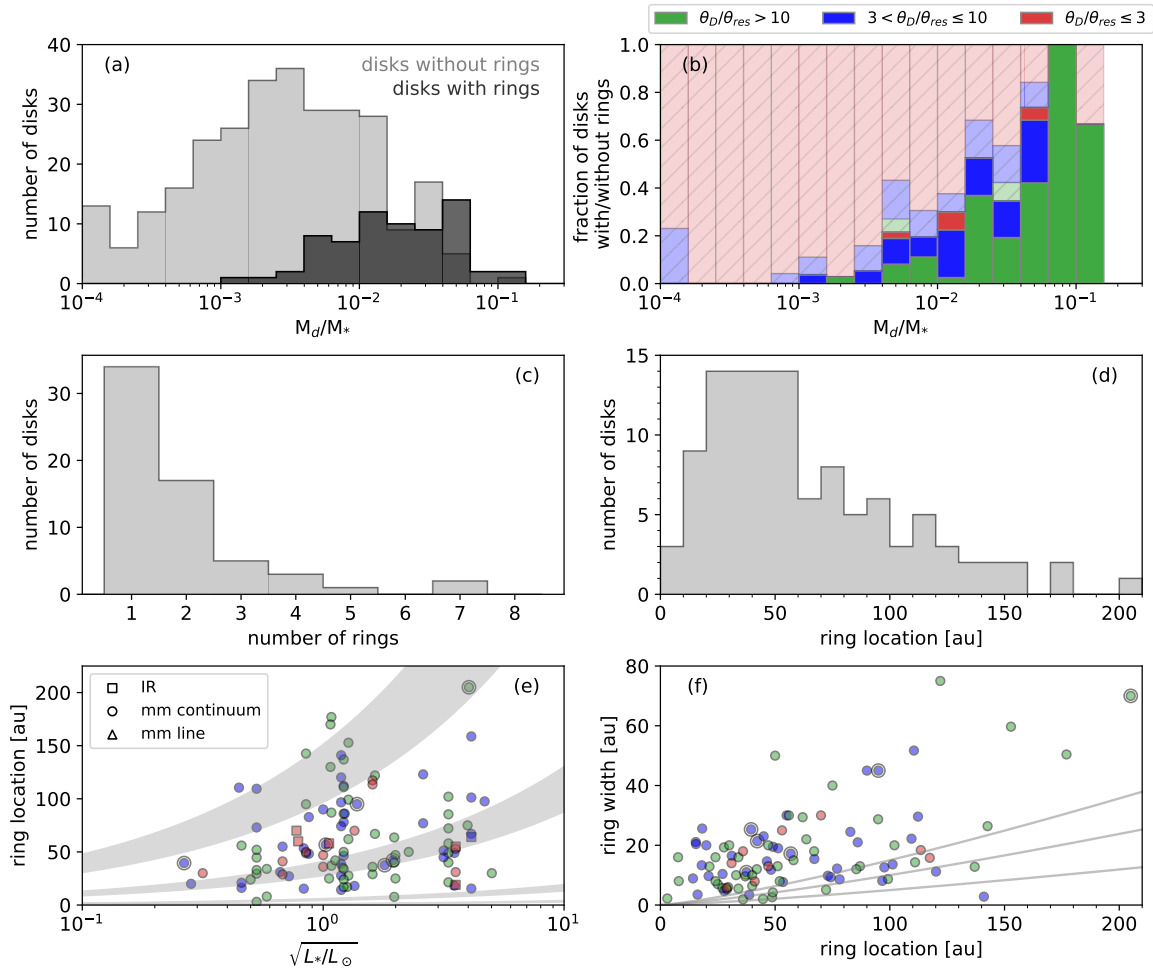


Fig. 3.— (a) Histograms showing the number of disks (gray) without rings and (black) with rings, as a function of M_d/M_* . The bin size is 0.2 dex in the logarithmic scale. (b) A histogram showing the fraction of disks with and without rings in each M_d/M_* bin. The same colors as in Figure 1 are used to present the effective angular resolution used for observations. (c) A histogram showing the number of rings in each disk that is known to have rings. (d) A histogram showing the radial location of individual rings. (e) A scatter plot presenting the radial location of rings vs. $\sqrt{L_*/L_\odot}$. Squares show the rings detected in IR observations, circles show the rings detected in mm continuum observations, and triangles show the rings detected in mm line observations, respectively. Double symbols (e.g., two concentric circles) indicate binary systems. The shaded gray regions represent the parameter space where N_2 , CO, CO_2 , and H_2O icelines (from top to bottom) would be located. (f) A scatter plot showing the radial width of the rings vs. the radial location of the rings. The three gray curves show the gas scale height $H = (H/R)_{100 \text{ au}}(R/100 \text{ au})^{1/4}$ adopting $(H/R)_{100 \text{ au}} = 0.15, 0.1,$ and 0.05 (from top to bottom).

radial width of the rings and the stellar or disk properties.

Misalignment: If mm-wave dust rings are optically thin and trace the disk midplane, their aspect ratio provides a direct measurement of the disk inclination relative to the line-of-sight. Although most of the multi-ring systems appear to be co-planar, there are systems where the disk inclination varies with the distance from the central star, implying a misalignment or warp in the disk. Such examples include HD 143006, DoAr44, AA Tau, HD 142527, HD 100453, HD 100546, J1604-2130, HD 139614, and GW Ori (Benisty et al. 2018; Pérez et al. 2018; Casassus et al. 2018; Loomis et al. 2017; Marino et al. 2015; Benisty et al. 2017; Walsh

et al. 2017; Mayama et al. 2018; Bi et al. 2020; Kraus et al. 2020). For these disks, the degree of misalignment appears to range from 30° (HD 143006, DoAr 44) to 80° (HD 100546). In NIR observations, misalignments can manifest themselves as a shadow cast on the misaligned outer disk (e.g., Min et al. 2017; Bohn et al. 2021). For a more complete review of misalignments and shadows, we refer readers to Benisty et al. in this book.

2.3.2. Spirals

Occurrence: Spirals are less common than rings and have been observed in only 22 disks so far (Table 2).

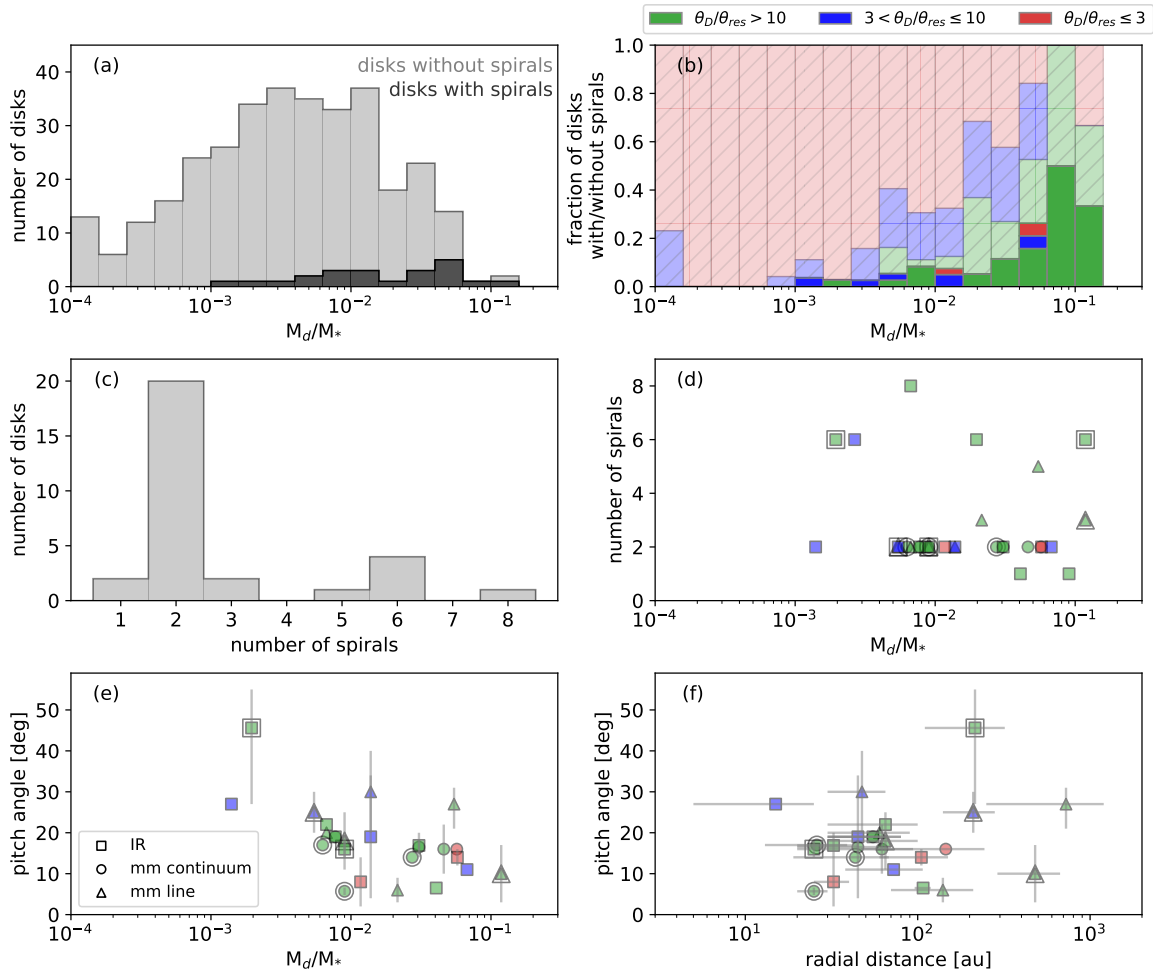


Fig. 4.— (a) Histograms showing the number of disks (gray) without spirals and (black) with spirals, as a function of M_d/M_* . The bin size is 0.2 dex in the logarithmic scale. (b) A histogram showing the fraction of disks with and without spirals in each M_d/M_* bin. The same colors as in Figure 1 are used to present the effective angular resolution used for observations. (c) A histogram showing the number of disks as a function of the number of spirals. (d) A scatter plot presenting the number of spirals vs. M_d/M_* . Squares show the spirals detected in IR observations, circles show the spirals detected in mm continuum observations, and triangles show the spirals detected in mm line observations, respectively. Double symbols (e.g., two concentric circles) indicate binary systems. (e) A scatter plot showing the pitch angle vs. M_d/M_* . The vertical bars show the range of pitch angle of spirals in multi-spiral systems. (f) A scatter plot showing the pitch angle vs. radial extent of the spirals (shown with horizontal bars).

Among the 22 disks, 17 disks show spirals in NIR observations and 12 disks show spirals in the mm continuum or line emission. In 7 disks, spirals are detected at both NIR and mm wavelengths although the properties of the spirals inferred at different wavelengths do not necessarily match (see Table 2). So far, spirals have been observed in 6 multiple stellar systems, either in the disk around the primary star as in AS 205N (Figure 2, *Kurtovic et al. 2018*), or in the circumbinary disk as in HD 142527 (*Fukagawa et al. 2006*). Similar to rings and gaps, the fraction of disks with spirals appears to increase with the M_d/M_* ratio (Figure 4 (a) and (b)), although we caution again that this may be a result of observational biases (see Section 2.2).

Multiplicity: The number of spirals in the 22 disks

ranges from 1 to 8, but there is a significant peak at 2 (Figure 4 (c)). We find no obvious correlation between the number of spirals and the stellar or disk properties including M_d/M_* (Figure 4 (d)). However, we find one noticeable difference when spirals in mm and NIR observations are compared. Spirals in NIR observations tend to reveal a larger number of spirals: all five systems with 6 or more spirals are observed in NIR, whereas mm observations have so far revealed only two- or three-armed spirals.

Pitch angle: Pitch angle defines how tightly a spiral is wound. Mathematically, the pitch angle ψ is given by $\tan \psi = -dR/(Rd\phi)$. Pitch angles are generally smaller than 30° , with the exception of HD34700A and CQ Tau which have pitch angles as large as $40 - 55^\circ$ (*Uyama et al.*

2020b; Wölfer et al. 2021). We find a weak trend that the pitch angle decreases as a function of M_d/M_* (Figure 4 (e)). At face value, this appears to be consistent with the finding by Yu et al. (2019). However, we note that this trend may be exclusive to the spirals detected in IR and is weak or missing for the spirals detected in mm continuum observations or mm line observations. The pitch angle does not appear to be correlated with the radial location of the spirals (Figure 4 (f)). There are seven disks where spirals are probed at more than one wavelength. For MWC 758, WaOph6, and HD 100453, spirals are detected in NIR and mm continuum observations which must probe significantly different heights in the disks (see Section 2.1). Among the three disks, in HD 100453 the pitch angle of the spirals measured in NIR and mm molecular line observations (14–18° and 11–25°, respectively) are larger than the pitch angle measured in mm continuum (5–7°; Rosotti et al. 2020a). For the other two disks, the pitch angles measured in NIR and mm continuum observations are comparable.

Radial extent: Spirals are observed across a wide range of radii from 5 to > 1000 au (Figure 4 (f)). The innermost radius at which spirals are observed depends either on the angular resolution of the observations, or, as in the case of NIR observations, on the size of the coronagraph used to occult the central star.

Pattern speed and time variation: Pattern speed and time variation of spirals are not shown in Table 2 or Figure 4 because such studies require long-term monitoring observations which are still scarce. However, they can potentially be used to determine the origin of the spirals. One example is presented in Ren et al. (2020), where the pattern speed of the spirals in the MWC 758 disk was inferred to be $0^\circ.22 \pm 0^\circ.03 \text{ yr}^{-1}$ over a 5 year time baseline. The pattern speed of the spirals is comparable to the orbital frequency at 172_{-14}^{+18} au assuming a $1.9 M_\odot$ central stellar mass. Because the spirals extend from about 40 to 80 au and the local Keplerian frequency over that radial extent ($0.7 - 2^\circ.0 \text{ yr}^{-1}$) is significantly larger than the observed spiral pattern speed, Ren et al. (2020) concluded that the spirals are not locally excited, but launched at larger orbital radii and propagated inward. Another example for which the motion of spirals is monitored is SAO 206462. Xie et al. (2021) explains the spiral motion with a single planet in a circular orbit at 86 au, although there is tentative evidence that the two spirals have different pattern speed, which may require the presence of two planets or one planet in an eccentric orbit (Zhu and Zhang 2022a).

2.3.3. Crescents

Crescents can be described as rings that have an azimuthal variation in intensity. Their identification is straightforward when the azimuthal intensity variation is apparent, as in the case of IRS 48 (van der Marel et al. 2013), HD 142527 (Boehler et al. 2018), and HD 143006 (Andrews et al. 2018b; Pérez et al. 2018, see also Figure 2). However, the distinction between rings and crescents

is not straightforward when the azimuthal intensity contrast is close to unity. In addition, the apparent asymmetry can be due to dust’s scattering phase function and/or the disk’s geometry, instead of the intrinsic dust distribution in the disk. Disentangling all these factors is fruitful, but challenging. As such, in this review we will mainly focus on the crescents in the (sub-)millimeter continuum observations, because they are believed to largely trace the dust distribution at the midplane and less sensitive to scattering phase function or disk geometry. Also, we will narrow our discussion on highly asymmetric disks with a large brightness contrast, which is a clear indication that dust has been azimuthally trapped in some disk features. With this in mind, in Table 3, we compile a list of disks with crescents with the ratio between the maximum and minimum intensities along the azimuth equal to or greater than 1.5.

Occurrence: Crescents are rarer than rings and spirals, and only a total of 19 crescents have been observed so far in 13 different disks. Due to the small number, it is not possible to draw a conclusion as to if the occurrence of crescents depends on the disk mass. However, it is worth noting that the occurrence rate of crescents is about 30% for the disks with $M_d/M_* > 0.05$, while the rate drops significantly to < 5% for the disks with $M_d/M_* < 0.05$.

Multiplicity: Millimeter observations show one crescent per disk, except in MWC 758 for which two crescents are observed at different radial locations, 48 and 83 au. There are two disks for which crescents are observed in IR observations: HD 143006 has 2 crescents (Benisty et al. 2018) and HD 139614 has 4 crescents (Muro-Arena et al. 2020). We note that the crescent at 74 au in the HD 143006 disk is the only crescent observed at both IR and mm wavelengths thus far (Benisty et al. 2018; Andrews et al. 2018b; Pérez et al. 2018). For HD 139614, Muro-Arena et al. (2020) suggested that the observed azimuthally asymmetry in the brightness can be explained with multiple misaligned/warped inner disks. In general, NIR scattered light observations are sensitive to shadows (see Benisty et al. in this book), so caution is needed when interpreting azimuthal intensity variations especially when a co-locating mm counterpart is not observed. Among all 13 disks that we compiled, there is no case where multiple crescents are observed at the same radial location within a single annular structure.

Radial location: Crescents are discovered at various distances from 22 au to 185 au from the star, and they do not appear to be clustered at any particular radial locations (Figure 5 (a)). A potential pattern we see is that crescents are located at large distance in circumbinary disks (HD 34700A, HD142527). This may suggest that the presence of the companion star can have an influence on the location of crescents, although small number of the sample limits us to make any firm conclusions.

Width and aspect ratio: Radial and azimuthal widths of a crescent are usually calculated by fitting 2D-Gaussian functions to the intensity. The ratio between the azimuthal and radial width defines the aspect ratio, which, as we will dis-

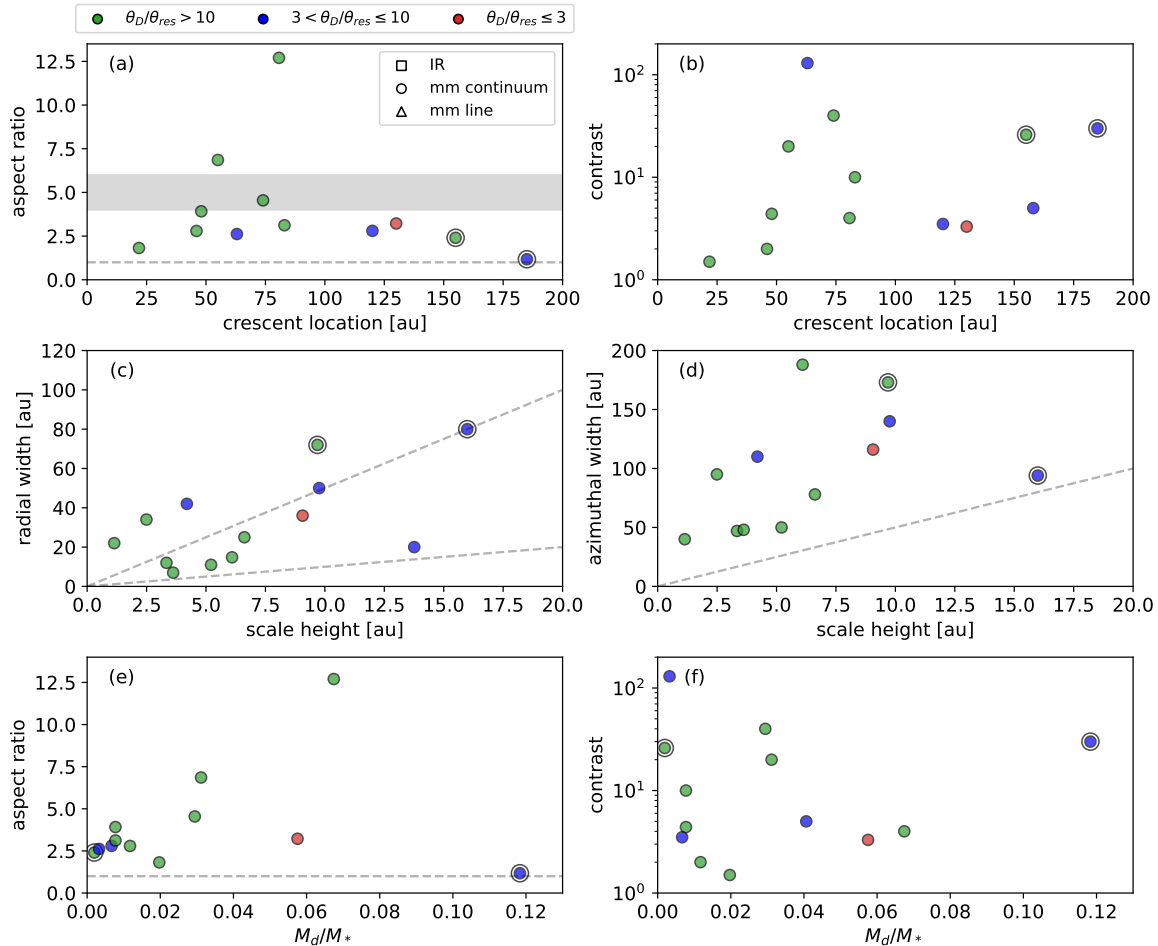


Fig. 5.— (a) Aspect ratio of crescents, defined as the ratio between the azimuthal FWHM and the radial FWHM, as a function of the radial location of the crescents. Squares show the crescents detected in IR observations, circles show the crescents detected in mm continuum observations, and triangles show the crescents detected in mm line observations, respectively. Double symbols (e.g., two concentric circles) indicate binary systems. The same colors as in Figure 1 are used to present the effective angular resolution used for observations. The gray shaded region shows aspect ratio between 4 and 6, a range with which a vortex can survive from elliptical instability (see Section 9.3). (b) Contrast of crescents, defined as the ratio between the peak brightness and minimum brightness at the radius of the crescent, as a function of the radial location of the crescents. (c) The radial width of crescent w_R as a function of the disk scale height H . The gas scale height $H = c_s/\Omega_K$, where $c_s = \sqrt{\mathcal{R}T_{\text{irr}}/\mu}$, is computed using the stellar irradiation-dominated temperature $T_{\text{irr}} = [\phi L_*/(4\pi r^2\sigma)]^{1/4}$ (e.g., *Chiang and Goldreich 1997*; *D’Alessio et al. 1998*; *Dullemond et al. 2001*). Here, ϕ accounts for the non-normal flaring angle. We adopt $\phi = 0.02$, the value adopted in DSHARP papers (*Huang et al. 2018b*; *Dullemond et al. 2018*) for $H/R \approx 0.07$ at 100 au for a star of solar mass and luminosity; however, we find that adopting a different value does not change the trend that $w_R > H$. The two dotted lines show (top) $w_R = 5H$ and (bottom) $w_R = H$. (d) The azimuthal width of crescent w_ϕ as a function of the disk scale height H . The dotted line shows $w_\phi = 5H$. (e) The aspect ratio as a function of M_d/M_* . The dotted lines shows aspect ratio of 1. (f) The contrast as a function of M_d/M_* .

cuss in Section 9.3, is important to constrain the formation process. Radial widths are measured for 13 out of a total of 19 crescents and vary between about 7 and 80 au (Figure 5 (c)). Azimuthal widths are measured for 12 crescents and vary between about 40 and 190 au (Figure 5 (d)). Combined together, the resulting aspect ratio ranges from ~ 1 (i.e., a nearly circular crescent) to ~ 13 (i.e., a crescent very elongated in azimuthal direction). However, most of the aspect ratios lie between 2 and 5 (Figure 5 (a) and (e)). The as-

pect ratio of crescents does not appear to be related to their radial locations (Figure 5 (a)) but there seems to be a tentative trend that crescents with larger aspect ratios are found in more massive disks (Figure 5 (e)).

Contrast: The contrast of the observed crescents varies from a minimum of 1.5, the threshold used to distinguish between rings and crescents, to a maximum of > 130 in the case of IRS 48. In IRS 48 and few other disks, the observations only provide a lower limit for the contrast because

no continuum emission is measured on the opposite side of the crescent. There is a very tentative trend that the contrast of crescents decreases with M_d/M_* (Figure 5 (f)). Beside that, we find no correlation between the contrast of the crescents and the disk or stellar properties.

2.3.4. Other (sub)structures

Although we focus on rings/gaps, spirals, and crescents in this review, we note that there are an increasing number of other types of (sub)structures. These include, but not limited to, kinematic substructure (Pinte *et al.* 2018, 2019, see also Pinte *et al.* in this book), and tails or streamers (e.g., Akiyama *et al.* 2019; Pineda *et al.* 2020; Ginski *et al.* 2021, see also Pineda *et al.* and Pinte *et al.* in this book).

3. Coupling Between Gas and Dust

When interpreting substructures probed by emission from the dust, it is important to keep in mind that the spatial distribution of the dust may be different to that of the gas. This is because the gas is supported against the central star's gravity by pressure gradients (both radially and vertically), whereas the dust is not. The resulting relative velocity between the gas and the dust causes aerodynamic drag. In general, the mobility of dust particles relative to the gas can lead to concentrations of dust particles in narrow regions, amplifying the contrast of their emission and facilitating the detection of disk substructures in the dust emission.

3.1. Aerodynamic drag

For a particle with radius, a , that is smaller than the mean free path of the ambient gas molecules, λ_{mfp} (more precisely $a < 9\lambda_{\text{mfp}}/4$), the drag occurs as the particle collides with individual gas molecules. This is called Epstein drag (Epstein 1924). λ_{mfp} is of order of ~ 1 cm in the mid-plane at 1 au in the MMSN, and increases with the inverse of the gas density $1/\rho_g$. For the disk regions ($\gtrsim 10$ au) and particle sizes ($\lesssim 1$ cm) that this Chapter focuses on, it is safe to assume that particles experience Epstein drag. In the Epstein regime, the drag force F_D is given by

$$F_D = -\frac{4}{3}\pi a^2 \rho_g \Delta v v_{\text{th}}, \quad (1)$$

where ρ_g is the gas density, Δv is the relative velocity between the particle and the gas, $v_{\text{th}} \equiv \sqrt{8/\pi} c_s$ is the thermal speed of the gas molecules and c_s is the sound speed.

The drag force acts in the opposite direction to Δv such that the solid particle loses (angular) momentum. The timescale over which this happens is called stopping time $t_{\text{stop}} \equiv m\Delta v/|F_D|$, where m is the mass of the solid particle of interest. The stopping time is the key parameter describing the coupling between the gas and the dust. Using Equation (1), the stopping time is given by

$$t_{\text{stop}} = \frac{\rho_s a}{\rho_g v_{\text{th}}}, \quad (2)$$

where ρ_s is the mean internal density of the particle. In the limit of short stopping time $t_{\text{stop}} \ll t_{\text{dyn}}$, where t_{dyn} is the dynamical timescale, Δv vanishes (because otherwise the drag force would diverge) and the particle follows the gas motion. In the opposite limit of long stopping time $t_{\text{stop}} \gg t_{\text{dyn}}$, the aerodynamic drag is negligible and the particle decouples from the gas. In the intermediate regime where the stopping time is comparable to the dynamical timescale $t_{\text{stop}} \simeq t_{\text{dyn}}$, the particle can move relative to the gas but its motion is still largely affected by aerodynamic drag. This partial coupling drives secular drift motion and plays a crucial role in shaping substructures.

It is often useful to define a dimensionless stopping time, which is also called Stokes number,

$$\text{St} = \Omega_K t_{\text{stop}}, \quad (3)$$

where Ω_K is the local Keplerian frequency. In a vertically isothermal disk where the gas density ρ_g relates to the vertically integrated surface density Σ_g as $\rho_g = \Sigma_g/(\sqrt{2\pi}H) \exp[-Z^2/(2H^2)]$, where Z denotes the height in the disk and H denotes the scale height of the gas, the Stokes number is given by

$$\begin{aligned} \text{St} &= \frac{\pi \rho_s a}{2\Sigma_g} \exp\left(\frac{Z^2}{2H^2}\right) \\ &= 0.16 \exp\left(\frac{Z^2}{2H^2}\right) \left(\frac{\rho_s}{1 \text{ g cm}^{-3}}\right) \left(\frac{a}{1 \text{ mm}}\right) \\ &\quad \times \left(\frac{\Sigma_g}{1 \text{ g cm}^{-2}}\right)^{-1}. \end{aligned} \quad (4)$$

For the outer disk regions where $\Sigma_g \simeq 1 \text{ g cm}^{-2}$, we thus expect (sub)mm-sized particles to have a Stokes number close to unity (i.e., $t_{\text{stop}} \simeq t_{\text{dyn}}$) and to experience strong aerodynamic drag, whereas μm -sized particles have a Stokes number orders of magnitude smaller than unity (i.e., $t_{\text{stop}} \ll t_{\text{dyn}}$) and couple well to the gas.

3.2. Horizontal Drift

The most important consequence of aerodynamic drag in protoplanetary disks is the radial drift of solid particles. The orbital velocity of the gas $v_{g,\phi}$ is determined by the balance between the centrifugal force, stellar gravity, and the radial gas pressure gradient, dP/dR , with

$$\frac{v_{g,\phi}^2}{R} = \frac{GM_* R}{(R^2 + Z^2)^{3/2}} + \frac{1}{\rho_g} \frac{dP}{dR}. \quad (5)$$

On global scales, the density and temperature of the gas decrease as a function of radius, so the pressure gradient dP/dR is negative. This means that the gas orbits at a sub-Keplerian speed. For solid particles, on the other hand, the pressure gradient is negligible and so particles orbit at the Keplerian velocity in the absence of aerodynamic drag. As a result, the sub-Keplerian gas motion acts on solid particles as a headwind, removing angular momentum from solid particles and causing particles to drift inward.

The radial drift velocity of solid particles arising from the aerodynamic drag can be written as

$$v_{d,R} = \frac{St^{-1}v_{g,R} - \eta v_K}{St + St^{-1}}, \quad (6)$$

where

$$\eta \equiv -(\rho_g R \Omega_K^2)^{-1} \frac{dP}{dR} = -(c_s/v_K)^2 \frac{d \ln P}{d \ln R} \quad (7)$$

(Whipple 1972; Adachi et al. 1976; Weidenschilling 1977a; Nakagawa et al. 1986; Takeuchi and Lin 2002). For small particles with $St \lesssim \alpha \ll 1$, Equation (6) reduces to $v_{d,R} \simeq v_{g,R} - St\eta v_K \simeq v_{g,R}$ ³, so particles follow the gas motion. For larger particles with $St \gtrsim \alpha$, where α is the dimensionless parameter describing the viscous stress (Shakura and Sunyaev 1973), the radial drift velocity approximates to $v_{d,R} \simeq -\eta v_K / (St + St^{-1})$ so they decouple from the gas. Note that in the large particle regime, the radial drift velocity maximizes when $St = 1$. The timescale for the radial drift is given by $t_{\text{drift}} = R/|v_{d,R}|$. For particles with $St = 1$, $t_{\text{drift}} \simeq 2/(\eta\Omega_K)$. Since $\eta \simeq 10^{-3} - 10^{-1}$ under typical protoplanetary disk conditions, particles with appropriate sizes can drift (and be lost from the disk) within about 10^3 orbital periods, corresponding to 1,000 years at 1 au and 1 million years at 100 au around a solar-mass star. Such a short drift timescale can prevent particles from growing in size. As such, this is often called a “radial-drift barrier” or a “meter-size barrier” in planet/planetesimal formation, where the latter is named after the fact that $St = 1$ particles at 1 au in the MMSN have a size of about one meter (Weidenschilling 1977a).

So far, we have assumed that the pressure gradient dP/dR is negative. However, when there is an inversion in the pressure gradient ($dP/dR > 0$), the gas orbits at a super-Keplerian speed. In this case, particles experience a tailwind and thus drift outward. Although a global inversion of dP/dR is unlikely, protoplanetary disks can have a local pressure gradient inversion around pressure bumps formed, for example, at the outer edge of a gap carved by a planet. At the peak of a pressure bump, the pressure gradient is zero and the aerodynamic drag vanishes. Thus, pressure bumps offer prime sites to trap particles (Whipple 1972; Pinilla et al. 2012). Using ALMA molecular line observations, Teague et al. (2018a) measured the rotational velocity of the gas in the disk around HD 163296 and showed that the pressure peaks co-locate with the continuum rings in the disk (see also Teague et al. 2018b; Rosotti et al. 2020b). This provides direct evidence that particles experience radial drift and are trapped in gas pressure bumps.

In addition to the radial drift, one can consider azimuthal drift. Although azimuthal drift is negligible in axisymmet-

ric disks ($dP/d\phi = 0$), azimuthal drift can become important when a disk has asymmetric structures, such as crescents and spirals. When there exists a high-pressure anticyclonic vortex in the disk, particles drift toward the pressure peak in both the radial and azimuthal directions and can be trapped therein (Barge and Sommeria 1995; Adams and Watkins 1995; Tanga et al. 1996). Spirals offer another implication, although the situation can be different from vortices. While vortices orbit at the local Keplerian speed, spirals can orbit at a speed that is significantly different from the local Keplerian speed. For example, at a finite distance from a planet, a spiral launched by the planet orbits at the orbital frequency of the planet Ω_p , not at the local Keplerian speed Ω_K . As such, particles with a stopping time shorter than the spiral crossing time, $t_{\text{stop}} \lesssim \Delta\phi_s/|\Omega_p - \Omega_K|$ where $\Delta\phi_s$ is the azimuthal width of the spiral, can be trapped by the spiral, while particles with a longer stopping time than the spiral crossing time do not have sufficient time to respond to the perturbation and thus would be poorly coupled to the spiral (see e.g., Isella and Turner 2018; Sturm et al. 2020).

3.3. Vertical Settling

Aerodynamic drag also changes the vertical distribution of particles relative to the gas. A particle located at height Z ($\ll R$) above the midplane feels the vertical component of stellar gravity, $F_{\text{grav}} = -m\Omega_K^2 Z$. Equating the gravitational force and the drag force in Equation (1), the vertical settling velocity is given by $v_{d,Z} = St\Omega_K Z$. The vertical settling timescale can be then written as $t_{\text{sett}} = |Z/v_{d,Z}| = 1/(St\Omega_K)$. At one scale height above the midplane in the MMSN, the settling timescale for a μm -sized particle is about one million years, independent of R ⁴. For a mm-sized particle, the settling timescale is only about 1,000 years since the settling timescale is inversely proportional to the particle size. This suggests that in the absence of turbulent stirring, particles should settle on timescales shorter than the typical lifetime of protoplanetary disks (\simeq a few to 10 Myr; see Manara et al. in this book). On the other hand, optical and infrared observations clearly show that μm -sized particles scatter stellar photons from a few gas scale heights above the midplane (Avenhaus et al. 2018; Rich et al. 2021; see also Benisty et al. in this book), indicating that turbulence may drive vertical diffusion of dust. This is the topic of the following subsection.

3.4. Turbulent Diffusion and Dust Concentration

As we mentioned in Section 3.2, particles can drift radially and azimuthally toward local pressure maxima and be trapped therein. However, particle rings and crescents cannot be infinitely thin when turbulence is present; instead, their radial/azimuthal widths are determined by the balance between radial/azimuthal drift and turbulent

³Here, we have used that $St|\eta v_K| \lesssim |v_{g,R}|$ for $St \lesssim \alpha$. For a disk where gas accretion can be described with the viscous stress adopting the dimensionless parameter α introduced by Shakura and Sunyaev (1973), the radial velocity of the gas is given by $v_{g,R} = -(3/2)\alpha c_s (H/R)$. With this, the condition for $St|\eta v_K| \lesssim |v_{g,R}|$ becomes $St \lesssim (3/2)(\alpha/|\eta|)(H/R)^2 = (3/2)(\alpha/d \ln P/d \ln R) \sim \alpha$.

⁴Note that this is because $\Sigma_g \propto R^{-3/2}$ for the MMSN and $t_{\text{sett}} \propto \Sigma_g R^{3/2}$. The radial dependency of the vertical settling timescale changes for different gas surface density profiles.

diffusion (*Dullemond et al. 2018*). In the vicinity of a pressure maximum at radius R_0 with radial width w , whose radial profile is described by a Gaussian function $P(R) = P(R_0) \exp[-(R - R_0)^2/(2w^2)]$, the pressure gradient is $d \ln P/dR = -(R - R_0)/w^2$. Inserting this into Equation (6), at the radial distance ΔR from the pressure maximum, the radial drift velocity is $v_{d,R} \simeq (\text{St}/(\text{St}^2 + 1))(H/w)^2 \Omega \Delta R$ and the drift timescale is $t_{\text{drift}} = |\Delta R/v_{d,R}| \simeq (w/H)^2 (\text{St}^2 + 1)/(\text{St}\Omega)$. As explained in Section 3.2, this radial velocity and drift timescale are applicable to the particles with $\text{St} \gtrsim \alpha$. The radial diffusion timescale is given by $t_{\text{diff},R} = w_d^2/D_{d,R}$, where w_d is the radial width of the dust ring and $D_{d,R}$ is the radial diffusion coefficient for dust, which relates to the radial diffusion coefficient for gas $D_{g,R}$ as $D_{d,R} = D_{g,R}/(1 + \text{St}^2)$ (*Youdin and Lithwick 2007*). From the balance of the two timescales, the width of the dust ring in drift–diffusion equilibrium is given by

$$w_d \simeq \left(\frac{\alpha_R}{\text{St}} \right)^{1/2} w, \quad (8)$$

where $\alpha_R \equiv D_{g,R}/(H^2\Omega_K)$ is the dimensionless radial diffusion coefficient defined in a similar way to the Shakura & Sunyaev α parameter. Similarly, the azimuthal extent of a dust clump that is in drift–diffusion equilibrium, $\Delta\phi_d$, is given by $\Delta\phi_d \simeq (\alpha_\phi/\text{St})^{1/2} \Delta\phi$, where α_ϕ is the dimensionless azimuthal diffusion coefficient and $\Delta\phi$ is the azimuthal extent of the associated gas clump (*Birnstiel et al. 2013; Lyra and Lin 2013*). As seen in the derived relations between the dust and gas widths, the dust substructure has a width comparable to or smaller than the width of the associated gas substructure.

Equation (8) tells us that if we infer w_d from continuum observations and w from molecular line observations, which is possible by measuring the modulation in the rotational velocity of the gas due to pressure gradients (see Equation 5; see also *Teague et al. 2018a*), we can directly obtain the ratio α_R/St . *Rosotti et al. (2020b)* used this method and found that $\alpha_R/\text{St} \sim 0.1$ for three continuum rings in the HD 163296 disk and two continuum rings in the AS 209 disk. Although the Stokes number has uncertainties that arise from the uncertainties in the gas density and the size of particles that the continuum observation is most sensitive to, the estimated α_R/St can put constraints on the degree of radial diffusion. Assuming that the continuum observations probe particles of 1 mm in size, *Rosotti et al. (2020b)* found α_R to be $(1 - \text{few}) \times 10^{-4}$ for the HD 163296 disk.

One can also consider vertical diffusion of solid particles. For a particle layer with a vertical height H_d , the timescale of vertical diffusion is given by $t_{\text{diff},Z} \sim H_d^2/D_Z$, where D_Z is the vertical turbulent diffusion coefficient. In the equilibrium state where vertical diffusion balances settling, we have $t_{\text{sett}} \simeq t_{\text{diff},Z}$ which gives

$$H_d \simeq \left(\frac{\alpha_Z}{\text{St}} \right)^{1/2} H, \quad (9)$$

where $\alpha_Z \equiv D_Z/(H^2\Omega_K)$ is the dimensionless vertical diffusion coefficient. *Pinte et al. (2016)* and *Isella et al. (2016)* measured the vertical thicknesses of the dust rings in the HL Tau and HD 163296 disks from the sharpness of the emission rings and gaps in the ALMA millimeter continuum images. They found that (sub-)mm-sized dust particles are settled substantially, with $H_d \lesssim 1$ au at 100 au, corresponding to α_Z of a few $\times 10^{-4}$. *Doi and Kataoka (2021)* carried out a similar experiment and estimated the vertical thicknesses of the dust rings in the HD 163296 disk (see also *Ohashi and Kataoka 2019*). They found $\alpha_Z/\text{St} > 2.4$ at the 67 au ring and $\alpha_Z/\text{St} < 1.1 \times 10^{-2}$ at the 100 au ring. Assuming that the continuum observations probe particles of 1 mm in size, these numbers correspond to $\alpha_Z > 1.8 \times 10^{-2}$ and $\alpha_Z < 1.8 \times 10^{-4}$, respectively, which might suggest radially varying turbulent diffusion in the disk.

When both the radial width ratio w_d/w and the vertical thickness ratio H_d/H of a ring are measured, we can use them to infer the (an)isotropy of the underlying turbulence: $(H_d/H)/(w_d/w) \simeq (\alpha_Z/\alpha_R)^{1/2}$. Note that the Stokes number, which is often poorly defined as mentioned earlier, cancels out in this relation. Combining the results from *Rosotti et al. (2020b)* and *Doi and Kataoka (2021)* for the continuum rings at 67 and 100 au in the HD 163296 disk, we can infer $\alpha_Z/\alpha_R \gtrsim 10$ for the 67 au ring and $\alpha_Z/\alpha_R \lesssim 0.3$ for the 100 au ring. Such an anisotropy, combined with numerical simulations, may help to determine the origin of the turbulence.

4. Hydrodynamic Processes

Let us now move onto a discussion of substructure-forming mechanisms. To provide a broad visual overview, in Figure 6 we present a three-dimensional pie chart where we illustrate various substructure-forming processes that we will review in this Chapter. Following the way we structure this Chapter, we group different processes into several categories: hydrodynamic processes and gravitational instability (GI), magnetohydrodynamic processes, tidal processes, and processes induced by dust particles.

In this section, we start by introducing hydrodynamic processes that are capable of creating disk substructures. Assuming a smooth disk structure and simple thermodynamics, Keplerian disks should be linearly stable according to the Rayleigh stability criterion ($\partial(R^4\Omega^2)/\partial R > 0$; *Rayleigh 1917*), in the absence of magnetic fields. However, the disk can be unstable when inhomogeneous density structure, more complicated thermodynamics and/or three-dimensionality are considered. Examples include Rossby wave instability (RWI), vertical shear instability (VSI), convective overstability (COS), and zombie vortex instability (ZVI), which we will discuss in the subsections below. In addition to the aforementioned internally-operating processes, there are externally-driven processes that can produce disk substructures such as infall and photoevaporation. In each of the subsections below, we will introduce how the

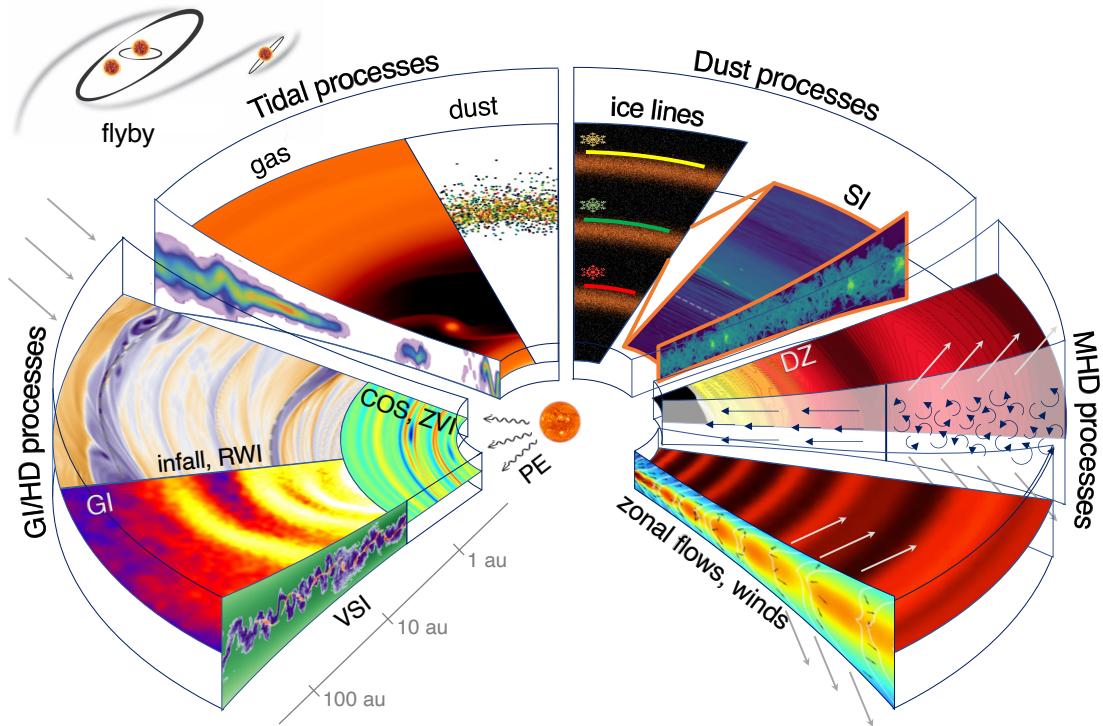


Fig. 6.— A cartoon showing various substructure-forming processes discussed in this Chapter. In the clockwise direction from the left, we present four main categories of substructure-forming mechanisms: hydrodynamic processes (HD, Section 4) including gravitational instability (GI, Section 7; figure from *Rice et al. 2004*), infall and Rossby wave instability (RWI; figure from *Kuznetsova et al. 2022*), convective overstability (COS), zombie vortex instability (ZVI; figure from *Marcus et al. 2015*), photoevaporation (PE), and vertical shear instability (VSI; figure from *Flock et al. 2017b*); tidal processes (Section 6) including planet-disk interaction (figure from *Bae et al. 2019*), stellar companions, and stellar flyby; dust processes (Section 8) including ice lines and streaming instability (SI; figure from *Li and Youdin 2021*); magneto-hydrodynamic processes (MHD, Section 5) including dead-zones (DZ; figure from *Flock et al. 2015*), zonal flows (figure from *Suriano et al. 2018*), and winds. Figures are reproduced by permission of the AAS, A&A, and MNRAS.

process operates, describe under which conditions the process operates, and summarize the properties of the substructures formed by the process. For in-depth discussion on the numerical studies of VSI, COS, and ZVI, we refer readers to the Chapter by *Lesur et al.* in this book.

4.1. Rossby Wave Instability

The RWI arises from a local minimum in the radial profile of the potential vorticity $\eta = \kappa^2 S^{-2/\gamma} / (2\Omega\Sigma_g)$ (*Lovell et al. 1999; Li et al. 2000*), where $\kappa = R^{-3}\partial(R^4\Omega^2)/\partial R$ is the epicyclic frequency, $S = P/\Sigma_g^\gamma$ is the entropy, and γ is the adiabatic index. From its definition, one can see that the radial profile of the potential vorticity is determined by the density, temperature, and orbital frequency of the disk gas, which are related with each other through the radial force balance in Equation (5). Thus, perturbations given to the gas density and/or temperature transition to shear in the rotation velocity in order to maintain the radial force balance. When the velocity shear is sufficiently large, a Kelvin-Helmholtz type instability can arise from

the shear, creating anticyclonic vortices.

Where can such strong radial potential vorticity variations develop in protoplanetary disks? Previous studies showed that they can develop (1) at the edges of MRI-dead zone where the accretion rate can rapidly change (*Varnière and Tagger 2006; Inaba and Barge 2006; Lyra et al. 2008; Lyra and Mac Low 2012; Meheut et al. 2010; Miranda et al. 2017; Pierens and Lin 2018*, see also Section 5.2.1), (2) at the edge of planet-induced gaps where pressure bumps are sustained (*de Val-Borro et al. 2007; Lyra et al. 2009; Fu et al. 2014b,a; Lin 2014; Bae et al. 2016a*), (3) at the edge of the region subject to mass addition via infalling flows onto the disk (*Bae et al. 2015; Kuznetsova et al. 2022*, see also Section 4.6), and (4) between corrugated flows induced by the VSI (*Richard et al. 2016*, see also Section 4.2).

Properties of RWI-induced vortices are often studied by adopting a Gaussian density perturbation to an otherwise smooth disk as an initial condition, with the width and amplitude of the perturbation as variables. *Ono et al. (2016, 2018)* carried out parameter studies using linear sta-

bility analyses and two-dimensional simulations, under a barotropic setup. They showed that disks with a density perturbation of the order of $\Delta\Sigma_g/\Sigma_g \gtrsim 1$ over a radial length scale of the order of the local scale height can become unstable to the RWI. For such perturbations, the RWI grows rapidly with a typical growth timescale of $\sim 10 \Omega^{-1}$. During the linear phase of the instability, the disk region subject to a steep potential vortensity variation breaks into multiple anticyclonic vortices, with the most unstable azimuthal mode number increasing with the strength of the perturbation. As the instability saturates, vortices eventually merge into a single vortex over a typical timescale of $\sim 100 \Omega^{-1}$. For the vortices formed after the final merger, the radial half-width of the vortices has a maximum value of about 2 – 2.5 scale heights (Surville and Barge 2015; Ono et al. 2018). These simulations showed that the aspect ratio ranges from 2 to ~ 20 , although the majority have an aspect ratio in the range 4 – 8. Vortices can survive as long as $\gtrsim 1000$ orbital periods, although their lifetime depends strongly on the level of viscous dissipation (e.g., Lin 2014) or disk turbulence (Zhu and Stone 2014).

As vortices form via the RWI, they can excite spiral waves. While vortices extend within the region that is subsonic with respect to the vortex center, they can perturb the sonic line and launch free traveling waves to the supersonic region (Paardekooper et al. 2010; Ono et al. 2018). After such free waves are launched, their shape (i.e., pitch angle) can be described in the same way as the spirals launched by a planet, which we will discuss in Section 6. However, although the spirals driven by vortices have similar shapes as the ones driven by companions, they are much weaker than planet-driven spirals: the surface density contrast of vortex-driven spirals are comparable to those driven by a subthermal mass planet (typically a few to a few tens of Earth masses; Huang et al. 2019). Thus, spirals driven by vortices are less likely to be observable compared with planetary spirals although whether three-dimensional effects can enhance the strength of vortex spirals at the disk surface needs to be studied in the future. Alternatively, it is possible that a vortex itself may appear as an one-arm spiral in scattered light when viewed at a finite inclination (Marr and Dong 2022).

4.2. Vertical Shear Instability

The VSI is a linear instability originating from vertical gradients in the disk’s rotational velocity (Urpin and Brandenburg 1998; Arlt and Urpin 2004; Nelson et al. 2013). By solving Equation (5) along with a similar equation of force balance in the vertical direction, one can show that vertical differential rotation will always arise unless the disk is globally isothermal, a condition that is very unlikely to be found in protoplanetary disks. Protoplanetary disks thus offer favorable conditions for the VSI to develop. However, the VSI requires rapid gas cooling so that the vertical differential rotation is sustained. When cooling is inefficient, vertical buoyancy stabilizes the vertical gas motion and the

VSI is suppressed (Lin and Youdin 2015). For typical protoplanetary disk conditions, this cooling requirement is met in the outer regions of protoplanetary disks at $\sim 10\text{--}100$ au (Malygin et al. 2017; Pfeil and Klahr 2019). In addition to buoyancy, dust settling and the subsequent back-reaction of the dust on the gas (Lin 2019), dust growth (Fukuhara et al. 2021), and strong magnetic fields (Latter and Papaloizou 2018; Cui and Lin 2021) are known to stabilize the VSI.

When the VSI is fully grown to the non-linear state, the most prominent outcome is nearly axisymmetric vertical corrugation modes (i.e., radially alternating upward and downward gas flows) which have much smaller horizontal wavelengths than vertical wavelengths ($\lambda_R/\lambda_Z \ll 1$; Nelson et al. 2013). Numerical simulations showed that the VSI induces vertical corrugation modes that are as strong as $\sim 10\text{--}100 \text{ m s}^{-1}$ (Flock et al. 2017b, 2020), which are observable using molecular line observations with ALMA (Barraza-Alfaro et al. 2021). Because the VSI predominantly drives vertical gas flows, disks with a low inclination offer favorable conditions for the detection of VSI-driven velocity perturbations. Vertical corrugation modes can cause strong vertical diffusion of dust particles, characterized by $\alpha_Z \simeq 0.01$ (Stoll et al. 2017; Flock et al. 2020). For the disk models considered in Flock et al. (2017b, 2020), mm-sized particles with a Stokes number of about 0.1 are lofted up to $Z/R \sim 0.1$ with a scale height $H_d \simeq 0.03 R$. The perturbed dust distribution manifests as concentric bright rings and dark gaps in radio continuum observations (Flock et al. 2017b; Blanco et al. 2021). However, the perturbations driven by the VSI are intrinsically transient, and particles do not experience long-term trapping or net radial concentration (Flock et al. 2017b) unless they are trapped in VSI-induced vortices.

The velocity perturbations driven by the VSI can give rise to potential vorticity perturbations that break up into vortices (Richard et al. 2016), in a manner that is similar to the RWI introduced in the previous subsection. Recent high-resolution numerical simulations showed that the VSI creates long-lived vortices with a lifetime of $\gtrsim 100$ orbits. The VSI-induced vortices typically have a radial size of about a local gas scale height with an azimuthal size of about 10 local gas scale heights, resulting in an aspect ratio of $\simeq 10$ (Flock et al. 2020; Manger et al. 2020). Note that these aspect ratio values are measured from the potential vorticity of the gas, not from the distribution of solid particles trapped therein, so caution is needed when connecting these simulations to the crescents observed in continuum observations.

4.3. Convective Overstability

The COS is a linear, axisymmetric instability in which radial buoyancy leads to exponential amplification of epicyclic oscillations (Klahr and Hubbard 2014; Lyra 2014). The COS operates when the cooling time of the gas is comparable to the epicyclic oscillation period (\simeq Keplerian timescale), while it is suppressed in the limits of

short and long cooling times: too rapid cooling removes buoyancy, whereas too slow cooling makes the work done on the oscillating gas by the buoyant force over one epicycle vanishingly small. Due to this requirement, the COS can be active around the midplane at $\sim 1 - 10$ au and above the midplane at $r \sim 10 - 100$ au (Malygin et al. 2017; Lyra and Umurhan 2019; Pfeil and Klahr 2019).

Three-dimensional hydrodynamic simulations show that the COS produces a self-sustained, large-scale vortex in its nonlinear saturated state (Lyra 2014; Raettig et al. 2021). Although the vortices initially created by the instability are small, they merge together and form larger vortices. Three-dimensional simulations using a local shearing-box show that eventually a vortex of radial extent $\approx H$ forms (Raettig et al. 2021), although the final vortex size may be affected by the box size. Given that the COS is expected to operate at $\sim 1 - 10$ au, the radial extent of COS-driven vortices would generally be less than 1 au, making it very challenging to observe them using ALMA. As we mentioned earlier, the COS may operate in the surface layers in outer disk regions of $\sim 10 - 100$ au; however, whether the COS triggered at high altitudes can produce vortex columns extending down to the midplane and collect large particles there to produce observable signatures in radio continuum observations will have to be tested in the future.

4.4. Zombie Vortex Instability

The ZVI is another purely hydrodynamic instability that can operate in protoplanetary disks (Barranco and Marcus 2005; Marcus et al. 2013, 2015, 2016). The instability is triggered when the so-called baroclinic critical layers are excited. These baroclinic critical layers are where mathematical singularities exist, and as they are excited the singularities generate vortex layers. The vortices formed in the vortex layers excite new critical layers where additional vortices can form and turbulence arises. This self-replicating nature is why the instability is named the “zombie” vortex instability. Under typical protoplanetary disk conditions, the radial width of the vortex and the spacing between the critical layers are expected to be of order the vertical pressure scale height, with an aspect ratio of $4 - 5$ (Marcus et al. 2015).

The ZVI requires strong vertical buoyancy and cooling times much longer than the Keplerian timescale (Lesur and Latter 2016; Barranco et al. 2018). As such, the ZVI likely operates in the innermost region of protoplanetary disks within $\lesssim 1$ au (Malygin et al. 2017). It is thus unlikely that the crescents observed at tens to hundreds au are associated with the ZVI.

4.5. Eccentric Modes

An eccentric mode refers to the coherent precession of gas on eccentric orbits. Historically, it has been invoked to explain spirals in spiral galaxies (see review by Shu 2016). In a locally isothermal disk, Lin (2015) has shown that eccentric modes can be excited as the background tempera-

ture gradient can exert negative angular momentum to the mode to destabilize it. One of the reasons why eccentric modes are of interest is that they are less susceptible to dissipation process (e.g., viscous dissipation) and can be long-lived (Lubow 1991; Tremaine 2001). The eccentric modes form a single spiral arm in the disk and precess at rates that are much lower than the local orbital frequency Lee et al. (2019). Due to the slow orbital motion, it is expected that the spiral associated with eccentric modes traps small particles only ($St \ll 1$; see Section 3). Lin (2015) showed that spirals associated with eccentric modes satisfy $kR \sim \pi G \Sigma R / c_s^2 \sim 1 / (HQ)$ where k is the wavenumber. With $Q \sim 1$ and $H/R \ll 1$, the spirals are tightly wound with pitch angle $\lesssim 5^\circ$. At this moment, it is unclear if more open spirals can form with the eccentric mode. Eccentric modes can also evolve with time. Simulations by Li et al. (2021) have shown that the spirals become multiple rings over the timescale of several thousands orbits.

4.6. Infall

So far, we have focused on hydrodynamic processes that originate within protoplanetary disks. However, there are important substructure-forming processes that are externally driven. The first example we introduce in this subsection is infalling flows onto the disk. In the traditional rotating singular isothermal sphere model of star and disk formation (Ulrich 1976; Shu 1977; Cassen and Moosman 1981), the rotational velocity of the infalling flow when it reaches the disk midplane at the centrifugal radius (i.e., outer edge of the mass landing on the disk) is the same as the local Keplerian velocity. As a result, the infalling material tends to pile up near the centrifugal radius and create a pressure bump. Using two-dimensional hydrodynamic simulations implementing infall from a rotating singular isothermal cloud, Bae et al. (2015) showed that a strong pressure bump can develop and trigger the RWI near the outer edge of the infall, which, in turn, creates vortices. Kuznetsova et al. (2022) further investigated this scenario by adopting various infall models in which infalling materials have different specific angular momentum. The vortices induced by infall generally share similar properties to other RWI-induced vortices which are summarized in Section 4.1.

When the specific angular momentum of the infalling material significantly differs from that of the disk gas, the mismatch can lead to a rapid redistribution of the infalling gas. Using two-dimensional hydrodynamic simulations, Lesur et al. (2015) showed that such a redistribution can occur via large-amplitude spiral density waves (see also Kuznetsova et al. 2022). These spirals can propagate inward to radii ten times smaller than the radius at which infalling material generates shock to the gas. By numerically solving the ordinary equations in locally isothermal disks under the constraint that the flow must satisfy the Rankine-Hugoniot conditions through the shock, Hennebelle et al. (2016) showed that the pitch angle of infall-driven spirals are generally small, $3 - 9^\circ$ for $H/R = 0.05 - 0.15$. The

dominant azimuthal mode depends on the detailed properties of the infalling flow. A large number of spirals ($\gtrsim 10$) can develop when the infalling flow is axisymmetric (Lesur *et al.* 2015). On the other hand, the $m = 1$ mode can dominate when the infalling flow is asymmetric (Hennebelle *et al.* 2017).

4.7. Photoevaporation

Photoevaporation is another externally driven substructure-forming hydrodynamic process. Since photoevaporation is reviewed extensively in *Protostars and Planets VI*, here we briefly summarize the mechanism and refer readers to Alexander *et al.* (2014) for a more complete review.

The disk can “evaporate” as the gas is heated up by high-energy (UV/X-ray) stellar photons and obtains large enough kinetic energy that exceeds the gravitational binding energy (Bally and Scoville 1982; Shu *et al.* 1993; Hollenbach *et al.* 1994). Whether or not photoevaporation can produce inner cavities or annular gaps depends on the mass-loss rate. Qualitatively speaking, the mass-loss rate via photoevaporation has to be greater than the disk’s accretion rate (at least locally). Once a hole or gap is opened, the inner edge of the outer disk becomes directly exposed to the stellar irradiation. Time-dependent models show that the disk gas is then rapidly cleared from the inside-out on timescales of $10^5 - 10^6$ years, leaving an inner cavity or gap of a few $\times 10$ au in size (Morishima 2012; Bae *et al.* 2013; Kunitomo *et al.* 2020; Ercolano *et al.* 2021). When the X-ray-heated inner edge of the disk becomes dynamically unstable, it is also possible that the disk gas is cleared on much shorter, dynamical time-scales, a process called thermal sweeping (Owen *et al.* 2012). The pressure bump at the inner edge of the outer disk is expected to be strong enough to trap dust particles, which can be observable in (sub-)mm continuum observations (Gárate *et al.* 2021). Due to the expected azimuthal symmetry of stellar irradiation, time-dependent disk evolutionary calculations are commonly carried out adopting one-dimensional radial grids or two-dimensional radial – vertical grids. Whether the pressure bump created by photoevaporation can become unstable to the RWI and generate vortices remains to be examined using multi-dimensional time-dependent calculations including the azimuthal dimension.

5. Magnetohydrodynamic Processes

Although we do not have direct evidence that protoplanetary disks are threaded by magnetic fields⁵ and there exist few constraints on what kind of geometry magnetic fields have, the existence of magnetospheric accretion and jets/outflows suggests that magnetic fields are present at least in some parts of the disk. In addition, theoretical studies show that magnetic turbulence and/or magnetized winds likely play an important role in the dynamical evolution of

protoplanetary disks.

Even when magnetic fields are present, however, the gas disk would interact with them only if the disk is sufficiently ionized and coupled to the magnetic fields. For the most regions in protoplanetary disks, besides the innermost/outermost regions and the surface layers where a sufficient ionization level can be sustained, it turns out that the gas is only weakly ionized so that the ideal MHD assumption of a perfectly conducting fluid breaks down. To provide a broad overview, in a disk around a solar-mass star, it is generally found that ideal MHD is a good approximation within ~ 0.1 au when the disk temperature is above ~ 1000 K, while non-ideal MHD effects, namely Ohmic resistivity, the Hall effect, and ambipolar diffusion, dominate in the inner ($0.1 \text{ au} \lesssim R \lesssim 1 \text{ au}$), middle ($1 \text{ au} \lesssim R \lesssim 10 \text{ au}$), and outer ($R \gtrsim 10 \text{ au}$) disk regions, respectively (see Lesur *et al.* in this book). The exact regions of where each non-ideal effect dominates depends on various factors including the stellar luminosity, the external ionization sources and their strength, and the amount of dust and gas.

In this section, we discuss the ideal and non-ideal MHD processes that can potentially form substructures in protoplanetary disks. Specifically, we focus on the zonal flows that are formed out of an initially unordered flow through the magnetic self-organization process. These banded structures are long-lived and can offer a possible explanation for the observed ringed substructures in protoplanetary disks. We note that the term zonal flow describes the resulting banded structure after it is produced but it does not necessarily ascribe a physical mechanism to its formation. Below, we split the physical mechanisms that can form zonal flows into two subsections: those formed by magnetic turbulence in ideal MHD and those formed by non-ideal MHD processes. We then introduce magnetized winds, which can arise in both ideal and non-ideal MHD regimes and can produce annular substructures.

5.1. Ideal MHD

Balbus and Hawley (1991) showed that the presence of weak magnetic fields in disks can destabilize the disk through the magnetorotational instability (MRI). The MRI drives turbulence and can potentially provide the necessary angular momentum transport to account for observed accretion rates in disks. The physical picture behind the MRI is as follows: when two neighboring fluid elements are coupled by a magnetic field, a small radially inward displacement of one element leads to a magnetic tension force that opposes its rotation, drains its angular momentum, and causes it to drift further radially inward. The angular momentum is transferred to the outer element which moves outward and the process precedes to runaway. Disks are unstable to the MRI so long as the angular velocity increases radially inward and the magnetic field is not strong enough to stabilize the initial perturbation (plasma $\beta \equiv P_{\text{gas}}/P_{\text{magnetic}} \lesssim 1$).

⁵Some tentative evidence was recently found from circular polarization measurements of molecular lines (see Teague *et al.* 2021).

5.1.1. Zonal flows

In ideal MHD turbulence, ring structures were noted early in the global simulations of [Hawley \(2001\)](#). Their simulations showed that initially small radial variations of the Maxwell stress ($B_R B_\phi / 4\pi$) over the largest scales of the simulation domain can eventually lead to the concentration of gas into rings. [Hawley \(2001\)](#) explained this as increasing accretion efficiency with decreasing density. Local shearing box simulations have been carried out to explore the zonal flows ([Johansen et al. 2009](#); [Bai and Stone 2014](#)). In simulations from [Johansen et al. \(2009\)](#), zonal flows are initially launched by Maxwell stress fluctuations that are as small as 10% compared to the background. The resulting pressure bumps are in a geostrophic balance with sub/super-Keplerian zonal flows, and they can grow to fill up the largest scale of the simulation box, as large as 10 gas scale heights. These structures can live 10 – 50 orbital periods, and the lifetime increases with the simulation box size. It is unclear if the zonal flow structure eventually converges with the box size ([Simon et al. 2012](#); [Bai and Stone 2014](#)). Recent global simulations ([Zhu et al. 2015a](#); [Jacquemin-Ide et al. 2021](#)) show the formation of ring structure in disks threaded by net vertical magnetic flux. But we need to caution the potential influence from the inner boundary condition in these global simulations.

5.1.2. Spirals

Magnetohydrodynamic turbulence in disks can generate spirals. Since turbulence is generally homogeneous along the azimuthal direction (except for large scale vortices), higher mode spirals are excited. The number and strength of excited spirals depends on the properties of the turbulence. For the MRI, spirals are generated when a wave swings from leading to trailing ([Heinemann and Papaloizou 2009a,b](#)) and the maximum coupling occurs when the perturbation’s azimuthal wavelength is $2\pi H$. If we assume that a perturbation at the $2\pi H$ azimuthal length scale will excite one spiral arm, then the disk will excite $m \sim R/H$ spirals, which is generally of order of ~ 10 . In agreement with the prediction, global MHD simulations suggest that the kinetic energy spectra and the velocity spectra peak for an azimuthal wavenumber between $m = 3$ and ~ 10 ([Flock et al. 2011](#); [Suzuki and Inutsuka 2014](#)). Note that, in general, $m = 2$ modes are not the dominant mode in MRI turbulent disks.

5.2. Non-ideal MHD

5.2.1. Dead-zones

[Gammie \(1996\)](#) found that Ohmic resistivity in the inner (~ 1 au) regions of protoplanetary disks can make disks stable against the MRI, although the surface layers may still be sufficiently ionized for the MRI to drive accretion. The mid-plane region where the MRI is inactive is called the “dead-zone”.

Pressure bumps can form at the inner/outer edge of dead-zones due to the mismatch in the accretion efficiency be-

tween the MRI active and dead zones. Interior/exterior to the pressure bumps at the inner/outer edge, gaps can open again due to the mismatch in the accretion rate (see the dead-zone in the MHD section in [Figure 6](#)). The density contrast across the transition from the MRI-active region to the dead-zone is typically a few, large enough to trigger the RWI which in turn can generate vortices ([Lyra and Mac Low 2012](#); [Lyra et al. 2015](#); [Flock et al. 2015, 2017a](#)). Simulations by [Ruge et al. \(2016\)](#) showed that dust grains with a size of up to 1 cm can be trapped at the edge of the dead-zone, and large grains ($\gtrsim 50 \mu\text{m}$) eventually concentrate into vortices on timescales of ~ 20 local orbits. The location of the inner edge of the dead-zone is determined mainly by the stellar luminosity, such that it lies close to the star at about 0.1 au for T Tauri stars while it can be as far as 1 au for Herbig stars ([Flock et al. 2016, 2019](#)). Due to the radial location and associated small physical sizes, rings or vortices at the inner dead-zone edge are unlikely to be observable with ALMA. The location of the outer edge of the dead-zone is determined by and sensitive to the ionization state of the disk and the gas and dust density ([Dzyurkevich et al. 2013](#); [Turner et al. 2014](#); [Lyra et al. 2015](#); [Flock et al. 2015](#)). Depending on those parameters, rings or vortices at the outer dead-zone edge can be observed using ALMA (e.g., [Flock et al. 2015](#)).

5.2.2. Hall effect

The “dead-zone” picture has been significantly modified with the inclusion of the Hall effect and ambipolar diffusion in recent years. [Kunz and Lesur \(2013\)](#) found that in the non-linear saturated state of the Hall-dominated MRI turbulence, large-scale axisymmetric pressure bumps can arise through zonal flows. Their simulations showed that zonal flows will develop when the Hall length (the ratio of the Hall diffusivity to the Alfvén speed, $l_H = \eta_H / v_A$) is a significant fraction of the gas scale height ($l_H \gtrsim 0.2H$). In vertically unstratified global simulations, the number of zonal flows is found to increase as the Hall effect becomes stronger ($l_H > H$) and zonal flows have typical widths of $\sim H$ ([Béthune et al. 2016](#)). The vertically stratified simulations of [Bai \(2015\)](#) showed that zonal flows are launched when the Hall length increases, but they suggested that zonal field concentrations are merely an inevitability of MRI turbulence in stratified simulations with an initial net vertical magnetic flux. The zonal flows formed in global simulations are capable of trapping dust grains in magnetic flux concentrations with dust density enhancements of ~ 20 times over the initial profile ([Krapp et al. 2018](#)).

5.2.3. Ambipolar diffusion

The formation of zonal flows in disks where only ambipolar diffusion operates have been seen in the shearing-box simulations of [Bai and Stone \(2014\)](#) and in the global three-dimensional simulation of [Béthune et al. \(2017\)](#). The exact reason for the formation of zonal flows in ambipolar diffusion-dominated regions is still not fully understood and

deserves future studies. It has been shown that magnetic flux concentrations can form as a result of the reconnection of radial magnetic fields along a midplane current layer where B_ϕ changes sign, steepened by the effects of ambipolar diffusion (Suriano *et al.* 2018, 2019; Hu *et al.* 2019). The reconnection of magnetic fields in a well-defined current sheet at the disk midplane is aided by the presence of strong magnetic fields and large ambipolar diffusivities (Brandenburg and Zweibel 1994).

In non-ideal MHD simulations with strong ambipolar diffusion, Bai and Stone (2014) found that magnetic flux concentrates into thin shells whose width is typically less than $\sim 0.5H$ (see also Simon and Armitage 2014). In shearing box simulations that include dust grains, grains are effectively trapped in the zonal flows and are concentrated into thin radial bands. Small grains ($St = 0.001$) have dust density contrasts of ~ 2 , while large grains ($St = 0.1$) can have density contrasts of order 10^3 (Riols and Lesur 2018). The width of the rings is about $1 - 2H$ and the separation between the rings is of order of $3 - 4H$; however, these properties depend on the plasma β . In their simulations, zonal flows and radial pressure profiles are found to remain almost steady within the simulation timescale (~ 100 orbits). Using 3D shearing box simulations, Riols and Lesur (2019) showed the development of a linear and secular instability driven by MHD winds, which gives birth to long-lived (a few hundred to thousand orbits) rings of sizes $> H$ with typical ring separations of $\sim 10H$. The linear instability for the spontaneous formation of rings in disks with large-scale vertical magnetic fields is able to predict ring density contrast at given magnetic field strengths (Riols and Lesur 2019).

The global axisymmetric simulations by Riols *et al.* (2020) showed that 0.1 mm and 3 mm dust grains accumulate in the gaseous rings formed from MHD winds with ambipolar diffusion, and the separation between dust rings is $2.5H$ for $\beta = 10^4$ and $4H$ for $\beta = 10^3$ near $R = 20$ au. They also find the half-width of the 3-mm dust rings is $0.3H$ at $R = 20$ au for $\beta = 10^3$ and $0.15H$ for $\beta = 10^4$, whereas the gas rings have a half-width of $1.2H$. Gaseous rings are formed at smaller contrast when $\beta = 10^5$, but dust grains do not accumulate in them. Cui and Bai (2021) also observe the spontaneous concentration of magnetic flux into axisymmetric bands in global 3D simulations of the outer regions of protoplanetary disks with ambipolar diffusion. The simulations are capable of resolving the MRI, and the disks both launch winds and have active MRI turbulence. Zonal flows form stochastically and are not as long-lived as previously seen in less resolved simulations that explore a similar parameter space. In their fiducial model they find ring/gap widths of $1.5 - 2.5H$ and surface density contrasts between rings and gaps of 15–50%, while ring/gap widths can vary from 1 to $5H$ over a range of ambipolar Elsässer numbers and for $\beta = 10^4$ and 10^3 . Above a magnetic field strength corresponding to $\beta > 10^5$, the zonal flows vanish. Similar zonal flows and particle concentration have also been seen in Hu *et al.* (2022). In addition, Hu *et al.* (2022)

found significant meridional circulation that resemble to the observed meridional flows in the HD 163296 disk (Teague *et al.* 2019).

5.3. Magnetized Winds

For both ideal and non-ideal MHD simulations, a magnetocentrifugal wind can be launched if the disk is threaded by net vertical magnetic fields (Blandford and Payne 1982). Magnetocentrifugal winds can extract angular momentum by exerting a torque in opposition to the disk rotation, called the magnetic breaking torque. Although this breaking torque may not be as important as the MRI turbulent stress that transports angular momentum in ideal MHD disks (Zhu and Stone 2018), it may be essential for accretion in disks dominated by non-ideal MHD effects (Bai and Stone 2013).

Accretion due to wind launching can potentially lead to structure formation (Moll 2012). For disks in both ideal and non-ideal MHD limits, a linear magnetic wind instability has been found to explain the formation of rings and gaps in stratified shearing box simulations (Riols and Lesur 2019). Qualitatively, the instability can be described as follows. If magnetic diffusivity is not too large, magnetic flux will be transported with the viscous flow radially away from a local overdensity in the disk, and therefore concentrate towards disk regions with lower density. Thus, the increased magnetic flux at less diffuse gaps will also lead to an increased angular momentum removal rate in the wind, and the instability grows if more mass is removed in the wind than can be replenished into the gap.

An MHD disk wind can lead to a localized gap if the disk wind depletion timescale is shorter than the viscous accretion timescale, i.e., gas is lost in the wind before it can be replenished from larger radii (Suzuki *et al.* 2016). Then, dust can concentrate in the resulting pressure maximum outside of the gas gap only when the radial dust drift timescale is comparable or shorter than the wind depletion time. Takahashi and Muto (2018), for example, found that this can be satisfied for grains of size $St = 0.1$ which form a ~ 10 au wide gap near 20 au, given a disk viscosity of $\alpha \sim 10^{-4}$.

6. Tidal Interaction with Perturbers

The ubiquity of planetary systems around main sequence stars suggests that planet formation must commonly happen. As a planet grows, the tidal interaction between the planet and its natal disk perturbs the gas and solids in the disk. This perturbation is observable with modern observing facilities. Tidal interaction with stellar-mass bodies – both gravitationally bound companions and gravitationally unbound, flyby perturbers – can also produce observable signatures. In this section, we summarize the mechanism and outcome of tidal interactions with perturbers.

6.1. Gravitationally Bound Planetary and Stellar Companions

6.1.1. Excitation of spiral waves

The interaction between a companion and its host disk starts with the excitation of spiral waves, which can be described well with linear theory (Goldreich and Tremaine 1978, 1979; Ogilvie and Lubow 2002; Bae and Zhu 2018a; Miranda and Rafikov 2019). A companion launches wave modes at the Lindblad resonances through the resonance between the rotation of the companion's potential and the epicyclic motion of the disk gas (Goldreich and Tremaine 1978, 1979). In Keplerian disks, the propagation of wave modes depends on the azimuthal wavenumber in such a way that different azimuthal wave modes can constructively interfere with each other and create a coherent structure – a spiral arm (Ogilvie and Lubow 2002). It is also possible that a companion can excite multiple spiral arms because such constructive interference can occur for multiple sets of wave modes (Bae and Zhu 2018a,b).

Using two-dimensional hydrodynamic simulations, Bae and Zhu (2018b) investigated how the number and pitch angle of companion-driven spirals vary as a function of the disk temperature and companion mass. In general, a smaller number of spirals form with larger companion mass and higher disk temperature (Bae and Zhu 2018b). For companions with at least a Saturn-mass (around a solar-mass star), it is expected that 2 – 3 spirals are excited inside the companion's orbit and 1 – 2 spirals are excited outside the companion's orbit, with the exact number depending on the disk temperature. Important characteristics of Lindblad spirals include that the pitch angle peaks at the location of the planet and quickly decreases away from the planet (Rafikov 2002; Muto et al. 2012), and the spirals are more opened up with a higher mass planet due to the non-linear wave propagation (Zhu et al. 2015b; Bae and Zhu 2018a,b, see also Figure 6 of this Chapter). By measuring the pitch angle of a spiral over a broad range of disk radii, these characteristics can thus help to determine the location and mass of the planet.

While many seminal works on planet-disk interaction adopted an isothermal assumption (see PPVI review by Baruteau et al. 2014), recent studies have highlighted the importance of using more realistic disk thermal properties (see Paardekooper et al. in this book). Using linear theory and two-dimensional hydrodynamic simulations, Miranda and Rafikov (2020) and Zhang and Zhu (2020) showed that disk's cooling timescale can play an important role in the dissipation of companion-driven spirals. They showed that when the cooling timescale is of order of the dynamical timescale ($t_{\text{cool}} \sim 1/\Omega$), the amplitude of companion-driven spirals greatly decreases as the density waves are subject to a strong radiative dissipation. The observational implications of spirals subject to different cooling timescales are presented in Speedie et al. (2022). Although the intrinsic number of spirals a companion excites does not depend on the disk's cooling timescale, these stud-

ies suggest that the number of *observable* spirals can be smaller depending on the cooling timescale.

Another important development in recent years is the use of three-dimensional simulations. As we mentioned in Section 2.3.2, spirals are more frequently observed in NIR than mm continuum observations. It is thus important to understand that the pitch angle of companion-driven spirals in the surface layers (probed with NIR observations or optically thick molecular lines in mm wavelengths) can be different from the pitch angle in the midplane (probed with mm observations). Using three-dimensional numerical simulations adopting vertically stratified temperature structure, Juhász and Rosotti (2018) showed that the pitch angle of the spirals in thermally stratified disks is the smallest in the disk midplane and increases towards the disk surface, by approximately the ratio of the sound speed between the layers: $\psi(z)/\psi(z=0) \simeq c_s(z)/c_s(z=0)$. When the disk is thermally stratified and/or cooling is slow, the disk can have non-zero vertical buoyancy frequency. In such a case, companions can excite spirals via buoyancy resonances (Zhu et al. 2012b; Lubow and Zhu 2014; McNally et al. 2020; Bae et al. 2021; Yun et al. 2022), in addition to those driven by Lindblad resonances. Buoyancy resonances occur when the companion's orbital frequency and the buoyancy frequency match with each other. Buoyancy spirals have several characteristics which distinguish themselves from Lindblad spirals. These include that (1) buoyancy spirals are much more tightly wound compared with Lindblad spirals, with a pitch angle $\lesssim 10^\circ$ in the vicinity of the companion; (2) their pitch angle monotonically decreases over the disk radius; and (3) they predominantly produce vertical velocity perturbations.

Regardless of the companion mass and disk properties, companion-driven spirals (via both Lindblad and buoyancy resonances) orbit at the companion's orbital frequency. As such, only small particles with a sufficiently short stopping time may be trapped by companion-driven spirals (see Section 3.2). This might support the fact that spirals are more commonly seen in NIR scattered light observations than mm continuum observations. While larger grains generally do not couple to spiral, they (as well as small grains) can experience vertical stirring arising from the turbulence and vertical flows induced by companion-driven spirals. Bae et al. (2016b,c) showed that companion-driven spirals can undergo the spiral wave instability (SWI), a parametric instability arising from the resonant coupling between spiral waves and pairs of inertial waves. When the SWI is saturated corrugated vertical flows develop, which can loft dust particles from the midplane (Bae et al. 2016b,c, see also the vertical slice in the tidal processes section in Figure 6). Bae et al. (2016c) showed that a Jupiter-mass planet in a MMSN-like disk can produce significant vertical diffusion of dust particle, corresponding to a diffusion coefficient $\alpha_Z \simeq 10^{-3} - 10^{-2}$. More recent three-dimensional multi-fluid simulations also showed that giant planets can induce significant vertical stirring of particles (Bi et al. 2021; Binkert et al. 2021), although whether the SWI is the

origin of the vertical stirring seen in these simulations is unclear at this point.

Finally, spirals excited by an eccentric perturber have been studied recently (*Zhu and Zhang 2022b*; *Fairbairn and Rafikov 2022*). These spirals are highly complicated: they can detach from the planet, bifurcate, break, or even cross each other. The pitch angle and pattern speed are different between different spirals and can vary significantly across one spiral. These properties are very different from those of spirals driven by a planet on a circular orbit, and can help us to find perturbers on eccentric orbits in future observations.

6.1.2. Gap opening

While the initial excitation of companion-driven spirals is well described with linear theory, companion-driven spirals non-linearly steepen to shocks as they propagate (*Goodman and Rafikov 2001*; *Cimerman and Rafikov 2021*). As spiral waves generate shocks, angular momentum is transferred to the disk gas, opening a gap (*Rafikov 2002*). For low-mass companions whose masses are smaller than the so-called thermal mass, defined as $M_{\text{th}} \equiv (H/R)_p^3 M_*$ where $(H/R)_p$ is the disk aspect ratio at the location of the companion, spiral waves have to propagate before they steepen into shocks (*Goodman and Rafikov 2001*). This means that gaps open at finite distance from the companion, while the planet is still embedded in its co-orbiting region (*Dong et al. 2017*). When a companion excites multiple spirals, it is possible that the companion carves multiple gaps in the disk as each of its spiral opens a gap (*Bae et al. 2017*; *Dong et al. 2017, 2018a*). When a companion reaches a thermal mass, the spiral waves launched by the companion are already non-linear at excitation. Such massive companions can thus carve a gap around their orbit. As a reference, for a solar-mass host star, a thermal mass is about 0.5 times Saturn’s mass when $(H/R)_p = 0.05$, about a Jupiter mass when $(H/R)_p = 0.1$, and about 3 Jupiter masses when $(H/R)_p = 0.15$.

The depth and width of the gap a companion opens depend on the mass of the companion, in addition to the disk temperature and viscosity. Thus, when gap properties are constrained from observations, one can use the properties to infer the mass of the companion (see Section 10). The scaling relation between the companion mass, disk temperature, and disk viscosity, and the gap width/depth can be derived analytically by considering the angular momentum exchange between the disk and the companion (*Fung et al. 2014*; *Kanagawa et al. 2015a,b*; *Ginzburg and Sari 2018*) or empirically by carrying out numerical simulations (e.g., *Duffell and MacFadyen 2013*; *Fung et al. 2014*; *Kanagawa et al. 2016*; *Dong and Fung 2017*; *Kanagawa et al. 2017*; *Zhang et al. 2018*; *Yun et al. 2019*). Under the assumption that the disk accretion can be described with the viscous theory adopting α viscosity (*Shakura and Sunyaev 1973*), *Kanagawa et al. (2015a)* analytically derived the gap depth as

$$\Sigma_p/\Sigma_0 = \frac{1}{1 + 0.04K_d}, \quad (10)$$

where Σ_p and Σ_0 denote the perturbed and unperturbed surface density, respectively, and $K_d \equiv \alpha^{-1} (H/R)_p^{-5} (M_p/M_*)^2$. While the above relation is derived assuming that the angular momentum deposition occurs locally, within about a scale height from the companion’s radial location, it is also possible to consider additional non-local deposition of angular momentum in the gap width and depth derivation (*Ginzburg and Sari 2018*). Strictly speaking, the scaling relations derived analytically can be applicable to low-mass planets only. For high-mass planets, non-linear effects can become important, and numerical simulations can complement the scaling relations. In general though, empirical scaling relations obtained from numerical simulations show a reasonable match to the above analytic formula, within the planetary mass regime (see e.g., *Fung et al. 2014*; *Kanagawa et al. 2015b*; *Zhang et al. 2018*; *Yun et al. 2019*). When the planet is misaligned with the disk, the gap will be shallower and a similar gap depth formulae can be derived and tested against simulations (*Zhu 2019*).

Beyond the gap within which a companion is embedded, a local pressure maximum forms, trapping grains. Numerical simulations show that the width of the gas ring, measured as the full width at half maximum in the perturbed surface density profile Σ/Σ_0 , is $\sim 2 - 4 H$. In the PDS 70 disk, where two giant planets are detected within its inner cavity (*Kepler et al. 2018*; *Haffert et al. 2019*), the continuum ring beyond the orbit of PDS 70c has a width of about 35 au measured at the half-maximum of the peak flux density, corresponding to about 3 gas scale heights (*Kepler et al. 2019*). This agrees well with the gas ring width seen in numerical simulations.

Companion-induced rings and gaps are generally stable but the number and location of rings and gaps can vary when planets undergo orbital migration, with the details depending on the migration speed (*Meru et al. 2019*; *Nazari et al. 2019*; *Weber et al. 2019*; *Kanagawa et al. 2020, 2021*). For a planet migrating slower than the dust, a dust ring forms outside of the planet’s orbit, whereas if the planet migrates faster than the dust the ring appears inside of the planet’s orbit (*Meru et al. 2019*; *Nazari et al. 2019*). If the radial drift velocity of the dust can be estimated, for example via the spectral index of the millimeter emission, the continuum morphology can thus be used to constrain the planet migration speed. When planets undergo intermittent orbital migration, it can also leave multiple rings and gaps behind them (*Wafflard-Fernandez and Baruteau 2020*, see also *Paardekooper et al.* in this book).

While it is generally believed that stellar companions are too massive to create narrow, axisymmetric gaps in protoplanetary disks, stellar companions can tidally truncate the inner disk, open a large inner cavity, and create a ring beyond the cavity (*Artymowicz and Lubow 1994, 1996*). The size of the cavity depends upon the eccentricity of the binary and the inclination of the disk to the binary orbital plane (*Miranda and Lai 2015*; *Lubow et al. 2015*; *Lubow and Martin 2018*; *Franchini et al. 2019a*). For a coplanar disk, the inner cavity size is in the approximate range

1.8–3.3 a_b for eccentricity in the range 0–1, where a_b is the semi-major axis of the binary orbit.

6.1.3. Disk breaking and misalignment

While companions in highly viscous disks can cause the disk to warp (e.g. [Xiang-Gruess and Papaloizou 2013](#); [Arzamasskiy et al. 2018](#); [Nealon et al. 2019](#)), massive planetary companions and stellar companions in less viscous disks can induce deep gaps to break the gas disk and produce misalignments between different parts of the disk (e.g. [Zhu 2019](#); [Bi et al. 2020](#)). With a deep gap satisfying the disk breaking condition in [Zhu \(2019\)](#), the planet effectively separates the disk into disjoint regions that are not in communication with each others. If the disk is broken into disjoint rings, the misaligned rings can then nodally precess independently. The timescale for the precession depends upon the radius of the disk ring and so the precession can lead to a large misalignment between the different parts of the disk (e.g. [Lubow and Martin 2018](#)).

While we expect most planets to form coplanar to their parental disk, their dynamics can deviate from the disk. This is particularly efficient when the planet is sufficiently massive to open a gap in the circumstellar disk in binary systems ([Picogna and Marzari 2015](#); [Lubow and Martin 2016](#)). Around one component of a binary, planet-disk interactions lead the inclination of a planet to increase on average. Even a small misalignment can lead to a highly inclined planet that may be able to undergo Kozai-Lidov oscillations ([Kozai 1962](#); [Lidov 1962](#); [Martin et al. 2016](#); [Franchini et al. 2020](#)). In a circumbinary disk, planet-disk interactions have similar effects, although an outer disk generally leads to the planet tilt decreasing on average ([Pierens and Lin 2018](#)).

The disk inclination relative to an inner binary or an outer binary companion can evolve over the lifetime of the disk. Circumstellar disks and low inclination circumbinary disks nodally precess about the binary angular momentum vector ([Papaloizou and Lin 1995](#); [Lodato and Facchini 2013](#)). Circumstellar disks generally precess as a solid body since the sound crossing timescale is short compared to the global disk precession timescale ([Larwood et al. 1996](#)). Circumbinary disks that are sufficiently extended in radius may be subject to disk warping or even breaking as a result of the precession ([Nixon et al. 2013](#); [Facchini et al. 2013](#); [Juhász and Facchini 2017](#); [Facchini et al. 2018](#); [Price et al. 2018b](#)). For highly inclined circumbinary disks around an eccentric binary the precession is about the binary eccentricity vector (or semi-major axis) ([Verrier and Evans 2009](#); [Farago and Laskar 2010](#); [Doolin and Blundell 2011](#); [Aly et al. 2015](#)).

A circumstellar disk with a sufficiently high inclination can undergo Kozai-Lidov ([Kozai 1962](#); [Lidov 1962](#)) oscillations where the disk inclination and eccentricity are exchanged ([Martin et al. 2014](#); [Fu et al. 2015](#)). This can lead to highly eccentric disks and mass transfer between binary components ([Franchini et al. 2019b](#)). Since a highly misaligned circumbinary disc provides a source of high incli-

nation material to the circumstellar discs, these oscillations may be long lived ([Smallwood et al. 2021](#)).

Dissipation within a disk during nodal precession causes a circumstellar disk to move towards coplanar alignment ([Lubow and Ogilvie 2000](#); [Nixon et al. 2011](#); [Foucart and Lai 2013](#)). A circumbinary disk moves either towards coplanar alignment or towards polar alignment depending on its initial inclination ([Martin and Lubow 2017](#); [Zanazzi and Lai 2018](#)). A polar aligned low-mass disk has its angular momentum vector aligned to the binary eccentricity vector. The disk is perpendicular to the binary orbital plane. A massive circumbinary disk reaches a polar aligned stationary state at lower levels of misalignment ([Zanazzi and Lai 2018](#); [Martin and Lubow 2019](#); [Chen et al. 2019](#)). There have been two observed polar disks, a polar gas disk ([Kennedy et al. 2019](#)) and a polar debris disk ([Kennedy et al. 2012](#); [Smallwood et al. 2020](#)).

The alignment timescale for a disk depends upon a few parameters. First, it depends on the nodal precession timescale. The shorter the precession timescale, the shorter the alignment timescale. For an external binary companion, the closer the companion, the faster the precession and the shorter the alignment timescale. This is why disks in closer binaries tend to be aligned while those in wider binaries may be misaligned ([Czekala et al. 2019](#)). The more radially extended a circumbinary disk is the longer the alignment timescale. Further, the alignment timescale also increases with the disk aspect ratio and decreases with the Shakura & Sunyaev α parameter ([Lubow and Ogilvie 2000](#); [Bate et al. 2000](#)). Thus, depending on the properties of the disk and binary, the lifetime of the disk may be shorter than the alignment timescale meaning that planet formation may occur in misaligned disks ([Martin et al. 2016](#)).

6.1.4. Vortex formation

As a planet opens a gap, the rotational velocity of the protoplanetary disk evolves to maintain the radial force balance (Equation (5)). The resulting sharp velocity shear can trigger the Rossby wave instability and form vortices. The properties of vortices formed through this process are expected to be similar to the vortices formed in more generalized simulations of RWI adopting a Gaussian density perturbation which we discussed in Section 4.1.

Vortices can also be generated at the inner edge of circumbinary disks (e.g., [Price et al. 2018a](#)). Although vortices in circumbinary disks share some similarities with the ones created by planets at the gap edge, they seem to be more closely linked to the spirals launched by the binary stars and the eccentric gap edge ([Shi et al. 2012](#); [Ragusa et al. 2017](#)). When the vortices move close to the binary, material streams to the binary and then flung out back to the disk edge, enhancing the vortices. Even in disks with high viscosity or MHD turbulence and even when the binary orbit is circular, asymmetric over-densities can appear when the gap edge starts to become eccentric ([Muñoz and Lithwick 2020](#); [Ragusa et al. 2020](#)). The discovery of the

crescents in circumbinary disks (Figure 5a) seems to support that at least some crescents could be induced by the binary.

6.2. Stellar Flybys

The great majority of local star formation happened in groups and clusters of tens to hundreds members, embedded within their natal (giant) molecular clouds (e.g., *Carpenter 2000; Lada and Lada 2003; Evans et al. 2009*). It is also believed that our very own star, the Sun, was born in a cluster (see e.g., reviews by *Adams 2010*). The presence of nearby stars can greatly affect the dynamics of the stars themselves, but also the formation and evolution of their disks because the disks can be tidally perturbed or even truncated during close encounters.

The most common observable from flyby events is the formation of spirals. The spiral formation mechanism via stellar flybys can be understood in a similar way that a gravitationally bound companion excites spirals, except that the location of the external potential relative to the disk can rapidly change. In general, numerical simulations show that a stellar flyby produces grand-design, two-armed spirals, consisting of one that is connected to the perturbing star and the other that forms on the opposite side. The fact that $m = 2$ mode dominates is sensible given the large perturber mass (*Bae and Zhu 2018b*). Flyby-induced spirals generally have large pitch angles of $20 - 30^\circ$ during the encounter, which subsequently moderates to $\sim 10 - 20^\circ$ (*Cuello et al. 2019*). Spirals driven by a stellar flyby are expected to disappear once the close encounter is over, typically after a few thousand years (*Cuello et al. 2019*).

7. The Effect of Self-gravity

So far, we have ignored the effects of the disk’s self-gravity. However, when the disk is sufficiently massive, self-gravity of the disk can trigger gravitational instability, change the disk’s underlying structure (e.g., make the disk thinner), or affect the outcome of other substructure-forming processes. In this section, we first describe gravitational instability in Section 7.1, and then we discuss the influence that self-gravity can have on other substructure-forming processes in Section 7.2.

7.1. Gravitational Instability

In a uniform gaseous medium, perturbations on large scales can grow and collapse when the self-gravity of the gas overcomes the gas pressure – the so-called Jeans instability. In rotating systems like protoplanetary disks, gas pressure can stabilize perturbations on small scales, similar to the Jeans instability, while rotation can stabilize perturbations on large scales. When the disk is sufficiently massive such that the so-called Toomre $Q \equiv c_s \Omega / (\pi G \Sigma)$ parameter (*Toomre 1964*) is $\lesssim 1$, the small and large scales separate from each other and perturbations at intermediate scales are subject to GI (see review by *Kratter and Lodato 2016*).

In order to have a small Q close to unity, the disk needs to be massive (large Σ) and/or cold (small c_s). Since protoplanetary disks experience significant mass infall during early protostellar stages and lose mass over their lifetime, it is likely that protoplanetary disks are more prone to GI while they are young. If we assume that the disk temperature is dominated by stellar irradiation, then the temperature drops as $T \propto R^{-1/2}$. Adopting a radially decreasing surface density profile $\Sigma \propto R^{-1}$, Q therefore varies as $Q \propto R^{-3/4}$, indicating that the outer disk is generally more prone to GI. Indeed, numerical simulations of protoplanetary disk subject to infall suggest that young protoplanetary disks (< 1 Myr) can be subject to GI at large radii of $R \gtrsim 10$ au (e.g., *Vorobyov and Basu 2005; Bae et al. 2014; Xu and Kunz 2021a,b*).

For a disk with $Q \lesssim 1$, GI quickly leads to the formation of non-axisymmetric spirals which can efficiently transport angular momentum through gravitational torques. GI-driven spirals can also produce turbulence which can transport angular momentum. Angular momentum transport is accompanied by energy dissipation in the disk so that the disk heats up, increasing Q and stabilizing the instability. When Q becomes much larger than 1, GI does not operate in the disk, the disk cools down, and Q decreases. Eventually, the heating and cooling are balanced such that Q is maintained around 1. In this regard, GI can be seen as a thermally self-regulated instability with the Toomre Q staying around 1. However, GI does not always lead to stable spirals in disks. Depending on the disk’s cooling rate, the spirals can collapse to form bound objects (e.g. giant planets; *Gammie 2001; Rice et al. 2003, 2005; Cossins et al. 2009*). Traditionally, the orbital cooling parameter (β cooling) has been adopted to quantify the cooling efficiency (*Gammie 2001*). When the cooling timescale is shorter than the orbital timescale, a condition that is generally easier to be met at large distances $\gtrsim 50$ au, the GI-driven spirals can collapse to form bound clumps (*Rafikov 2005; Cossins et al. 2010b; Zhu et al. 2012a*). This is the competing mechanism for giant planet formation far away from the central star (*Boss 1997*), besides the core accretion mechanism. The exact cooling criterion for clump formation is still being actively studied, including its numerical convergence (*Meru and Bate 2011; Lodato and Clarke 2011; Paardekooper 2012; Booth and Clarke 2019*), different viscosity and cooling treatments (*Rice et al. 2012; Michael et al. 2012; Rice et al. 2014; Baehr and Klahr 2015; Hirose and Shi 2019; Vorobyov et al. 2020*), and relationship to the disk’s local condition (*Rogers and Wadsley 2012; Takahashi et al. 2016*).

The main observable outcome of GI is spirals. Similar to spirals driven by other processes, one can characterize GI-driven spirals using the pitch angle and multiplicity. *Cossins et al. (2009)* carried out smoothed particle hydrodynamics (SPH) simulations to study GI-driven spirals in disks with different masses and cooling timescales. The dominant azimuthal mode and the pitch angle are found to be more sensitive to the disk mass than the cooling time.

When $M_d/M_* = 0.05$, the $m = 14$ mode dominates with a pitch angle of about 10° . When $M_d/M_* = 0.125$, the disk has $m = 9$ with a pitch angle of 14° . When the disk becomes more massive with $0.25 < M_d/M_* < 1.5$, the $m = 2$ mode dominates (Forgan *et al.* 2011; Hall *et al.* 2019). Thus, $M_d/M_* \sim 0.2$ is roughly the boundary above which $m = 2$ mode dominates.

GI-driven spirals are generally transient. Spirals can constantly form and disappear, typically within the orbital timescale. Even within one orbital timescale, the spirals can self-adjust so that the normal flow speed into spiral the arms is sonic (Cossins *et al.* 2009; Béthune *et al.* 2021). This suggests that the pattern speed of the spirals Ω_p is generally close to the local angular velocity of the flow $\Omega \simeq \Omega_K$. Indeed, numerical simulations showed that $|\Omega_p - \Omega|/\Omega < 15\%$ for disks with $M_d/M_* \leq 0.125$, although $|\Omega_p - \Omega|/\Omega \gtrsim 50\%$ when the disk-to-star mass ratio exceeds 0.5 (Forgan *et al.* 2011). However, we note that most GI simulations start with a globally gravitationally unstable configuration as an initial condition. If a disk is gravitationally unstable only locally within a narrow range of radius, due for instance to the concentrated mass addition from the envelop near the centrifugal radius (e.g., Bae *et al.* 2014), the spirals are launched only at the gravitationally unstable region of the disk while they can propagate radially to the gravitationally stable region. In such a case, the pattern speed of the GI-driven spirals is the angular velocity at the excitation radius of the spirals, a picture similar to planet-driven spirals as explained in Section 6.1.

Spirals generated by gravitational instability can trap dust particles (Rice *et al.* 2006; Gibbons *et al.* 2014). Shearing-box simulations including dust particles (Baehr and Zhu 2021a) suggest that dusty spirals have universal opening angles ($\sim 10^\circ$), independent of the computational domain, the cooling time, or the particle size. Particles with $St \sim 1$ drift fastest and thus have the highest concentration in spirals. Particles with $St > 1$ can also be trapped in spirals, but in this case it is the gravity from the gaseous spiral arms that enables trapping, instead of aerodynamic drag. It is thus possible that GI-driven spirals are observed with mm continuum observations (Cossins *et al.* 2010a; Evans *et al.* 2017; Forgan *et al.* 2018; Hall *et al.* 2018).

In addition to continuum observations, molecular line observations can also probe the spirals induced by GI (Hall *et al.* 2020). Forgan *et al.* (2012) suggest that the in-plane velocity broadening can be one order of magnitude higher than the perpendicular velocity broadening. Shi and Chiang (2014) carried out 3-D shearing box simulations and found that turbulent velocities are nearly uniform vertically, increasing by just a factor of 2 from the midplane to the surface. They found a peak at around $0.2\text{--}0.3 c_s$, higher than Forgan *et al.* (2012). These results can be tested by future disk kinematics observations.

To summarize, gravitational instabilities can produce 2 to > 10 spirals, although high-order modes are likely more challenging to observe due to the smaller density perturbations that they produce. The pitch angle of GI-driven spirals

is typically $5 - 15^\circ$. The spirals can be transient and the pattern speed is expected to be close to the local Keplerian speed.

7.2. Influence of Self-gravity on Other Substructure-forming Processes

When the disk is gravitationally stable ($Q > 1$), disk self-gravity is ignored by most theoretical works for several reasons. First, gravitational instability has a sharp turn-on/off at $Q \sim 1$ – gravitational instability does not operate even in a $Q = 2$ disk. Second, Class II protoplanetary disks are thought to be far less massive than a $Q = 1$ disk. Third, it is computationally expensive to include disk self-gravity in simulations. However, even in gravitationally stable disks ($Q > 1$), disk self-gravity can be important for many physical processes, including dust settling, vortex formation, and planet-disk interactions.

In a self-gravitating disk, both the gravity from the gas to the dust and the anisotropic turbulence lead to a more settled dust disk (Baehr and Zhu 2021b). This can potentially explain the thin dusty layer in the moderately accreting HL Tau (Pinte *et al.* 2016). When the interaction between the dust and the gas is taken into account, the dusty disk can also be subject to the secular gravitational instability (Youdin 2011; Takahashi and Inutsuka 2014, 2016; Tominaga *et al.* 2018, 2019), which can generate ring substructures.

Self-gravity can significantly weaken vortices in protoplanetary disks (Lin and Papaloizou 2011). Lovelace and Hohlfeld (2013) suggested that disk self-gravity can suppress the development of RWI modes with mode number $m < (\pi/2)(R/H)Q^{-1}$. Thus, for all mode numbers $m \geq 1$ the vortex formation by the RWI will be significantly affected when $Q < (\pi/2)(H/R)^{-1}$. For a disk with $H/R = 0.1$ as an example, this suggests that even for a disk with $Q \simeq 10$ self-gravity can play a significant role in vortex formation (Zhu and Baruteau 2016).

Finally, the outcome of planet-disk interactions, such as the number and strength of planet-driven spirals and the width and depth of gaps around the planet, can also be affected in $Q > 1$ disks. Zhang and Zhu (2020) found that in disks with $Q \simeq 2$, planets generate stronger and more tightly wound spirals and the gaps are also deeper (see also Pohl *et al.* 2015).

8. Processes Induced by Dust Particles

Until now, we have discussed processes where the grains' spatial distribution passively evolves depending on the dynamics of the gas. However, there are situations where dust plays a dominant role in shaping the continuum emission morphology. We separate such processes into two broad categories: icelines and dust-induced instabilities.

8.1. Icelines

Icelines are the radial locations where volatiles sublimate and condense. Because the sublimation temperature

is material-dependent, different volatile species have icelines at different radial locations. For instance, N_2 , CO , CO_2 , and H_2O have sublimation temperatures of ~ 10 – 20 , 20 – 30 , 60 – 70 , and 130 – 160 K at typical disk densities, respectively (Zhang *et al.* 2015). Because the disk temperature usually decreases with distance from the central star, species that are more volatile have icelines at larger radial distances. Because dust particles drift toward the central star, they inevitably pass through icelines and lose ice.

Around the icelines of major volatiles, the inward flow of icy aggregates can produce dust substructures in three different ways. First, aggregates may break up into fragments when they lose ice. Because small fragments drift slowly, they pile up inside the icelines (Saito and Sirono 2011; Ida and Guillot 2016; Hyodo *et al.* 2019). Second, the vapor released from the aggregates can be transported outward by turbulence and condense onto other aggregates outside the icelines, which can result in a local enhancement in the solid surface density (Ros and Johansen 2013; Schoonenberg and Ormel 2017; Drazkowska and Alibert 2017; Stammer *et al.* 2017; Hyodo *et al.* 2019). Third, the aggregates' stickiness can change as their composition changes at the icelines. This can cause a steep variation of the grain size and dust surface density across the icelines (Birnstiel *et al.* 2010; Banzatti *et al.* 2015; Pinilla *et al.* 2017a; Okuzumi and Tazaki 2019). However, we note that there are currently large uncertainties in the stickiness of silicates and ices. It was previously believed that H_2O ice is stickier than silicates (Dominik and Tielens 1997; Blum and Wurm 2000; Wada *et al.* 2009; Gundlach and Blum 2015), but some recent studies call this into question (Kimura *et al.* 2015; Gundlach *et al.* 2018; Musiolik and Wurm 2019; Steinpilz *et al.* 2019). Other recent experiments show that CO_2 ice is less sticky than H_2O ice (Musiolik *et al.* 2016a,b).

Zhang *et al.* (2015) proposed that annular gaps seen in the HL Tau disk could be related to the icelines of some volatiles. They assumed that icy particles outside the icelines have grown beyond millimeter sizes through ice recondensation. Such particles have smaller millimeter opacities and therefore produce less thermal emission per mass than those smaller than millimeters. Zhang *et al.* (2015) explained the dips seen in the dust continuum images of the HL Tau disk as a result of the millimeter optical depth reduction due to ice condensation growth. However, ice recondensation can cause an increase in the solid surface density, and therefore whether or not ice condensation growth results in a reduction of millimeter dust emission has to be further tested.

Outside icelines, icy aggregates may also experience another important mechanical process: sintering. This is a phenomenon where the grains inside an aggregate fuse together, at temperatures slightly below the sublimation and melting temperatures of constituting materials. An important consequence of sintering is that it makes aggregates harder but less sticky (Sirono 2011; Sirono and Ueno 2017). Combined with the size-dependent radial drift, sintering can also result in an enhancement of the dust surface density

outside of the icelines (Okuzumi *et al.* 2016). Unlike the three iceline-related substructure formation processes described above, sintering-induced dust ring formation may occur at the icelines of moderately abundant volatiles such as NH_3 and CH_4 , in addition to the icelines of more abundant H_2O , CO_2 , and CO (Sirono and Ueno 2017).

Okuzumi *et al.* (2016) proposed that the prominent dust rings in the HL Tau disk can be explained by aggregate sintering outside of major icelines. According to their scenario, the icelines define the rings' inner edges, whereas the sintering timescale determines the rings' radial extent. The ring widths can be either larger or smaller than the gas scale height, depending on the size of grains that constitute the aggregates. Okuzumi *et al.* (2016) list several volatiles (including H_2O , NH_3 , CO_2 , CH_4 , and CO) whose abundance may be high enough to induce aggregate sintering. The number of dust rings predicted from this scenario can be smaller than the number of the major volatiles because some rings can overlap.

The iceline scenarios do not require gas ring/gap substructures to produce dust ring/gap substructures. However, this does not mean that the gas surface density must be radially smooth across icelines. For example, Hu *et al.* (2019) show that sintering-induced dust rings at icelines, when combined with non-ideal MHD effects, can produce gas rings at the same locations. Specifically, the most prominent ring at the CO_2 iceline shows a gas surface density contrast of 17% compared to the expected smooth disk profile. This occurs because a large amount of dust in the dust rings leads to a lower ionization level (Sano *et al.* 2000; Wardle 2007; Okuzumi 2009; Hu *et al.* 2021) that results in slower disk gas accretion.

The most important prediction from the iceline scenarios is that the locations of the iceline-induced substructures should be determined by the disk radial temperature profile. This prediction has been widely used to observationally test the scenarios (Long *et al.* 2018; Huang *et al.* 2018b; van der Marel *et al.* 2019). The current observational data show no clear correlation between the locations of the observed rings and the expected locations of the icelines of major volatile species. This can be seen in Figure 3(e), where we compare the radial locations of observed rings with the expected locations of some of the major icelines (N_2 , CO , CO_2 , and H_2O). Moreover, the radius ratios of substructure pairs do not show clustering at particular values (not shown in Figure 3 but see Huang *et al.* 2018b; van der Marel *et al.* 2019), which would be expected if the substructures are of iceline origin and if the disk radial temperature profile obeys a power law. Existing continuum observations thus disfavor iceline scenarios as the universal explanation for the observed ring/gap substructures. Yet, the latest high-resolution observations of dust continuum and CO emission lines from the Molecules with ALMA on Planet-forming Scales (MAPS) ALMA Large Program show that two of five observed disks (HD 163296 and MWC 480) have bright dust rings at the midplane CO iceline (Zhang *et al.* 2021).

Caution is needed in testing iceline scenarios using a

simple disk temperature model. *Owen (2020)* shows that icelines can be thermally unstable and suggests that a simple (steady and power-law) temperature profile may not be applicable to inferring iceline locations. Even without dust rings, centrally irradiated disks can be thermally unstable (*Dullemond 2000; Watanabe and Lin 2008; Wu and Lithwick 2021*) and icelines may migrate back and forth (*Ueda et al. 2021; Okuzumi et al. 2022*). Accretion outbursts may also affect iceline positions (*Martin and Livio 2012*).

8.2. Dust-induced Instabilities

The streaming instability can produce dust substructures in disks (*Youdin and Goodman 2005; Johansen and Youdin 2007*). As explained in Section 3.2, dust grains in a gas disk with a negative radial pressure gradient experience headwinds. When dust overdensities are present, the back-reaction from grains on the gas causes the gas to orbit faster than otherwise, weakening the headwind on the grains. The weaker headwind reduces the radial drift of grains, further enhancing the concentration of grains. Numerical simulations show that when the streaming instability is saturated, the resulting grain rings have a width that ranges from a fraction up to 10 percent of the gas scale height and the spacing between the rings is 10 to 20 percent of the gas scale height (*Yang and Johansen 2014; Yang et al. 2017; Li et al. 2018a; Carrera et al. 2021*).

When the concentration of grains becomes sufficiently large (dust-to-gas mass ratio ~ 1), the gas dynamics can be dominated by the grains. Under such circumstances, the drag from the grains on the gas can overcome the viscous diffusion of the gas, creating a local gas pressure maxima (*Gonzalez et al. 2017*). When the gas accretion is governed by magnetic processes, inhomogeneous grain distributions can result in spatial variations in the degree of coupling between the gas and the magnetic field, by changing the disk ionization structure (*Hu et al. 2019*) or the conductivity of the gas (*Dullemond and Penzlin 2018*) across the over-/under-dense regions. This, in turn, leads to a non-uniform accretion of the gas, creating local gas pressure maxima within which grains can be efficiently trapped.

Because the rate of collisional grain growth scales with the grain surface density, grains grow faster (slower) in a positive (negative) grain surface density perturbation. The resultant radial variation of the grain size yields a radial variation of the grains' radial drift velocity, which in turn alters the radial surface density variation. *Tominaga et al. (2021)* showed that this feedback can be positive and produce dust rings and gaps.

The dust concentration within a vortex can feedback to the gas and weaken the vortex. Both analytical and numerical works (*Fu et al. 2014a; Raiton and Papaloizou 2014*) suggest that a dust-loaded vortex can be subject to instabilities, especially at the vortex center. However, these instabilities may not be able to destroy the vortex. The dust feedback can be even more complicated if multiple dust species can feedback to the vortex (*Crnkovic-Rubsamen*

et al. 2015), potentially leading to anti-correlations between small and large dust grains within vortices. Such instability studies involving multiple dust species just start to emerge (*Krapp et al. 2018; Paardekooper et al. 2020; Yang and Zhu 2021*). They can potentially lead to interesting observational effects, which deserve future studies.

9. Connecting Observed Substructures with Physical Processes

Now that we have summarized observed disk substructure properties and introduced various potential substructure-forming processes, in this Section, we aim to connect the observations and the theory. We highlight the successes and challenges of the physical processes in explaining rings and gaps (Section 9.1), spirals (Section 9.2), and crescents (Section 9.3). In each subsection, we start by discussing companions as the potential substructure-forming mechanism because it is the only mechanism for which we have clear observational evidence (e.g., cavity in PDS 70, spirals in AS 205; see Figure 2 and subsections below). We then discuss what advantages and disadvantages other substructure-forming processes have in comparison to the companion scenario. As we discuss each mechanism, we also highlight future research directions (both theoretical and observational) that can help to distinguish between the different origins. We summarize suggested future observations in Table 4.

9.1. Rings and Gaps

The most immediate observables of annular substructures are the number of rings/gaps, their radial location, and their radial width. These properties of observed rings and gaps are summarized in Section 2.3.1, Figure 3, and Table 1. From the observations carried out so far, we do not find a concentration of rings around certain radial locations or correlations between ring properties and stellar/disk properties (Figure 3). Before we further discuss what the absence of patterns or correlations may indicate regarding the origin of annular substructures, it is worth pointing out that ring properties are inferred mostly from (sub-)millimeter continuum observations and thus caution is needed when interpreting the observations, in particular for the radial width. Large grains probed by continuum observations are likely subject to strong aerodynamic drag, the degree of which depends on the Stokes number of the grains (Section 3). For a given grain size, the Stokes number can vary significantly depending on the column density of the protoplanetary disk. This means that one shall not directly compare the width of dust rings located at different radii within the same disk or the width of dust rings found in different disks. Instead, for a proper comparison, we have to convert the observed width of dust rings to the width in the underlying gas distribution in order to remove the dependency on differing Stokes numbers. Of course, this is not a straightforward task. As described by Equation (3), the Stokes number is a function of grain's internal density and the gas column

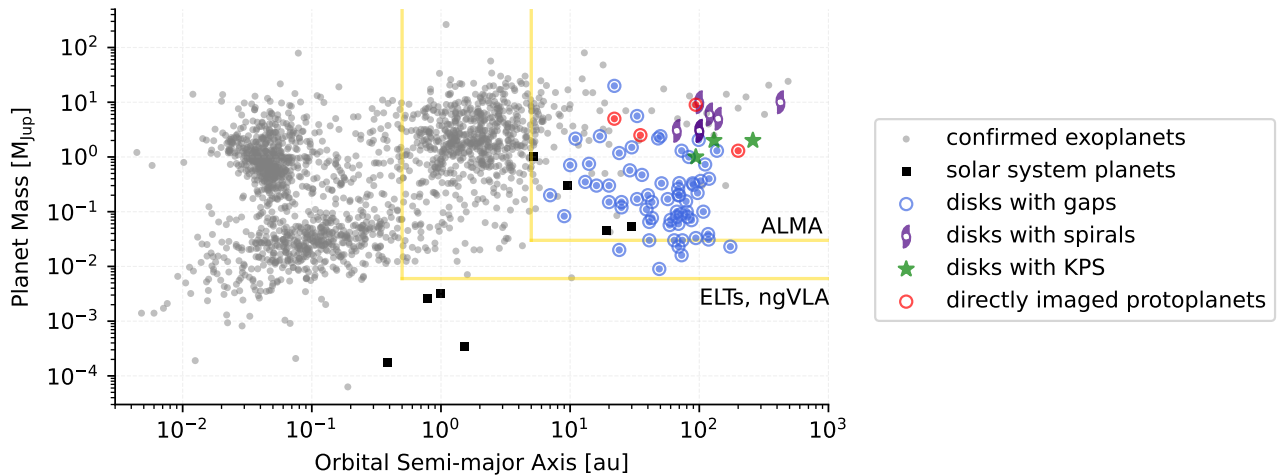


Fig. 7.— The distribution of the mass and orbital semi-major axis of (grey circles) confirmed exoplanets, (black squares) solar system planets, and (color symbols) protoplanets proposed to reproduce the observed disk substructures (blue \odot for annular substructures, purple spiral symbols for spirals, and green stars for kinematic planetary signatures). Directly imaged protoplanets (PDS 70b/c, AB Aur b, AS 209b) are shown with red \odot symbols. Uncertainties in the estimated planet mass are not presented in this figure, though it is typically a factor of a few to ten, which are mainly arising from the ill-constrained disk properties including the disk viscosity. The yellow lines show illustrative regions where current and future observing facilities are expected to find protoplanets directly or through disk substructures they create. Data used in this plot and references are available at <http://ppvii.org/chapter/12/>.

density of the disk both of which are, needless to say, difficult to constrain. The fact that most ring properties are constrained by continuum observations is a great challenge when it comes to comparing observations with simulations, too, because most (but not all) theoretical predictions come from gas-only simulations. Given these difficulties, it may thus be too early to conclude that correlations between ring properties and stellar/disk properties are lacking. In the future, directly constraining the radial width of gas rings from the radial variations in the rotational velocity profile (e.g., [Teague et al. 2018a](#)) and from the observations of optically thin gas tracers (e.g., [Facchini et al. 2020](#)) for a large disk sample would help to perform a more proper statistical analysis.

Among the physical processes capable of creating rings and gaps, the companion scenario is most flexible in explaining the broad range of ring/gap properties. This flexibility is due in part to ill-constrained disk viscosity and temperature (see e.g., Equation 10), but nevertheless one can almost always adjust the companion mass and orbital radius to reproduce the observations. In fact, there has been a lot of effort from the community to explain observed rings and gaps using planets. Figure 7 shows the population of such hypothesized planets that are proposed to reproduce the observed disk substructures using either hydrodynamic planet-disk interaction simulations or scaling relations between the planet mass, disk properties, and gap width/depth. This figure suggests that the observed annular substructures could have been created by a population of planets with masses between about 0.1–10 Jupiter masses

and orbital radii of about 10–500 au.

However, challenges do exist for the planet scenario. Part of the complication arises from the possibility that a single planet can open multiple gaps, some (or all) of which do not have a planet within them ([Bae et al. 2017](#); [Dong et al. 2017](#); [Wafflard-Fernandez and Baruteau 2020](#), see also Section 6.1.2). This suggests that, even in the case that all of the observed rings and gaps are created by planets, some of the hypothesized planet population presented in Figure 7 can be false positives. After all, we need more direct evidence of planets in order to unambiguously connect companions to annular substructures. The best ways include searching for thermal emission in the near and mid-infrared where planets are the brightest, line emission from accreting gas (e.g. $H\alpha$), and emission from circumplanetary disks (CPDs). Encouragingly, there are a small, yet increasing number of young planets directly detected. PDS 70b and c are detected in near-infrared imaging and $H\alpha$ observations ([Keppler et al. 2018](#); [Wagner et al. 2018](#); [Haffert et al. 2019](#); [Mesa et al. 2019](#), see also [Benisty et al.](#) in this book), and a CPD is detected in sub-mm around PDS 70c ([Isella et al. 2019](#); [Benisty et al. 2021](#)). More recently, AB Aur b is detected in near-infrared imaging ([Currie et al. 2022](#)) and AS 209b is detected through its CPD emission in ^{13}CO ([Bae et al. 2022](#)). The detection of these planets has proven that direct detection of young, forming planets is possible with existing facilities. Furthermore, these observations provide direct evidence that companions can indeed create substructures: a cavity created by PDS 70b and c, spirals excited by AB Aur b, and a gap and velocity kinks (see Section 9.2)

produced by AS 209b. In the very near future, the James Webb Space Telescope (JWST) should provide the capability to detect young, forming planets predicted via ALMA observations. Indeed, at the time of writing this Chapter, there are accepted JWST programs which specifically aim to search for planets responsible for the substructures previously observed with ALMA and ground-based telescopes. In the further future, 30-m class ground based telescopes and the next generation Very Large Array (ngVLA) will be key in the search for planets around young stars.

Icelines are another popular scenario proposed to explain rings and gaps. Icelines must exist since temperature changes across the disk are unavoidable and the phase transition of volatiles should occur at appropriate locations. Until now, a common practice to test the iceline scenario is to infer the disk temperature, from either simplified approximations of the midplane temperature using the stellar luminosity (Figure 3e; see also e.g., [Huang et al. 2018b](#)) or disk specific radiative transfer modeling ([van der Marel et al. 2019](#)), and compare the predicted condensation front locations with observed ring/gap locations. Most previous attempts did not find a strong correlation between the position of the observed rings/gaps and the expected location of ice-lines, although it is worth noting that some of the observed continuum rings in the disks around HL Tau ([Zhang et al. 2015](#); [Okuzumi et al. 2016](#)), MWC 480, and HD 163296 ([Zhang et al. 2021](#)) lie close to the expected positions of midplane icelines. Another indirect way to test the iceline scenario is to map the gas density and pressure profiles across rings and gaps. Unlike most other annular substructure-forming mechanisms which generate pressure bumps that trap grains, pressure bumps are not a prerequisite for rings formed by icelines. Therefore, if we find a case where the grain size changes across a continuum ring/gap but there is no associated gas pressure maximum/minimum at the ring/gap location, icelines would offer a compelling explanation. So far, the capability of measuring the gas density profile has been limited by the sensitivity and angular resolution of optically thin gas tracers, but some progress has been made. As an example, five disks with continuum rings/gaps have been recently targeted by the ALMA large program MAPS ([Öberg et al. 2021](#)). [Zhang et al. \(2021\)](#) found that dust gaps are coincident with gas gaps in some of the disks, as expected in the case of radial migration of grains due to gas pressure gradients, whereas depletion of the gas is minimal or lacking within some of the dust gaps in IM Lup, GM Aur, and MWC 480. A more direct way to test the iceline scenario would be to measure the disk midplane temperature at the location of the rings and gaps directly from the observations and compare it with the condensation temperature of volatiles. So far, such a direct measurement has been applied only to the outer disk (> 50 au) of HD 163296 ([Dullemond et al. 2020](#)), where it is found that the temperature is nearly constant around 20K across a region characterized by the three dust rings in the disk. This temperature is roughly consistent with the condensation temperature of CO. Clearly, ALMA observations

of a larger disk sample at both higher angular resolution and sensitivity are required to understand the role that icelines play in the formation of dust rings and gaps.

While the companion and iceline scenario offers predictions that can be tested with observations, most of the discussed (magneto-)hydrodynamic processes either have somewhat similar predictions in terms of the gas distribution and kinematics, or are difficult to observationally test. For example, numerical simulations showed that both VSI and MHD zonal flows tend to produce multiple sets of rings and gaps with typical radial length scales of order of a gas scale height. For VSI and magnetically-driven zonal flows, it is expected that they induce corrugated vertical flows with velocities as high as $10\text{-}100\text{ m s}^{-1}$ on spatial scales comparable to the disk pressure scale height ([Barraza-Alfaro et al. 2021](#); [Hu et al. 2022](#)). If such flows can be identified and their radial locations coincide with continuum rings and gaps, this can support VSI or zonal flows as the origin of the annular substructures. For magnetically-driven zonal flows, the detection of magnetic fields and the variation of the magnetic field strengths across observed annular substructures at sufficiently high spatial resolution might support the link between zonal flows and annular substructures. However, measurements of the magnetic field morphology and strength in disk are extremely difficult. In particular, constraining the field morphology via mapping of the dust continuum polarization is hampered by dust scattering (see, e.g., [Kataoka et al. 2015](#)) and the direct measurement of the field strength via observations of Zeeman splitting of molecular lines require a sensitivity not yet achieved by ALMA observations ([Harrison et al. 2021](#)). Despite these difficulties, a detailed study of the gas kinematics would undoubtedly provide important information on the origin of rings and gaps, and, in general, on the processes that control the evolution of circumstellar disks. So far, ALMA observations have either focused on mapping the dust continuum emission at very high angular resolution or mapping the gas kinematics at high velocity resolution ($50\text{-}100\text{ m s}^{-1}$) but on insufficient angular scales ($> 0.1''$). Mapping line emission at both high angular and high velocity resolution with ALMA is thus highly desired.

We would like to conclude our discussion of rings and gaps by mentioning two other physical processes, photoevaporative/MHD winds and streaming instability. Proving winds as a viable mechanism for gap (or cavity) formation requires spatial information as to where the winds originate from, which is challenging. Nevertheless, recent high resolution spectroscopic observations of molecular vibrational lines in infrared wavelengths showed some promising results. [Banzatti et al. \(2022\)](#) reported that spectra of CO vibrational lines in a fraction of their target disks have a combination of double-peak and triangular line shapes that can be interpreted as emission from a Keplerian disk plus disk winds. Based on their analysis, the CO emission in some disks, including transition disks SR 21 and IRS 48, appears to arise from a wind originating within the dust cavity observed in the mm. Although this does not prove that dust

cavities are created by winds, it at least demonstrates that winds might be effective in removing gas within 1-10 au from the central star.

Although streaming instability may operate at very small scales, the structures it produces may merge over time and potentially be observable. Considering the large amount of numerical resource it needed to capture both the instability and the large scale structure over a long period of time, the largest 3-D simulations so far only cover the disk region within 1-2 disk scale heights (*Yang and Johansen 2014; Li et al. 2018b*). However, these simulations already reveal some axisymmetric ring formation at the radial scale of a fraction of the disk scale height. With bigger simulation boxes and longer simulation duration, these structures may be more prominent, which deserves future studies. Since dust-induced instabilities, including the streaming instability, generally require high dust-to-gas mass ratio close to unity, measuring spatially-resolved gas and dust column density would be helpful to assess whether the disk is in a condition that can trigger dust-induced instabilities. Searching for clumps along continuum rings on scales comparable to or smaller than the gas scale height will be also helpful to infer whether streaming instability is in the act.

9.2. Spirals

The most immediate observables of spirals are the number of spirals, their radial location/extent, and their pitch angle. These properties of observed spirals are summarized in Section 2.3.2, Figure 4, and Table 2. In addition to these properties, the pattern speed of spirals can be inferred via long-term monitoring observations, which can put meaningful constraints on the origin of the spirals as we will discuss below. As we pointed out in Section 2.3.2, the occurrence rate of spirals is significantly lower than that of annular substructures. In particular, a relatively large fraction of disks observed at high effective angular resolution of $\theta_D/\theta_{res} > 3$ does not have spirals (Figure 4 (b)), suggesting that the low spiral occurrence is unlikely due to insufficient angular resolution. Instead, it may well be that spirals are intrinsically rarer than annular substructures in protoplanetary disks. Alternatively, the low spiral occurrence could be associated with poor coupling of grains within spirals. When the pattern speed of a spiral Ω_p and the background Keplerian speed Ω_K differ, only small particles with a stopping time shorter than the spiral crossing time can be trapped by the spiral (Section 3.2). Indeed, recent multi-fluid (gas + dust) planet-disk interaction simulations showed that grains with Stokes number of $\gtrsim 0.1$ are poorly coupled to planet-driven spirals (*Sturm et al. 2020; Speedie et al. 2022*). Along this line, it is interesting to note that spirals are preferentially detected in NIR observations (16 out of 22 disks with observed spirals) than in mm continuum observations (7 out of 22 disks with observed spirals; see Table 2). A direct test could be done if we measure the pattern speed of spirals through long-term monitoring observations, which can tell us whether or not the spirals orbit

at the local Keplerian frequency. Spirals driven by companions, RWI-driven vortices, or eccentric modes are expected to orbit at faster or slower speed than the local Keplerian speed, whereas spirals driven by GI or MRI are expected to orbit at the local Keplerian frequency.

As in the case of annular substructures, tidal interaction with companions is the only mechanism so far that has firm evidence for producing spirals. The discovery of spirals in wide-separation binary systems AS 205N/S, HT LupA/B (*Kurtovic et al. 2018*), HD 100453A/B (*Wagner et al. 2015*), and UX TauA/C (*Ménard et al. 2020; Zapata et al. 2020*) offer strong evidence that companions can indeed excite observable spirals. In all three systems two-armed spirals are observed in the disk around the primary star. This is consistent with the prediction that the number of spirals driven by a companion would decrease with growing companion mass, eventually converging to two inward of the companion's orbit when the mass ratio is greater than a few $\times 10^{-3}$ (*Bae and Zhu 2018b*), equivalent to a few Jupiter masses around a solar-mass star. It is worth pointing out that for AS 205N and HT LupA, spirals are detected in continuum observations with very low arm-to-trough contrast (no spirals are detected in continuum for UX TauA/C). The low contrast supports the idea that mm grains are poorly coupled to the companion-induced spirals due to the differential rotation between the spirals and the background disk gas. In summary, all of these pieces of information are consistent with the theoretical predictions for companion-driven spirals. However, whether or not these binary systems are gravitationally bound is not entirely clear at this point (*Salyk et al. 2014; Kurtovic et al. 2018; Zapata et al. 2020*). Future long-term monitoring observations that can characterize the orbital motion of the binary systems would enable us to determine whether these systems are gravitationally bound or they are currently experiencing flyby events.

For given underlying disk properties, spirals become weaker and more tightly wound with decreasing companion mass. This means that detecting spirals driven by planetary companions is generally more challenging than detecting spirals driven by stellar companions. As we mentioned earlier, the number of spirals a companion creates increases with decreasing companion mass and two-armed spirals are expected for multi-Jovian mass planets (*Bae and Zhu 2018b*). As a result, hydrodynamic simulations often require a few to 10 Jupiter-mass planets to reproduce observed two-armed spirals (Figure 7). One may ask why such large-mass planets at large orbital separation have not yet been detected since current high-contrast direct imaging observations offer sufficient sensitivity in most optimistic cases (e.g., *Zurlo et al. 2020; Asensio-Torres et al. 2021*, see also *Benisty et al.* in this Book). There are a few possible explanations to this, which are not exclusive to each other. *First*, the predicted planet masses from hydrodynamic simulations could be larger than the actual planet masses. Most previous numerical simulations of protoplanetary disks (not just for planet-disk interaction simulations,

but in general) adopted a vertically isothermal temperature structure whereas in reality, disks have stratified vertical temperature structures such that the disk surface is hotter than the disk midplane in the regions of our interest (i.e., $\gtrsim 10$ au; [Law et al. 2021](#)). Because planet-driven spirals form via superposition of *acoustic/shock* waves (Section 6.1.1), their propagation (and thus their morphology) is dependent on the underlying temperature structure. [Juhász and Rosotti \(2018\)](#) showed that, for a given planet mass, the spirals launched by the planet are more opened in the surface layers when vertical temperature stratification is considered. It is thus possible that the current predictions based on the spiral morphology could overestimate the required planet masses due to the use of a vertically isothermal temperature structure. *Second*, the predicted flux of the planets could be overestimated. The two most widely-used direct imaging approaches are searching for infrared thermal emission and accretion tracers (e.g., H α line emission) from young planets. For high-contrast optical/infrared imaging, the most crucial factor that determines the observability of the planet is the luminosity of the planet. The present-day luminosity of the planet is determined by the combination of the initial luminosity and the cooling rate. Depending on the formation pathway and detailed post-formation evolution, the present-day luminosity can vary by orders of magnitude (e.g., [Marley et al. 2007](#); [Spiegel and Burrows 2012](#); [Mordasini et al. 2017](#)). Current observing facilities can detect *hot-start* planets, but they are unable to detect *cold-start* planets (e.g., [Asensio-Torres et al. 2021](#)). For accretion tracers, the instantaneous accretion rate at the time of observations is crucial in determining the observability ([Zhu et al. 2015a](#); [Szulágyi et al. 2019](#); [Szulágyi and Ercolano 2020](#)), so whether young planets have completed gas accretion and whether planets' accretion is steady or episodic would be the question. *Lastly*, even if model predictions are accurate, we could still suffer from the extinction by circumplanetary and/or circumstellar disk materials along the line-of-sight to the planets (e.g., [Sanchis et al. 2020](#)).

As mentioned in Section 9.1, JWST observations in the mid-infrared wavelengths can offer a promising way to find young planets associated with the observed spirals. Alternatively, it has been demonstrated that velocity perturbations created by planet-driven spirals, so-called velocity kinks, can be observed with molecular line observations using ALMA ([Pinte et al. 2018](#); [Teague et al. 2018a](#); [Casassus and Pérez 2019](#); see also [Pinte et al.](#) in this book). One advantage of using kinematic substructure is that the strongest velocity perturbations arising in the immediate vicinity of the planet. It can thus help not only to infer the presence of embedded planets, but also to localize them. This property can be very powerful when kinematic substructures are found along with other morphological substructures. In the case of HD 97048, velocity perturbations in CO emission are found within the continuum gap which offer promising evidence of the presence of a planet in the disk ([Pinte et al. 2019](#)). In the case of AS 209, velocity perturbations are seen with an optically thick ^{12}CO line, which coincide

with a CPD seen with an optically thin ^{13}CO line ([Bae et al. 2022](#)).

Besides the companion scenario, gravitational instability is another popular scenario that is often proposed to explain observed spirals. Numerical simulations predicted that GI operating in more massive disks generate fewer, more opened spirals. However, we find no clear trend that the number of spiral arms decreases with the disk mass or the pitch angle of spiral arms increases with the disk mass. Figure 4 (e) actually suggests smaller pitch angles in more massive disks. This was first noted by [Yu et al. \(2019\)](#). [Chen et al. \(2021\)](#) explained this trend with the linear normal mode analysis showing that the spiral's pitch angle should be proportional to c_s^2/M_d . It will be important to confirm the linear normal mode analysis using direct numerical simulations in future. For a small number of objects, detailed comparisons between GI simulations and observations have been carried out. The most promising case for the GI induced spirals is Elias 2-27 ([Hall et al. 2018](#); [Forgan et al. 2018](#); [Paneque-Carreño et al. 2021](#)). For MWC 758 and SAO 206462, [Dong et al. \(2015\)](#) successfully reproduce the contrast of the observed spirals at near-IR (a factor of ~ 3) and the pitch angle (10° - 15°) using self-gravitating disks. These numerical simulations commonly suggest that the disk needs to be very massive with $M_d/M_* \gtrsim 0.25$ in order to explain the observed spiral morphology with GI. A direct observational test would thus be to measure the disk mass. When spatially-resolved gas surface density and gas temperature can be measured, we can also compute the Toomre Q parameter to check whether and at which radii the disk is gravitationally unstable.

From the data we collected, we found that there is a potentially strong link between the presence spirals and crescents in disks. Out of 12 disks with mm crescents, 9 disks turned out to have spirals (see Tables 2 and 3). One possible explanation to this potential link is that vortices have excited the spirals. In this scenario, spirals should be connected to crescents, and the two orbit the central star at the same frequency. It will be worth studying the connection between vortices and spirals for the 9 disks. Another possibility is that one physical process has created both crescents and spirals. The companion scenario is one such process, generating crescents via the RWI while exciting spirals via Lindblad resonances. In this case, vortices and spirals are not necessarily connected to each other, and they can orbit the central star at different frequencies.

Some recent NIR and (sub-)mm molecular line observations discovered asymmetric and extended streamer around some young disks ([Yen et al. 2019](#); [Alves et al. 2020](#); [Pineda et al. 2020](#); [Ginski et al. 2021](#); [Garufi et al. 2021](#)). When the specific angular momentum of infalling materials is sufficiently different from that of the disk, infalling materials can create spirals ([Lesur et al. 2015](#); [Kuffmeier et al. 2017, 2018](#); [Kuznetsova et al. 2022](#)). Detecting spirals in the disks having large-scale streamers (and vice versa) can support the idea of infall creating spirals. In addition, because spirals are excited at the location where infalling mass lands on

the disk, it will be helpful to identify the location of mass landing using shock tracers, such as SO and SO₂.

Because sound waves in differentially rotating disks propagate in the form of spirals, any perturbation in protoplanetary disks can naturally produce spirals. This also applies to turbulence driven by the hydrodynamic/MHD instabilities. In case of the MRI, direct detection of magnetic fields in the disk via continuum and/or line polarization observations would support the MRI being the origin of observed spirals.

Spirals driven by eccentric modes in marginally gravitationally unstable disks have perhaps the most distinct properties, since they are not propagating but trapped waves. Eccentric modes produce a single spiral that has a very small pitch angle of $\lesssim 5^\circ$. Also, the spiral orbits around the star at a much slower orbital frequency than the Keplerian frequency. Given that the majority of disks in our sample has more than one spiral, eccentric modes are less likely to be the dominating spiral-forming mechanism for the sample.

9.3. Crescents

The most immediate observables of crescents are the number of crescents, their radial location, radial/azimuthal extent, and azimuthal intensity contrast. These properties of observed crescents are summarized in Section 2.3.3, Figure 5, and Table 3.

While rings and spirals have many possible origins, there are only two leading mechanisms for crescents: vortices and lumps. In general, hydrodynamic instabilities (RWI, VSI, COS, and ZVI) create vortices which can trap particles therein. Lumps can form in eccentric disks as particles spend longer time near the apocenter than the pericenter. L4 and L5 Lagrangian points within the horseshoe region of a companion is another example of lumps. When vortices and lumps are compared, lumps have significantly less rotating motion around the lump center than vortices (Ragusa *et al.* 2017). Thus, if strong rotating gas motions around the core of a crescent can be identified via molecular line observations, it will be strong evidence that vortices driven by hydrodynamic instabilities could be the origin of the crescent. Boehler *et al.* (2021) presented a tentative evidence that the kinematics of the disk gas around the crescent in the HD 142527 disk is consistent with the presence of a large vortex around the dust crescent, although they cautioned that the beam smearing effect may instead create a similar kinematic pattern. Future high angular/velocity resolution observations will help distinguish vortices and lumps.

Among all 13 disks that we compiled, there is no case where multiple crescents are observed at the same radial location within a single annular structure. Because hydrodynamics instabilities generally form multiple vortices within a single ring, which subsequently merge with each other (see Section 4), the fact that we do not see multiple crescents at the same radial location in a single disk may imply that (albeit a small number statistics) the vortex merging timescale could be relatively short.

Unlike annular substructures or spirals, crescents do not have a case where a clear connection with a companion is confirmed. The continuum ring beyond the orbit of PDS 70b and c has an asymmetry in the intensity, but the azimuthal intensity contrast is only moderate and it is unclear at this point whether the asymmetry is associated with a vortex, potentially driven by the RWI. In addition to crescents that can form in the gap edge via the RWI, companions can create crescents within the horseshoe region, in L4 and L5 Lagrangian points. L4 and L5 are 60° ahead of and behind the companion, so dust concentrations that are $\simeq 120^\circ$ apart at the same radial distance to the central star may be an indication of dust trapping within Lagrangian points. Long *et al.* (2022) recently presented a promising evidence that dust could be trapped around Lagrangian points of yet-unseen planet embedded in the LkCa 15 disk.

While COS and ZVI are known to be able to create vortices, they are unlikely to be the cause of the crescents observed so far because they are expected to operate in the very inner part of protoplanetary disks (Section 4.3 and 4.4). In the future, ngVLA will offer the capability to probe the inner few AU regions where COS and ZVI are expected to operate.

We conclude by discussing some tentative connections between the crescent observations (Figure 5) and theory. First, most observed vortices have aspect ratios between 2 and 5. Theoretical works suggest that only the vortices with the aspect ratio between 4 and 6 can survive the elliptical instability in unstratified disks (Lesur and Papaloizou 2010). In this regard, the small aspect ratio of observed crescents (Figure 5 (a)) seem to be in tension with vortices being the origin, although we note that many of the crescents are poorly resolved in the radial direction, and future high angular resolution observations are required to obtain more accurate aspect ratio. It is also worth pointing out that crescents are observed in continuum observations and the aspect ratio in the gas could be different from what is measured with continuum. Second, although the origin of these crescents is still unknown, some crescents are discovered in the circumbinary disks. Considering that the theory predicts that lumps in circumbinary disks are different from vortices in several ways, we can search for these differences in observations to understand the nature of these crescents. Our current statistics suggests that crescents in circumbinary disks are normally further away from the star (Figure 5 (a)), and they are also wider (with respect to the local scale height, Figure 5 (c)). Third, the submm intensity contrast between the vortex center and the background disk can be much larger than 10 (Figure 5 (b)), suggesting that particle trapping is likely occurring in these crescents. Finally, the crescents seem to have larger aspect ratios in more massive disks (Figure 5 (e)). Considering that a larger aspect ratio corresponds to a weaker vortex, this seems to agree with the theory that disk self-gravity weakens the vortex.

10. Implications to Protoplanetary Disk and Planet Formation Theory

One of the reasons disk substructures have drawn much attention from the community is because of the possibility that planets could have created them. As discussed in Section 6, the gravitational interactions with planetary mass companions can create rings, gaps, spirals, and crescents. If the observed substructures are caused by forming planets, then there must be a large number of planets with $\sim 0.1 - 10$ Jupiter masses at orbital distances of $10 - 500$ au from their host star (Figure 7). While there is little evidence for a counterpart planet population around older, main-sequence stars, note that most of the current exoplanet detection methods are unable to find this planet population due to the short time baseline and/or insufficient sensitivity. If the lack of mature planets at large orbital distance is real, orbital migration through planet-disk interactions may be one possibility to reconcile the potential difference in protoplanet and mature planet populations (Lodato et al. 2019). However, even in that case, the question remains as to how to form giant planets at large orbital radii. In the core accretion theory, the timescale to build a planet scales roughly as a^2 (Pollack et al. 1996), so building Jovian-mass planets via core accretion is challenging. Gravitational instability offers an alternative (Boss 1997), but planets formed via GI tends to either grow far beyond Jupiter mass (but see Deng et al. 2021) or subject to rapid inward migration, so the formation of planets at large orbital radii is still an open question.

If most of the observed substructures turned out to be created by other mechanisms than planet-disk interaction, this implies that the building blocks of planets are confined in narrow regions and that the planet-forming environment could be very different from what have been assumed in planet formation models. Indeed, planetesimal and planet formation models have started to take non-smooth density distribution into account (see e.g., Carrera et al. 2021 for planetesimal formation by the streaming instability in pressure bumps and Chambers 2021 for rapid formation of Jupiter and wide-orbit exoplanets in disks with pressure bumps). Although it is still unclear how early disk substructures form, there has been an emerging picture that they could form well before the Class II phase (e.g., Segura-Cox et al. 2020), corresponding to stellar ages younger than about 1 Myr. If substructures form so early during protostellar phases, it is possible that they might be related through infall and/or (magneto-)hydrodynamic/gravitational instabilities. It is then reasonable to envision a scenario in which a first generation of planets might form with the help of substructures formed via non-planetary origins, while a second generation of planets may form from the pressure bumps created by the first generation of planets.

Regardless of the formation mechanism, the ubiquity of dust rings confined within pressure maxima has demonstrated that the long-standing radial drift problem can be solved, or at least mitigated. Based on the analysis of

DSHARP data, Dullemond et al. (2018) reported that the brightest rings in AS 209, Elias 2-24, HD 163296, GW Lup and HD 143006 contain a substantial amount of dust, between a few to about 200 Earth masses of solid material. Because ALMA observations are insensitive to solids larger than a few centimeters and protoplanetary disks can be optically thick even in mm wavelengths (Sierra et al. 2019; Zhu et al. 2019), these estimates are probably lower limits for the total amount of solids in these regions. Because large dust grains and pebbles are thought to play a key role in the assembly of planets via the pebble accretion process (see Drazkowska et al. in this book), disk regions where these dust particles are enhanced relative to the gas are preferred places for the formation of rocky and perhaps giant planets. Furthermore, dust rings have been observed on a very wide range of distances from the central star, perhaps suggesting that formation of planets via core accretion might happen much further away from the central star than previously thought. Of course, as we pointed out in Section 2.2, whether substructures are similarly common in fainter disks around lower-mass stars is yet to be confirmed.

For the streaming instability and pebble accretion to form planets or cores of giant planets within the typical protoplanetary disk lifetime, a sufficient amount of materials should exist but also a low level of turbulence is required so that the dust density near the midplane remains sufficiently high. Edge-on disks and inclined protoplanetary disks with annular substructures offer a great opportunity to infer the level of turbulence, as the vertical thickness of the dust disk can be measured (see, e.g., Isella et al. 2016; Pinte et al. 2016; Villenave et al. 2020). These works indicate that millimeter-size grains are confined within a vertical region whose extent is less than about 10% of the vertical extent of small grains and gas. As discussed in Section 3, these results suggest that disks may generally have a relatively low turbulence level, characterized by $\alpha \lesssim 10^{-3}$. In agreement with the level of turbulence inferred from the millimeter continuum observations, it is worth noting that a low level of turbulence in a small sample of protoplanetary disks was derived from measurements of non-thermal broadening of molecular lines (Flaherty et al. 2017, 2018, 2020; Teague et al. 2018c). In conclusion, the low level of turbulence and the substantial mass confined within observed ringed substructures suggest that, if the disks with annular substructure have not yet formed any planets, these disks might be places of ongoing/future planet formation.

11. Conclusion

The prevalence of substructures in protoplanetary disks indicates that their formation likely does not require fine-tuned conditions, at least in the disk population observed so far. On the other hand, the diversity of substructure properties, for example the number and radial location of rings and gaps, suggests that specific properties of disk substructures might be sensitive to disk properties such as the gas surface density, temperature, gas-to-dust ratio, and perhaps

the chemical inventory.

While there are some suggestive findings, we find that connecting observed substructure properties with theoretical prediction is not always straightforward even with the data taken with state-of-the-art observing facilities. This could be because the quality of the data is still not sufficient or too inhomogeneous to differentiate between various mechanisms. It must be also due in part to the fact that theoretical/numerical studies often consider the gas only, while a large fraction of substructures have been observed in continuum observations, making one-to-one comparison between theoretical predictions and observations less straightforward. In addition, theoretical studies tend to prefer simplified models to highlight the fundamental physical processes. However, in order for more proper comparison with observations, theoretical models have to include all relevant physical processes. The challenges in connecting substructure properties to theoretical predictions can also be due to that different mechanisms operate in different disks so that we do not see clear correlation among the substructure properties. In the end, this all may suggest that we need to find the cause of substructures more directly, rather than relying on substructure properties to infer their cause.

Observations of protoplanetary disks in the last few years have focused on the discovery of substructures. The new discoveries certainly have infused new energy in the study of disk evolution and planet formation. As we discussed, however, it is very challenging to infer the origin based on the morphology only. In the coming years, better morphological characterization of and kinematics associated with individual substructures using high angular/spectral resolution and sensitivity, across a larger sample including small and faint disks, will help to determine the cause of disk substructures.

Acknowledgments. We thank reviewers, Jonathan Williams, Xue-Ning Bai, and an anonymous reviewer, for carefully reading the Chapter and providing us suggestions that greatly helped to improve the Chapter.

TABLE 1
SYSTEMS WITH RINGS

2MASS Name	Alt. Name	d (pc)	M_* (M_\odot)	L_* (L_\odot)	Class	M_d ($0.01 M_\odot$)	λ	n	Ring location (au)	Ring FWHM (au)	FWHM (au)	FWHM (au)	binary sep. ($''$)	ref
J04345542+2428531	AA Tau	137	0.5	0.7	II	1	mm	3	48.7,94.9,142.6	2.6,28.7,26.4	21		-	1
J04335200+2250301	CI Tau	159	0.9	1.6	II	2.3	mm	4	27.7,62.0,99.2,152.8	19.3,29.4,8.7,59.7	19		-	2,3,4
J04141760+2806096	CIDA1	138	0.2	0.2	II	0.2	mm	2	16.2,21	3.5,9.7	6		-	5,6
J05052286+2531312	CIDA9A	172	0.5	0.1	II	0.9	mm	1	39.52	25.31	21		2.3	3,4,27,28
J04333906+2520382	DL Tau	159	0.9	1.5	II	3.7	mm	3	46.4,78.1,112.27	14.6,3.8,6,29.6	20		-	3,4
J04334871+1810099	DM Tau	145	0.3	0.2	TD	1.6	mm	1	24	16	5		-	7,8,9
J04352737+2414589	DNTau	128	0.5	0.7	II	1.2	mm	2	15.4,53.4	21.1,7.7	15		-	3,10
J04474859+2925112	DSTau	159	0.5	1	II	0.4	mm	1	56.8	17.2	19		6.2	4,27
J04233919+2456141	FTT Tau	128	0.3	0.4	II	1.3	mm	1	31.1	16.5	15		-	4
J04551098+3021595	GMAur	160	0.8	1.2	TD	3.8	mm	3	37.87,177	9.6,13,50.4	6		-	9,11,12
J04430309+2520187	GOTau	145	0.4	0.3	II	1	mm	2	73.0,109.45	9.8,22.2	18		-	3,10
J04245708+2711565	IP Tau	131	0.5	0.5	II	0.1	mm	1	27.1	10.4	16		-	4,10
J04295156+2606448	IQ Tau	131	0.4	0.8	II	0.9	mm	2	48.2,82.8	11.8,24.5	18		-	3,10
J04154278+2909597	IRAS04125+2902	160	0.4	0.5	TD	0.4	mm	1	55	30	48		-	13,14
J04391779+2221034	LkCa15	159	0.9	1.1	TD	2.7	mm	2	69.0,100.11	14.8,34	9		-	15,16,17
J04322210+1827426	MHO6	142	0.2	0.1	II	0.2	mm	1	58	-	9		-	36
J04584626+2950370	MWC480/HD31648	162	2.1	21.9	II	5.7	mm	1	20	20	14		-	6
J04215740+2826355	RY Tau	128	2.0	12.3	II	2.7	mm	2	97.6	12.6	23		-	3
J04300399+1813493	UX TauA	140	1.7	3.2	TD	0.9	mm	1	18.2,49.04	25.6,19.5	16		-	3,4,19
J04313843+1813576	HL Tau	140	1	11	I	13	mm	7	37.5	11	18		2.7	28,29,30,31
J05355845+2444542	CQ Tau	162	1.7	10	II	2.3	mm	1	21.4,40.0,49,~58, 72.2,85.4,102	12.9,6.4,4.2,<15, 5.1,12.0,<20	4		-	20,21
J05380526-0115216	V1247 Ori	398	1.9	15.8	PTD	7.7	mm	1	45	23	16		-	20,21
J16255615-2420481	SR4	135	0.8	1.8	II	1.1	mm	1	75	40	16		-	22,23,24
J16261033-2420548	GSS26/ISO-Oph17	139	0.7	4	II	2.9	mm	2	18	13.3	5		-	25,26
J16261886-2428196	Elias2-20	138	0.9	2.6	II	1.6	mm	2	25.47	7.20	3		-	21,32
J16262367-2443138	DoAr25	138	0.8	1.5	II	3.9	mm	3	29.36	5.2,1.9	4		-	33,34
J16262407-2416134	Elias2-24	134	1.1	6.8	II	5.5	mm	2	86,111,137	-14.3,12.8	4		-	21,32
J16264502-2423077	GSS39/Elias2-27	116	0.6	1.5	II	3.6	mm	1	77,12.3	12.2,-	5		-	21,32
J16273718-2430350	IRS48/WLY2-48	121	2	14.3	TD	0.7	mm	1	86	21	6		-	21,32,33
J16273901-2358187	DoAr33	140	1	1.6	II	0.6	mm	1	60	-	24		-	37
J16273942-2439155	ROX27/W5B52	137	0.5	1.1	II	1.1	mm	1	17	-	4		-	21,32
J16281650-2436579	ISO-Oph196/W5B60	137	0.2	0.3	II	1.6	mm	2	25	-	3		-	21,32
									8.34	8.16	5		-	34

TABLE 1
SYSTEMS WITH RINGS

2MASS Name	Alt. Name	d (pc)	M_* (M_\odot)	L_* (L_\odot)	Class	M_d ($0.01M_\odot$)	λ	n	Ring location (au)	Ring FWHM (au)	FWHM (au)	binary sep. ($''$)	ref
J16313565-2401294	WLY2-63/IRS63	144	-	-	I/FS	5.9	mm	2	27.0,51.1	5.7,13.0	6	-	35
J16313346-2427372	DoAr44	146	1.4	1	II/PT	1.5	mm	1	47	13	4	-	32,34
J16335560-2442049	RXJ1633.9-2442	139	1	1	II/TD	1.3	mm	1	36	18	3	-	32,34
J16394544-2402039	WSB82	139	1.5	5.1	II	3.2	mm	1	50	50	3	-	32,34
J16491530-1422087	AS209	121	0.8	1.4	II	3.6	mm	7	14.2,27.8,38.7, 74.2,96.7,120.14,141	8.9,4.7,3.4, 9.3,8.1,11.2,2.8	5	-	38
J16265843-2445318	SR24S	114	1.6	3.8	II	2.3	mm	1	42.2	21.4	4	5.2	32,34,39
J16271027-241912	SR21	138	2.5	12.6	II	2.9	mm	2	31.53	<14,25	14	-	40,41
J17562128-2157218	HD163296	101	2	17	II	6.2	ir	2	19.55	-	7	-	42
J10563044-7711393	T4/SYCha	181	0.8	1	II	1.3	mm	1	64	-	8	-	44
J10581677-7717170	SZCha	190	1.3	1.9	II/TD	3.8	mm	1	90	45	90	-	45
J11022491-7733357	CSCCha	176	1.5	1.4	TD	2.4	mm	1	35.2	45	95	-	45
J11081509-7733531	HPCha	190	1.4	1.3	TD	2.6	mm	1	42	<12	10	-	31,45,46
J11100010-7634578	WWCha	192	1.9	2.7	II	17.2	mm	2	67,122	8.75	8	-	45
J11332542-7011412	HD100546	110	2.2	25.1	TD	4.3	mm	2	20.5,29.7	8.3,25	13	-	47
J11015191-3442170	TWHyA	60	0.5	0.3	II	1.7	mm	5	3.0,29.5,33,44.7,~52	2.2,<6,<10,2.8,-	6	-	48,49
J14081015-4123525	PDS70	140	0.8	0.6	TD	1.2	mm	1	74	28	3	-	50,51,52
J15560921-3756057	Sz82,IMLup	158	1	2.6	II	4.4	ir	1	70	-	10	-	53
J15564188-4219232	HD142527	157	2.1	16.2	II/TD	24.9	mm	2	117.4,133.5	15.8,18.4	8	-	21,54
J15564230-3749154	Sz83,RULup	160	0.7	1.5	II	3.6	mm	4	205	70	31	0.1	55
J16071159-3903475	Sz91	159	0.5	0.2	TD	0.2	mm	1	17.24,34.50	<8.5,5,-	4	-	21
J16083070-3828268	-	156	1.5	1.8	TD	0.8	mm	1	110.5	51.7	40	-	54
J16083617-3923024	V1094Sco	154	0.8	1.1	II	3.6	mm	2	70	30	47	-	54
J16085468-3937431	Sz111	158	0.5	0.2	TD	1.3	mm	1	130,170	-	14	-	54
J16090141-3925119	-	164	0.2	0.1	TD	0.1	mm	1	56	30	14	-	46
J16094864-3911169	Sz118	164	1	0.7	II	0.5	mm	1	30	-	49	-	54
J16105158-3853137	Sz123A	158	0.6	0.1	II	0.3	mm	1	50	-	49	-	54
J15154844-3709160	SAO206462/HD135344B	135	1.6	9.8	TD	2.3	mm	1	35	15	8	-	-
J15583692-2257153	HD143006	166	1.4	3.9	II	0.9	mm	3	51.3	19	24	-	56
J16042165-2130284	J1604-2130	150	1	0.6	TD	0.9	mm	1	7.7,40.0,63.6	6,10,22	7	-	21
J16100501-2132318	-	145	0.7	0.5	II	0.3	ir	1	70	<30	34	-	38
J16100501-2132318	-	145	0.7	0.5	II	0.3	mm	2	60	-	11	-	57
J16100501-2132318	-	145	0.7	0.5	II	0.3	mm	2	28.8,41.1	5.7,7.9	7	-	17

NOTE.—References: Stellar distances, masses, and luminosities are taken from *Tesit et al. (2022)* and references therein. Dust ring properties were taken from: (1) *Loomis et al. (2017)*, (2) *Clarke et al. (2018)*, (3) *Long et al. (2018)*, (4) *Long et al. (2019)*, (5) *Pinilla et al. (2021)*, (6) *Kurtovic et al. (2021)*, (7) *Hashimoto et al. (2021)*, (8) *Andrews et al. (2011b)*, (9) *Isella et al. (2009)*, (10) *Andrews et al. (2009)*, (11) *Hughes et al. (2009)*, (12) *Huang et al. (2020a)*, (13) *Luhman et al. (2011)*, (14) *Español*

et al. (2015), (15) *Andrews et al.* (2011b), (16) *Isella et al.* (2012), (17) *Facchini et al.* (2020), (19) *Isella et al.* (2010), (20) *ALMA Partnership et al.* (2015), (21) *Huang et al.* (2018b), (22) *Ubeira Gabellini et al.* (2019), (23) *Uyama et al.* (2020b), (24) *Wölfer et al.* (2021), (25) *Ohta et al.* (2016), (26) *Kraus et al.* (2017), (27) *Akeson and Jensen* (2014), (28) *Pinilla et al.* (2018), (29) *Ménard et al.* (2020), (30) *Zapata et al.* (2020), (31) *Francis and van der Marel* (2020), (32) *Cieza et al.* (2019), (33) *Simon et al.* (2017), (34) *Cieza et al.* (2021), (35) *Segura-Cox et al.* (2020), (36) *Thadmann et al.* (2016), (37) *Fallette et al.* (2015), (38) *Andrews et al.* (2018b), (39) *Pinilla et al.* (2017b), (40) *Pérez et al.* (2014), (41) *Pinilla et al.* (2015), (42) *Muro-Arena et al.* (2020), (43) *Isella et al.* (2018), (44) *Giadit et al.* (2018), (45) *Pascucci et al.* (2016), (46) *Norfolk et al.* (2021), (47) *Pérez et al.* (2020), (48) *Andrews et al.* (2016), (49) *Tsuikagoshi et al.* (2016), (50) *Keppeler et al.* (2019), (51) *Isella et al.* (2019), (52) *Benisty et al.* (2021), (53) *Hashimoto et al.* (2012), (54) *Ansdell et al.* (2018), (55) *Fukagawa et al.* (2013), (56) *van der Marel et al.* (2016), (57) *Mayama et al.* (2012)

TABLE 2
SYSTEMS WITH SPIRALS

2MASS Name	Alt. Name	d (pc)	M_* (M_\odot)	L_* (L_\odot)	Class	M_d ($0.01 M_\odot$)	λ	m	ψ ($^\circ$)	radial extent (au)	FWHM (au)	binary sep. ($''$)	ref
J03454828+3224118	LkHa330	309	2.95	22.91	II	16.97	ir	2	12-16	60-150	46	-	5,9
J04300399+1813493	UXTauA	140	1.67	3.24	TD	0.91	mm line	2	20-30	140-280	18	2.7	11
							ir	2	-	-	18	2.7	12
J04554582+3033043	ABAur	163	3.17	123.03	II	2.12	mm line	2	20	30-90	18	-	1
							ir	8	22	30-100	10	-	2
J04555938+3034015	SUAur	158	2.18	14.45	II	0.58	ir	6	-	-	11	-	10
J05194140+0538428	HD34700A	356	4.1	25.12	II	0.8	ir	6	27-55	110-320	18	5.2	13,14
J05302753+2519571	MWC758/HD36112	156	1.5	10.96	II	1.16	mm	2	19	30-80	31	-	3,4,5
							ir	2	19	30-80	4	-	6
J05355845+2444542	CQTau	162	1.67	10	II	2.31	mm line	2	20-40	30-65	19	-	7
							ir	2	4, 34	30-60	16	-	8
J05380526-0115216	V1247Ori	398	1.9	15.81	PTD	7.72	ir	1	6.5	96-119	16	-	5
J11015191-3442170	TWHya	60	0.8	0.28	II	1.72	mm line	3	3-9	70-210	1	-	21
J11100010-7634578	WWCha	192	1.9	2.69	II	17.18	ir	1	-	-	13	-	19
J11330559-5419285	HD100453	103	1.5	10	-	1.35	mm	2	5-7	20-30	3	1.045	26
							mm line	2	11-25	30-100	5	1.045	26
							ir	2	14-18	20-30	3	1.045	26
J11332542-7011412	HD100546	110	2.2	25.12	TD	4.34	ir	6	-	-	6	-	20
J11493184-7851011	DZCha	110	0.5	1	-	0.07	ir	2	27	5-25	6	-	5
J15154844-3709160	SAO206462/HD135344B	135	1.6	9.77	TD	10.79	ir	2	11	38-107	12	-	5,27
J15451286-3417305	Sz68/HTLup	154	2.15	5.37	II	1.35	mm	2	17	13-39	4	2.8	23
J15560921-3756057	Sz82/IMLup	158	0.95	2.57	II	4.37	mm	2	10-22	30-94	8	-	16
J15564188-4219232	HD142527	157	2.1	16.22	II/TD	24.85	mm line	3	3-17	290-670	31	0.1	24
							ir	6	-	80-130	31	0.1	5,25
J15564230-3749154	Sz83/RULup	160	0.67	1.48	II	3.65	mm line	5	21-31	250-1200	4	-	22
J16113134-1838259	AS205N	128	0.99	2.19	-	12.65	mm	2	14	19-68	6	1.3	23
J16264502-2423077	GSS39/Elias2-27	116	0.63	1.51	II	3.59	mm	2	16	47-244	6	-	15,16
J16484562-1416359	WaOph6	123	0.68	2.88	II	2.08	mm	2	14.9-18	20-70	7	-	16
							ir	2	14-20	20-45	7	-	17
-	SR21	138	2.5	12.59	II	2.93	ir	2	2-14	25-40	7	-	18

NOTE.—References: Stellar distances, masses, and luminosities are taken from *Testi et al. (2022)* and references therein. Spiral properties are taken from: (1) *Tang et al. (2017)*, (2) *Hashimoto et al. (2011)*, (3) *Dong et al. (2018b)*, (4) *Boehler et al. (2018)*, (5) *Yu et al. (2019)*, (6) *Ren et al. (2020)*, (7) *Wölfer et al. (2021)*, (8) *Uyama et al. (2020a)*, (9) *Uyama et al. (2018)*, (10) *Ginski et al. (2021)*, (11) *Zapata et al. (2020)*, (12) *Ménard et al. (2020)*, (13) *Monnier et al. (2019)*, (14) *Uyama et al. (2020b)*, (15) *Andrews et al. (2018b)*, (16) *Huang et al. (2018c)*, (17) *Brown-Sevilla et al. (2021)*, (18) *Muro-Arena et al. (2020)*, (19) *Garufi et al. (2020)*, (20) *Follette et al. (2017)*, (21) *Teague et al. (2019)*, (22) *Huang et al. (2020b)*, (23) *Kurtovic et al. (2018)*, (24) *Christiaens et al. (2014)*, (25) *Avenhaus et al. (2014)*, (26) *Rosotti et al. (2020a)*, (27) *Garufi et al. (2013)*

TABLE 3
SYSTEMS WITH CRESCENTS

2MASS Name	Alt. Name	d (pc)	M_* (M_\odot)	L_* (L_\odot)	Class	M_d ($0.01 M_\odot$)	λ	n	rad (au)	w_r (au)	w_ϕ (au)	Δ	FWHM (au)	binary sep. ($''$)	ref
J03454828+3224118	LkHa330	309	2.95	22.91	II	16.97	mm	1	130	< 36	116	3.3	93	-	1
J04554582+3033043	ABAur	163	3.17	123.03	II	2.12	mm	1	120	< 50	140	3-4	23	-	2
J05194140+0538428	HD34700A	356	4.1 ^a	25.12	II	0.8	mm	1	155	72	173	>26	18	5.2	3
J05302753+2519571	MWC758/HD36112	156	1.5	10.96	II	1.16	mm	2	48,83	12,25	47,78	4,4,10	6	-	4
J05380526-0115216	V1247Ori	398	1.9	15.81	PTD	7.72	mm	1	158	20	-	5	16	-	5
J11332542-7011412	HD100546	110	2.2	25.12	TD	4.34	mm	1	21.8	22	40	1.5	6	-	6
J15154844-3709160	SAO206462/HD135344B	135	1.6	9.77	TD	10.79	mm	1	80.7	14.8	188	>4	24	-	7
J15404638-4229536	HD139614	135	1.6	9.23	-	3.02	ir	4	-	-	-	-	68	0.04	8
J15564188-4219232	HD142527	157	2.1	16.22	II/TD	24.85	mm	1	185	80	94	20-40	31	0.1	9
J15583692-2257153	HD143006	166	1.4	3.89	II	4.12	mm	1	74	11	50	>40	7	-	10
							ir	2	40,74	-	-	-	6	-	11
J16273718-2430350	IRS48/WLY2-48	121	2	14.29	TD	0.65	mm	1	63	42	110	>130	60	-	12
J17562128-2157218	HD163296	101	2	16.98	II	6.23	mm	1	55	~7	~48	>20	4	-	10
-	SR21	138	2.5	12.59	II	2.93	mm	1	46	34	95	~2	14	-	13

NOTE.—^a HD 34700A is a spectroscopic binary system and the stellar mass refers to the total mass of the systems. References: Stellar distances, masses, and luminosities are taken from *Testi et al. (2022)* and references therein. Crescent properties are taken from: (1) *Isella et al. (2013)*, (2) *Tang et al. (2017)*, (3) *Benac et al. (2020)*, (4) *Dong et al. (2018b)*, (5) *Kraus et al. (2017)*, (6) *Pérez et al. (2020)*, (7) *Pérez et al. (2014)*, (8) *Muro-Arena et al. (2020)*, (9) *Boehler et al. (2021)*, (10) *Andrews et al. (2018b)*, (11) *Benisty et al. (2018)*, (12) *van der Marel et al. (2013)*, (13) *Pinilla et al. (2015)*

TABLE 4
SUGGESTED FUTURE OBSERVATIONS TO DETERMINE THE ORIGIN OF SUBSTRUCTURES

Origin	Associated substructures	Diagnostics	Required observations
RWI (§4.1)	spiral/crescent	vorticity across the crescent	high angular + velocity resolution line observations
VSI (§4.2)	ring/crescent	corrugated vertical flows	high angular + velocity resolution line observations
COS (§4.3)	crescent	crescents in the inner few AU	high angular resolution observations with ngVLA
ZVI (§4.4)	crescent	crescents in the inner few AU	high angular resolution observations with ngVLA
eccentric modes (§4.5)	spiral	small pitch angle ($\lesssim 5^\circ$) and pattern speed ($\ll \Omega_K$)	high angular resolution NIR/molecular line observations + monitoring
infall (§4.6)	spiral/crescent	detection of large-scale envelope and streamers	medium/low angular resolution mosaic line observations
		shocks	shock tracers (e.g., SO), chemical tracers
photoevaporation (§4.7)	ring	detection of outflowing gas	molecular line observations in IR and mm wavelengths
zonal flows (§5.1.1, §5.2.2)	ring	direct detection of magnetic fields within rings/gaps	continuum/line polarization observations
MRI turbulence (§5.1.2)	spiral	direct detection of magnetic fields	continuum/line polarization observations
dead-zone (§5.2.1)	ring	variable level of turbulence inside/outside a ring	turbulence measurement using line observations
companion (§6.1)	ring/spiral/crescent	direct detection (IR, H α , CPD)	high angular resolution & high contrast imaging
		kinematic planetary signatures	high angular + velocity resolution line observations
stellar flyby (§6.2)	spiral	direct detection of flyby stars	large field-of-view imaging, proper motion with Gaia
GH (§7.1)	spiral	large disk mass, Toomre Q parameter	measure surface density & temperature
		spiral pattern speed & pitch angle	long-term monitoring, high angular resolution imaging
iceline (§8.1)	ring	condensation temperature	direct temperature measurements at the location of rings/gaps
		grain size changes across icelines	multi-wavelength continuum observations
dust-induced instabilities (§8.2)	ring	high dust-to-gas mass ratio	measure both gas and dust surface density

REFERENCES

- Adachi I. et al., 1976 *Progress of Theoretical Physics*, 56, 1756.
- Adams F. C., 2010 *ARA&A*, 48, 47.
- Adams F. C. and Watkins R., 1995 *ApJ*, 451, 314.
- Akeson R. L. and Jensen E. L. N., 2014 *ApJ*, 784, 1, 62.
- Akiyama E. et al., 2019 *AJ*, 157, 4, 165.
- Alexander R. et al., 2014 *Protostars and Planets VI* (H. Beuther, R. S. Klessen, C. P. Dullemond, and T. Henning), p. 475.
- ALMA Partnership et al., 2015 *ApJL*, 808, 1, L3.
- Alves F. O. et al., 2020 *ApJL*, 904, 1, L6.
- Aly H. et al., 2015 *MNRAS*, 449, 65.
- Andrews S. M. et al., 2009 *ApJ*, 700, 2, 1502.
- Andrews S. M. et al., 2011a *ApJL*, 742, 1, L5.
- Andrews S. M. et al., 2011b *ApJ*, 732, 1, 42.
- Andrews S. M. et al., 2013 *ApJ*, 771, 2, 129.
- Andrews S. M. et al., 2016 *ApJL*, 820, 2, L40.
- Andrews S. M. et al., 2018a *ApJ*, 865, 2, 157.
- Andrews S. M. et al., 2018b *ApJL*, 869, 2, L41.
- Ansdell M. et al., 2018 *ApJ*, 859, 1, 21.
- Arlt R. and Urpin V., 2004 *A&A*, 426, 755.
- Artymowicz P. and Lubow S. H., 1994 *ApJ*, 421, 651.
- Artymowicz P. and Lubow S. H., 1996 *ApJL*, 467, L77.
- Arzamasskiy L. et al., 2018 *MNRAS*, 475, 3, 3201.
- Asensio-Torres R. et al., 2021 *A&A*, 652, A101.
- Avenhaus H. et al., 2014 *ApJ*, 781, 2, 87.
- Avenhaus H. et al., 2018 *ApJ*, 863, 1, 44.
- Bae J. and Zhu Z., 2018a *ApJ*, 859, 2, 118.
- Bae J. and Zhu Z., 2018b *ApJ*, 859, 2, 119.
- Bae J. et al., 2013 *ApJ*, 774, 1, 57.
- Bae J. et al., 2014 *ApJ*, 795, 1, 61.
- Bae J. et al., 2015 *ApJ*, 805, 1, 15.
- Bae J. et al., 2016a *ApJ*, 819, 2, 134.
- Bae J. et al., 2016b *ApJ*, 829, 1, 13.
- Bae J. et al., 2016c *ApJ*, 833, 2, 126.
- Bae J. et al., 2017 *ApJ*, 850, 2, 201.
- Bae J. et al., 2019 *ApJL*, 884, 2, L41.
- Bae J. et al., 2021 *ApJ*, 912, 1, 56.
- Bae J. et al., 2022 *ApJL*, 934, 2, L20.
- Baehr H. and Klahr H., 2015 *ApJ*, 814, 2, 155.
- Baehr H. and Zhu Z., 2021a *ApJ*, 909, 2, 135.
- Baehr H. and Zhu Z., 2021b *ApJ*, 909, 2, 136.
- Bai X.-N., 2015 *ApJ*, 798, 2, 84.
- Bai X.-N. and Stone J. M., 2013 *ApJ*, 769, 1, 76.
- Bai X.-N. and Stone J. M., 2014 *ApJ*, 796, 1, 31.
- Balbus S. A. and Hawley J. F., 1991 *ApJ*, 376, 214.
- Bally J. and Scoville N. Z., 1982 *ApJ*, 255, 497.
- Banzatti A. et al., 2015 *ApJL*, 815, 1, L15.
- Banzatti A. et al., 2022 *arXiv e-prints*, arXiv:2202.03438.
- Barenfeld S. A. et al., 2017 *ApJ*, 851, 2, 85.
- Barge P. and Sommeria J., 1995 *A&A*, 295, L1.
- Barranco J. A. and Marcus P. S., 2005 *ApJ*, 623, 2, 1157.
- Barranco J. A. et al., 2018 *ApJ*, 869, 2, 127.
- Barraza-Alfaro M. et al., 2021 *A&A*, 653, A113.
- Baruteau C. et al., 2014 *Protostars and Planets VI* (H. Beuther, R. S. Klessen, C. P. Dullemond, and T. Henning), p. 667.
- Bate M. R. et al., 2000 *MNRAS*, 317, 4, 773.
- Benac P. et al., 2020 *ApJ*, 905, 2, 120.
- Benisty M. et al., 2015 *A&A*, 578, L6.
- Benisty M. et al., 2017 *A&A*, 597, A42.
- Benisty M. et al., 2018 *A&A*, 619, A171.
- Benisty M. et al., 2021 *ApJL*, 916, 1, L2.
- Béthune W. et al., 2016 *A&A*, 589, A87.
- Béthune W. et al., 2017 *A&A*, 600, A75.
- Béthune W. et al., 2021 *A&A*, 650, A49.
- Bi J. et al., 2020 *ApJL*, 895, 1, L18.
- Bi J. et al., 2021 *ApJ*, 912, 2, 107.
- Binkert F. et al., 2021 *MNRAS*, 506, 4, 5969.
- Birnstiel T. et al., 2010 *A&A*, 513, A79.
- Birnstiel T. et al., 2013 *A&A*, 550, L8.
- Birnstiel T. et al., 2018 *ApJL*, 869, 2, L45.
- Blanco D. et al., 2021 *arXiv e-prints*, arXiv:2108.00907.
- Blandford R. D. and Payne D. G., 1982 *MNRAS*, 199, 883.
- Blum J. and Wurm G., 2000 *Icarus*, 143, 138.
- Boehler Y. et al., 2018 *ApJ*, 853, 2, 162.
- Boehler Y. et al., 2021 *A&A*, 650, A59.
- Bohn A. J. et al., 2021 *arXiv e-prints*, arXiv:2112.00123.
- Booth R. A. and Clarke C. J., 2019 *MNRAS*, 483, 3, 3718.
- Boss A. P., 1997 *Science*, 276, 1836.
- Brandenburg A. and Zweibel E. G., 1994 *ApJL*, 427, L91.
- Brown-Sevilla S. B. et al., 2021 *arXiv e-prints*, arXiv:2107.13560.
- Carpenter J. M., 2000 *AJ*, 120, 6, 3139.
- Carrera D. et al., 2021 *AJ*, 161, 2, 96.
- Casassus S. and Pérez S., 2019 *ApJL*, 883, 2, L41.
- Casassus S. et al., 2018 *MNRAS*, 477, 4, 5104.
- Cassen P. and Moosman A., 1981 *Icarus*, 48, 3, 353.
- Chambers J., 2021 *ApJ*, 914, 2, 102.
- Chen C. et al., 2019 *MNRAS*, 490, 4, 5634.
- Chen E. et al., 2021 *ApJ*, 906, 1, 19.
- Chiang E. I. and Goldreich P., 1997 *ApJ*, 490, 1, 368.
- Christiaens V. et al., 2014 *ApJL*, 785, 1, L12.
- Cieza L. A. et al., 2019 *MNRAS*, 482, 1, 698.
- Cieza L. A. et al., 2021 *MNRAS*, 501, 2, 2934.
- Cimerman N. P. and Rafikov R. R., 2021 *MNRAS*.
- Clarke C. J. et al., 2018 *ApJL*, 866, 1, L6.
- Cossins P. et al., 2009 *MNRAS*, 393, 4, 1157.
- Cossins P. et al., 2010a *MNRAS*, 407, 1, 181.
- Cossins P. et al., 2010b *MNRAS*, 401, 4, 2587.
- Crnkovic-Rubsamen I. et al., 2015 *MNRAS*, 450, 4, 4285.
- Cuello N. et al., 2019 *MNRAS*, 483, 3, 4114.
- Cui C. and Bai X.-N., 2021 *MNRAS*, 507, 1, 1106.
- Cui C. and Lin M.-K., 2021 *MNRAS*, 505, 2, 2983.
- Currie T. et al., 2022 *Nature Astronomy*, 6, 751.
- Czekala I. et al., 2019 *ApJ*, 883, 1, 22.
- D'Alessio P. et al., 1998 *ApJ*, 500, 1, 411.
- de Val-Borro M. et al., 2007 *A&A*, 471, 3, 1043.
- Deng H. et al., 2021 *Nature Astronomy*, 5, 440.
- Doi K. and Kataoka A., 2021 *ApJ*, 912, 2, 164.
- Dominik C. and Tielens A. G. G. M., 1997 *ApJ*, 480, 2, 647.
- Dong R. and Fung J., 2017 *ApJ*, 835, 2, 146.
- Dong R. et al., 2015 *ApJL*, 812, 2, L32.
- Dong R. et al., 2017 *ApJ*, 843, 2, 127.
- Dong R. et al., 2018a *ApJ*, 866, 2, 110.
- Dong R. et al., 2018b *ApJ*, 860, 2, 124.
- Doolin S. and Blundell K. M., 2011 *MNRAS*, 418, 2656.
- Draine B. T., 2016 *ApJ*, 831, 1, 109.
- Drazkowska J. and Alibert Y., 2017 *A&A*, 608, A92.
- Duffell P. C. and MacFadyen A. I., 2013 *ApJ*, 769, 1, 41.
- Dullemond C. P., 2000 *A&A*, 361, L17.
- Dullemond C. P. and Penzlin A. B. T., 2018 *A&A*, 609, A50.
- Dullemond C. P. et al., 2001 *ApJ*, 560, 2, 957.
- Dullemond C. P. et al., 2018 *ApJL*, 869, 2, L46.
- Dullemond C. P. et al., 2020 *A&A*, 633, A137.
- Dutrey A. et al., 2014 *Protostars and Planets VI* (H. Beuther, R. S.

- Klessen, C. P. Dullemond, and T. Henning), p. 317.
- Dzyurkevich N. et al., 2013 *ApJ*, 765, 2, 114.
- Epstein P. S., 1924 *Physical Review*, 23, 6, 710.
- Ercolano B. et al., 2021 *MNRAS*, 508, 2, 1675.
- Espaillat C. et al., 2014 *Protostars and Planets VI* (H. Beuther, R. S. Klessen, C. P. Dullemond, and T. Henning), p. 497.
- Espaillat C. et al., 2015 *ApJ*, 807, 2, 156.
- Evans Neal J. I. et al., 2009 *ApJS*, 181, 2, 321.
- Evans M. G. et al., 2017 *MNRAS*, 470, 2, 1828.
- Facchini S. et al., 2013 *MNRAS*, 433, 2142.
- Facchini S. et al., 2018 *MNRAS*, 473, 4, 4459.
- Facchini S. et al., 2020 *A&A*, 639, A121.
- Fairbairn C. W. and Rafikov R. R., 2022 *MNRAS*.
- Farago F. and Laskar J., 2010 *MNRAS*, 401, 1189.
- Flaherty K. et al., 2020 *ApJ*, 895, 2, 109.
- Flaherty K. M. et al., 2017 *ApJ*, 843, 2, 150.
- Flaherty K. M. et al., 2018 *ApJ*, 856, 2, 117.
- Flock M. et al., 2011 *ApJ*, 735, 2, 122.
- Flock M. et al., 2015 *A&A*, 574, A68.
- Flock M. et al., 2016 *ApJ*, 827, 2, 144.
- Flock M. et al., 2017a *ApJ*, 835, 2, 230.
- Flock M. et al., 2017b *ApJ*, 850, 2, 131.
- Flock M. et al., 2019 *A&A*, 630, A147.
- Flock M. et al., 2020 *ApJ*, 897, 2, 155.
- Follette K. B. et al., 2015 *ApJ*, 798, 2, 132.
- Follette K. B. et al., 2017 *AJ*, 153, 6, 264.
- Forgan D. et al., 2011 *MNRAS*, 410, 2, 994.
- Forgan D. et al., 2012 *MNRAS*, 426, 3, 2419.
- Forgan D. H. et al., 2018 *ApJL*, 860, 1, L5.
- Foucart F. and Lai D., 2013 *ApJ*, 764, 106.
- Franchini A. et al., 2019a *ApJL*, 880, 2, L18.
- Franchini A. et al., 2019b *MNRAS*, 485, 315.
- Franchini A. et al., 2020 *MNRAS*, 491, 4, 5351.
- Francis L. and van der Marel N., 2020 *ApJ*, 892, 2, 111.
- Fu W. et al., 2014a *ApJL*, 795, 2, L39.
- Fu W. et al., 2014b *ApJL*, 788, 2, L41.
- Fu W. et al., 2015 *ApJ*, 807, 75.
- Fukagawa M. et al., 2006 *ApJL*, 636, 2, L153.
- Fukagawa M. et al., 2013 *PASJ*, 65, L14.
- Fukuhara Y. et al., 2021 *ApJ*, 914, 2, 132.
- Fung J. et al., 2014 *ApJ*, 782, 2, 88.
- Gammie C. F., 1996 *ApJ*, 457, 355.
- Gammie C. F., 2001 *ApJ*, 553, 1, 174.
- Gárate M. et al., 2021 *A&A*, 655, A18.
- Garufi A. et al., 2013 *A&A*, 560, A105.
- Garufi A. et al., 2020 *A&A*, 633, A82.
- Garufi A. et al., 2021 *arXiv e-prints*, arXiv:2110.13820.
- Gibbons P. G. et al., 2014 *MNRAS*, 442, 1, 361.
- Ginski C. et al., 2021 *ApJL*, 908, 2, L25.
- Ginzburg S. and Sari R., 2018 *MNRAS*, 479, 2, 1986.
- Goldreich P. and Tremaine S., 1978 *ApJ*, 222, 850.
- Goldreich P. and Tremaine S., 1979 *ApJ*, 233, 857.
- Gonzalez J. F. et al., 2017 *MNRAS*, 467, 2, 1984.
- Goodman J. and Rafikov R. R., 2001 *ApJ*, 552, 2, 793.
- Grady C. A. et al., 1999 *ApJL*, 523, 2, L151.
- Guidi G. et al., 2018 *MNRAS*, 479, 2, 1505.
- Gundlach B. and Blum J., 2015 *ApJ*, 798, 1, 34.
- Gundlach B. et al., 2018 *MNRAS*, 479, 1, 1273.
- Haffert S. Y. et al., 2019 *Nature Astronomy*, 3, 749.
- Hall C. et al., 2018 *MNRAS*, 477, 1, 1004.
- Hall C. et al., 2019 *ApJ*, 871, 2, 228.
- Hall C. et al., 2020 *ApJ*, 904, 2, 148.
- Harrison R. E. et al., 2021 *ApJ*, 908, 2, 141.
- Hashimoto J. et al., 2011 *ApJL*, 729, 2, L17.
- Hashimoto J. et al., 2012 *ApJL*, 758, 1, L19.
- Hashimoto J. et al., 2021 *ApJ*, 911, 1, 5.
- Hawley J. F., 2001 *ApJ*, 554, 1, 534.
- Hayashi C., 1981 *Progress of Theoretical Physics Supplement*, 70, 35.
- Heinemann T. and Papaloizou J. C. B., 2009a *MNRAS*, 397, 1, 52.
- Heinemann T. and Papaloizou J. C. B., 2009b *MNRAS*, 397, 1, 64.
- Helled R. et al., 2014 *Protostars and Planets VI* (H. Beuther, R. S. Klessen, C. P. Dullemond, and T. Henning), p. 643.
- Hendler N. et al., 2020 *ApJ*, 895, 2, 126.
- Hennebelle P. et al., 2016 *A&A*, 590, A22.
- Hennebelle P. et al., 2017 *A&A*, 599, A86.
- Hirose S. and Shi J.-M., 2019 *MNRAS*, 485, 1, 266.
- Hollenbach D. et al., 1994 *ApJ*, 428, 654.
- Hu X. et al., 2019 *ApJ*, 885, 1, 36.
- Hu X. et al., 2021 *ApJ*, 913, 2, 133.
- Hu X. et al., 2022 *arXiv e-prints*, arXiv:2203.05629.
- Huang J. et al., 2018a *ApJ*, 852, 2, 122.
- Huang J. et al., 2018b *ApJL*, 869, 2, L42.
- Huang J. et al., 2018c *ApJL*, 869, 2, L43.
- Huang J. et al., 2020a *ApJ*, 891, 1, 48.
- Huang J. et al., 2020b *ApJ*, 898, 2, 140.
- Huang P. et al., 2019 *ApJL*, 883, 2, L39.
- Hughes A. M. et al., 2009 *ApJ*, 698, 1, 131.
- Hyodo R. et al., 2019 *A&A*, 629, A90.
- Ida S. and Guillot T., 2016 *A&A*, 596, L3.
- Inaba S. and Barge P., 2006 *ApJ*, 649, 1, 415.
- Isella A. and Turner N. J., 2018 *ApJ*, 860, 1, 27.
- Isella A. et al., 2009 *ApJ*, 701, 1, 260.
- Isella A. et al., 2010 *ApJ*, 714, 2, 1746.
- Isella A. et al., 2012 *ApJ*, 747, 2, 136.
- Isella A. et al., 2013 *ApJ*, 775, 1, 30.
- Isella A. et al., 2014 *ApJ*, 788, 2, 129.
- Isella A. et al., 2016 *PhRvL*, 117, 25, 251101.
- Isella A. et al., 2018 *ApJL*, 869, 2, L49.
- Isella A. et al., 2019 *ApJL*, 879, 2, L25.
- Jacquemin-Ide J. et al., 2021 *A&A*, 647, A192.
- Jin S. et al., 2019 *ApJ*, 881, 2, 108.
- Johansen A. and Youdin A., 2007 *ApJ*, 662, 1, 627.
- Johansen A. et al., 2009 *ApJ*, 697, 2, 1269.
- Johansen A. et al., 2014 *Protostars and Planets VI* (H. Beuther, R. S. Klessen, C. P. Dullemond, and T. Henning), p. 547.
- Juhász A. and Facchini S., 2017 *MNRAS*, 466, 4, 4053.
- Juhász A. and Rosotti G. P., 2018 *MNRAS*, 474, 1, L32.
- Kanagawa K. D. et al., 2015a *MNRAS*, 448, 1, 994.
- Kanagawa K. D. et al., 2015b *ApJL*, 806, 1, L15.
- Kanagawa K. D. et al., 2016 *PASJ*, 68, 3, 43.
- Kanagawa K. D. et al., 2017 *PASJ*, 69, 6, 97.
- Kanagawa K. D. et al., 2020 *ApJ*, 892, 2, 83.
- Kanagawa K. D. et al., 2021 *arXiv e-prints*, arXiv:2109.09579.
- Kataoka A. et al., 2015 *ApJ*, 809, 1, 78.
- Kennedy G. M. et al., 2012 *MNRAS*, 421, 3, 2264.
- Kennedy G. M. et al., 2019 *Nature Astronomy*, 3, 230.
- Keppler M. et al., 2018 *A&A*, 617, A44.
- Keppler M. et al., 2019 *A&A*, 625, A118.
- Kimura H. et al., 2015 *ApJ*, 812, 1, 67.
- Klahr H. and Hubbard A., 2014 *ApJ*, 788, 1, 21.
- Kozai Y., 1962 *AJ*, 67, 591.
- Krapp L. et al., 2018 *ApJ*, 865, 2, 105.
- Kratter K. and Lodato G., 2016 *ARA&A*, 54, 271.

- Kraus S. et al., 2017 *ApJL*, 848, 1, L11.
 Kraus S. et al., 2020 *Science*, 369, 6508, 1233.
 Kuffmeier M. et al., 2017 *ApJ*, 846, 1, 7.
 Kuffmeier M. et al., 2018 *MNRAS*, 475, 2, 2642.
 Kunitomo M. et al., 2020 *MNRAS*, 492, 3, 3849.
 Kunz M. W. and Lesur G., 2013 *MNRAS*, 434, 3, 2295.
 Kurtovic N. T. et al., 2018 *ApJL*, 869, 2, L44.
 Kurtovic N. T. et al., 2021 *A&A*, 645, A139.
 Kuznetsova A. et al., 2022 *arXiv e-prints*, arXiv:2202.05301.
 Lada C. J. and Lada E. A., 2003 *ARA&A*, 41, 57.
 Larwood J. D. et al., 1996 *MNRAS*, 282, 597.
 Latter H. N. and Papaloizou J., 2018 *MNRAS*, 474, 3, 3110.
 Law C. J. et al., 2021 *ApJS*, 257, 1, 3.
 Lee W.-K. et al., 2019 *ApJ*, 872, 2, 184.
 Lesur G. and Papaloizou J. C. B., 2010 *A&A*, 513, A60.
 Lesur G. et al., 2015 *A&A*, 582, L9.
 Lesur G. R. J. and Latter H., 2016 *MNRAS*, 462, 4, 4549.
 Li H. et al., 2000 *ApJ*, 533, 2, 1023.
 Li J. et al., 2021 *ApJ*, 910, 1, 79.
 Li R. and Youdin A. N., 2021 *ApJ*, 919, 2, 107.
 Li R. et al., 2018a *ApJ*, 862, 1, 14.
 Li R. et al., 2018b *ApJ*, 862, 1, 14.
 Lidov M. L., 1962 *Planet. Space Sci.*, 9, 719.
 Lin M.-K., 2014 *MNRAS*, 437, 1, 575.
 Lin M.-K., 2015 *MNRAS*, 448, 4, 3806.
 Lin M.-K., 2019 *MNRAS*, 485, 4, 5221.
 Lin M.-K. and Papaloizou J. C. B., 2011 *MNRAS*, 415, 2, 1426.
 Lin M.-K. and Youdin A. N., 2015 *ApJ*, 811, 1, 17.
 Lodato G. and Clarke C. J., 2011 *MNRAS*, 413, 4, 2735.
 Lodato G. and Facchini S., 2013 *MNRAS*, 433, 2157.
 Lodato G. et al., 2019 *MNRAS*, 486, 1, 453.
 Long F. et al., 2018 *ApJ*, 869, 1, 17.
 Long F. et al., 2019 *ApJ*, 882, 1, 49.
 Long F. et al., 2022 *ApJL*, 937, 1, L1.
 Loomis R. A. et al., 2017 *ApJ*, 840, 1, 23.
 Lovelace R. V. E. and Hohlfield R. G., 2013 *MNRAS*, 429, 1, 529.
 Lovelace R. V. E. et al., 1999 *ApJ*, 513, 2, 805.
 Lubow S. H., 1991 *ApJ*, 381, 259.
 Lubow S. H. and Martin R. G., 2016 *ApJ*, 817, 30.
 Lubow S. H. and Martin R. G., 2018 *MNRAS*, 473, 3, 3733.
 Lubow S. H. and Ogilvie G. I., 2000 *ApJ*, 538, 326.
 Lubow S. H. and Zhu Z., 2014 *ApJ*, 785, 1, 32.
 Lubow S. H. et al., 2015 *ApJ*, 800, 96.
 Luhman K. L. et al., 2011 *ApJL*, 730, 1, L9.
 Lyra W., 2014 *ApJ*, 789, 1, 77.
 Lyra W. and Lin M.-K., 2013 *ApJ*, 775, 1, 17.
 Lyra W. and Mac Low M.-M., 2012 *ApJ*, 756, 1, 62.
 Lyra W. and Umurhan O. M., 2019 *PASP*, 131, 1001, 072001.
 Lyra W. et al., 2008 *A&A*, 491, 3, L41.
 Lyra W. et al., 2009 *A&A*, 493, 3, 1125.
 Lyra W. et al., 2015 *A&A*, 574, A10.
 Malygin M. G. et al., 2017 *A&A*, 605, A30.
 Manger N. et al., 2020 *MNRAS*, 499, 2, 1841.
 Marcus P. S. et al., 2013 *PhRvL*, 111, 8, 084501.
 Marcus P. S. et al., 2015 *ApJ*, 808, 1, 87.
 Marcus P. S. et al., 2016 *ApJ*, 833, 2, 148.
 Marino S. et al., 2015 *ApJL*, 798, 2, L44.
 Marley M. S. et al., 2007 *ApJ*, 655, 1, 541.
 Marr M. and Dong R., 2022 *ApJ*, 930, 1, 80.
 Martin R. G. and Livio M., 2012 *MNRAS*, 425, 1, L6.
 Martin R. G. and Lubow S. H., 2017 *ApJL*, 835, L28.
 Martin R. G. and Lubow S. H., 2019 *MNRAS*, 490, 1, 1332.
 Martin R. G. et al., 2014 *ApJL*, 792, L33.
 Martin R. G. et al., 2016 *MNRAS*, 458, 4345.
 Mayama S. et al., 2012 *ApJL*, 760, 2, L26.
 Mayama S. et al., 2018 *ApJL*, 868, 1, L3.
 McNally C. P. et al., 2020 *MNRAS*, 493, 3, 4382.
 Meheut H. et al., 2010 *A&A*, 516, A31.
 Ménard F. et al., 2020 *A&A*, 639, L1.
 Meru F. and Bate M. R., 2011 *MNRAS*, 411, 1, L1.
 Meru F. et al., 2019 *MNRAS*, 482, 3, 3678.
 Mesa D. et al., 2019 *A&A*, 632, A25.
 Michael S. et al., 2012 *ApJ*, 746, 1, 98.
 Min M. et al., 2017 *A&A*, 604, L10.
 Miranda R. and Lai D., 2015 *MNRAS*, 452, 2396.
 Miranda R. and Rafikov R. R., 2019 *ApJ*, 875, 1, 37.
 Miranda R. and Rafikov R. R., 2020 *ApJ*, 892, 1, 65.
 Miranda R. et al., 2017 *ApJ*, 835, 2, 118.
 Moll R., 2012 *A&A*, 548, A76.
 Monnier J. D. et al., 2019 *ApJ*, 872, 2, 122.
 Mordasini C. et al., 2017 *A&A*, 608, A72.
 Morishima R., 2012 *MNRAS*, 420, 4, 2851.
 Muñoz D. J. and Lithwick Y., 2020 *ApJ*, 905, 2, 106.
 Muro-Arena G. A. et al., 2020 *A&A*, 635, A121.
 Musiolik G. and Wurm G., 2019 *ApJ*, 873, 1, 58.
 Musiolik G. et al., 2016a *ApJ*, 818, 1, 16.
 Musiolik G. et al., 2016b *ApJ*, 827, 1, 63.
 Muto T. et al., 2012 *ApJL*, 748, 2, L22.
 Nakagawa Y. et al., 1986 *Icarus*, 67, 3, 375.
 Nazari P. et al., 2019 *MNRAS*, 485, 4, 5914.
 Nealon R. et al., 2019 *MNRAS*, 484, 4, 4951.
 Nelson R. P. et al., 2013 *MNRAS*, 435, 3, 2610.
 Nixon C. et al., 2013 *MNRAS*, 434, 1946.
 Nixon C. J. et al., 2011 *MNRAS*, 417, L66.
 Norfolk B. J. et al., 2021 *MNRAS*, 502, 4, 5779.
 Öberg K. I. et al., 2021 *ApJS*, 257, 1, 1.
 Ogilvie G. I. and Lubow S. H., 2002 *MNRAS*, 330, 4, 950.
 Ohashi S. and Kataoka A., 2019 *ApJ*, 886, 2, 103.
 Ohta Y. et al., 2016 *PASJ*, 68, 4, 53.
 Okuzumi S., 2009 *ApJ*, 698, 2, 1122.
 Okuzumi S. and Tazaki R., 2019 *ApJ*, 878, 2, 132.
 Okuzumi S. et al., 2016 *ApJ*, 821, 2, 82.
 Okuzumi S. et al., 2022 *arXiv e-prints*, arXiv:2201.09241.
 Ono T. et al., 2016 *ApJ*, 823, 2, 84.
 Ono T. et al., 2018 *ApJ*, 864, 1, 70.
 Owen J. E., 2020 *MNRAS*, 495, 3, 3160.
 Owen J. E. et al., 2012 *MNRAS*, 422, 3, 1880.
 Paardekooper S.-J., 2012 *MNRAS*, 421, 4, 3286.
 Paardekooper S.-J. et al., 2010 *ApJ*, 725, 1, 146.
 Paardekooper S.-J. et al., 2020 *MNRAS*, 499, 3, 4223.
 Paneque-Carreño T. et al., 2021 *ApJ*, 914, 2, 88.
 Papaloizou J. C. B. and Lin D. N. C., 1995 *ApJ*, 438, 841.
 Pascucci I. et al., 2016 *ApJ*, 831, 2, 125.
 Pérez L. M. et al., 2014 *ApJL*, 783, 1, L13.
 Pérez L. M. et al., 2018 *ApJL*, 869, 2, L50.
 Pérez S. et al., 2020 *ApJL*, 889, 1, L24.
 Pfeil T. and Klahr H., 2019 *ApJ*, 871, 2, 150.
 Picogna G. and Marzari F., 2015 *A&A*, 583, A133.
 Pierens A. and Lin M.-K., 2018 *MNRAS*, 479, 4, 4878.
 Pineda J. E. et al., 2020 *Nature Astronomy*, 4, 1158.
 Pinilla P. et al., 2012 *A&A*, 538, A114.
 Pinilla P. et al., 2015 *A&A*, 584, A16.
 Pinilla P. et al., 2017a *ApJ*, 845, 1, 68.
 Pinilla P. et al., 2017b *ApJ*, 845, 1, 68.

- Pinilla P. et al., 2018 *ApJ*, 859, 1, 32.
- Pinilla P. et al., 2021 *A&A*, 649, A122.
- Pinte C. et al., 2016 *ApJ*, 816, 1, 25.
- Pinte C. et al., 2018 *ApJL*, 860, 1, L13.
- Pinte C. et al., 2019 *Nature Astronomy*, 3, 1109.
- Pohl A. et al., 2015 *MNRAS*, 453, 2, 1768.
- Pollack J. B. et al., 1996 *Icarus*, 124, 1, 62.
- Price D. J. et al., 2018a *MNRAS*, 477, 1, 1270.
- Price D. J. et al., 2018b *PASA*, 35, e031.
- Raettig N. et al., 2021 *ApJ*, 913, 2, 92.
- Rafikov R. R., 2002 *ApJ*, 569, 2, 997.
- Rafikov R. R., 2005 *ApJL*, 621, 1, L69.
- Ragusa E. et al., 2017 *MNRAS*, 464, 2, 1449.
- Ragusa E. et al., 2020 *MNRAS*, 499, 3, 3362.
- Railton A. D. and Papaloizou J. C. B., 2014 *MNRAS*, 445, 4, 4409.
- Rayleigh L., 1917 *Proceedings of the Royal Society of London Series A*, 93, 648, 148.
- Raymond S. N. et al., 2014 *Protostars and Planets VI* (H. Beuther, R. S. Klessen, C. P. Dullemond, and T. Henning), p. 595.
- Ren B. et al., 2020 *ApJL*, 898, 2, L38.
- Rice W. K. M. et al., 2003 *MNRAS*, 339, 4, 1025.
- Rice W. K. M. et al., 2004 *MNRAS*, 355, 2, 543.
- Rice W. K. M. et al., 2005 *MNRAS*, 364, 1, L56.
- Rice W. K. M. et al., 2006 *MNRAS*, 372, 1, L9.
- Rice W. K. M. et al., 2012 *MNRAS*, 420, 2, 1640.
- Rice W. K. M. et al., 2014 *MNRAS*, 438, 2, 1593.
- Rich E. A. et al., 2021 *ApJ*, 913, 2, 138.
- Richard S. et al., 2016 *MNRAS*, 456, 4, 3571.
- Riols A. and Lesur G., 2018 *A&A*, 617, A117.
- Riols A. and Lesur G., 2019 *A&A*, 625, A108.
- Riols A. et al., 2020 *A&A*, 639, A95.
- Rogers P. D. and Wadsley J., 2012 *MNRAS*, 423, 2, 1896.
- Ros K. and Johansen A., 2013 *A&A*, 552, A137.
- Rosotti G. P. et al., 2020a *MNRAS*, 491, 1, 1335.
- Rosotti G. P. et al., 2020b *MNRAS*, 495, 1, 173.
- Ruge J. P. et al., 2016 *A&A*, 590, A17.
- Safronov V. S., 1972 *Evolution of the protoplanetary cloud and formation of the earth and planets*.
- Saito E. and Sirono S.-i., 2011 *ApJ*, 728, 1, 20.
- Salyk C. et al., 2014 *ApJ*, 792, 1, 68.
- Sanchis E. et al., 2020 *MNRAS*, 492, 3, 3440.
- Sano T. et al., 2000 *ApJ*, 543, 1, 486.
- Schoonenberg D. and Ormel C. W., 2017 *A&A*, 602, A21.
- Segura-Cox D. M. et al., 2020 *Nature*, 586, 7828, 228.
- Shakura N. I. and Sunyaev R. A., 1973 *A&A*, 500, 33.
- Shi J.-M. and Chiang E., 2014 *ApJ*, 789, 1, 34.
- Shi J.-M. et al., 2012 *ApJ*, 749, 2, 118.
- Shu F. H., 1977 *ApJ*, 214, 488.
- Shu F. H., 2016 *ARA&A*, 54, 667.
- Shu F. H. et al., 1993 *Icarus*, 106, 1, 92.
- Sierra A. et al., 2019 *ApJ*, 876, 1, 7.
- Simon J. B. and Armitage P. J., 2014 *ApJ*, 784, 1, 15.
- Simon J. B. et al., 2012 *MNRAS*, 422, 3, 2685.
- Simon M. et al., 2017 *ApJ*, 844, 2, 158.
- Sirono S.-i., 2011 *ApJ*, 735, 2, 131.
- Sirono S.-i. and Ueno H., 2017 *ApJ*, 841, 1, 36.
- Smallwood J. L. et al., 2020 *MNRAS*, 494, 1, 487.
- Smallwood J. L. et al., 2021 *ApJL*, 907, 1, L14.
- Speedie J. et al., 2022 *arXiv e-prints*, arXiv:2203.00692.
- Spiegel D. S. and Burrows A., 2012 *ApJ*, 745, 2, 174.
- Stammler S. M. et al., 2017 *A&A*, 600, A140.
- Steinpilz T. et al., 2019 *ApJ*, 874, 1, 60.
- Stoll M. H. R. et al., 2017 *A&A*, 599, L6.
- Strom K. M. et al., 1989 *AJ*, 97, 1451.
- Sturm J. A. et al., 2020 *A&A*, 643, A92.
- Suriano S. S. et al., 2018 *MNRAS*, 477, 1, 1239.
- Suriano S. S. et al., 2019 *MNRAS*, 484, 1, 107.
- Surville C. and Barge P., 2015 *A&A*, 579, A100.
- Suzuki T. K. and Inutsuka S.-i., 2014 *ApJ*, 784, 2, 121.
- Suzuki T. K. et al., 2016 *A&A*, 596, A74.
- Szulágyi J. and Ercolano B., 2020 *ApJ*, 902, 2, 126.
- Szulágyi J. et al., 2019 *MNRAS*, 487, 1, 1248.
- Takahashi S. Z. and Inutsuka S.-i., 2014 *ApJ*, 794, 1, 55.
- Takahashi S. Z. and Inutsuka S.-i., 2016 *AJ*, 152, 6, 184.
- Takahashi S. Z. and Muto T., 2018 *ApJ*, 865, 2, 102.
- Takahashi S. Z. et al., 2016 *MNRAS*, 458, 4, 3597.
- Takeuchi T. and Lin D. N. C., 2002 *ApJ*, 581, 2, 1344.
- Tang Y.-W. et al., 2017 *ApJ*, 840, 1, 32.
- Tanga P. et al., 1996 *Icarus*, 121, 1, 158.
- Teague R. et al., 2018a *ApJL*, 860, 1, L12.
- Teague R. et al., 2018b *ApJ*, 868, 2, 113.
- Teague R. et al., 2018c *ApJ*, 864, 2, 133.
- Teague R. et al., 2019 *ApJL*, 884, 2, L56.
- Teague R. et al., 2021 *ApJ*, 922, 2, 139.
- Testi L. et al., 2014 *Protostars and Planets VI* (H. Beuther, R. S. Klessen, C. P. Dullemond, and T. Henning), p. 339.
- Testi L. et al., 2022 *arXiv e-prints*, arXiv:2201.04079.
- Thalmann C. et al., 2016 *ApJL*, 828, 2, L17.
- Tominaga R. T. et al., 2018 *PASJ*, 70, 1, 3.
- Tominaga R. T. et al., 2019 *ApJ*, 881, 1, 53.
- Tominaga R. T. et al., 2021 *ApJ*, 923, 1, 34.
- Toomre A., 1964 *ApJ*, 139, 1217.
- Tremaine S., 2001 *AJ*, 121, 3, 1776.
- Tsukagoshi T. et al., 2016 *ApJL*, 829, 2, L35.
- Turner N. J. et al., 2014 *Protostars and Planets VI* (H. Beuther, R. S. Klessen, C. P. Dullemond, and T. Henning), p. 411.
- Ubeira Gabellini M. G. et al., 2019 *MNRAS*, 486, 4, 4638.
- Ueda T. et al., 2021 *ApJL*, 914, 2, L38.
- Ulrich R. K., 1976 *ApJ*, 210, 377.
- Urpin V. and Brandenburg A., 1998 *MNRAS*, 294, 3, 399.
- Uyama T. et al., 2018 *AJ*, 156, 2, 63.
- Uyama T. et al., 2020a *AJ*, 159, 3, 118.
- Uyama T. et al., 2020b *ApJ*, 900, 2, 135.
- van der Marel N. et al., 2013 *Science*, 340, 6137, 1199.
- van der Marel N. et al., 2016 *ApJ*, 832, 2, 178.
- van der Marel N. et al., 2019 *ApJ*, 872, 1, 112.
- Varnière P. and Tagger M., 2006 *A&A*, 446, 2, L13.
- Verrier P. E. and Evans N. W., 2009 *MNRAS*, 394, 1721.
- Villenave M. et al., 2020 *A&A*, 642, A164.
- Vorobyov E. I. and Basu S., 2005 *ApJL*, 633, 2, L137.
- Vorobyov E. I. et al., 2020 *A&A*, 638, A102.
- Wada K. et al., 2009 *ApJ*, 702, 2, 1490.
- Wafflard-Fernandez G. and Baruteau C., 2020 *MNRAS*, 493, 4, 5892.
- Wagner K. et al., 2015 *ApJL*, 813, 1, L2.
- Wagner K. et al., 2018 *ApJL*, 863, 1, L8.
- Walsh C. et al., 2017 *A&A*, 607, A114.
- Wardle M., 2007 *Ap&SS*, 311, 1-3, 35.
- Watanabe S.-i. and Lin D. N. C., 2008 *ApJ*, 672, 2, 1183.
- Weber P. et al., 2019 *ApJ*, 884, 2, 178.
- Weidenschilling S. J., 1977a *MNRAS*, 180, 57.
- Weidenschilling S. J., 1977b *Ap&SS*, 51, 1, 153.
- Whipple F. L., 1972 *From Plasma to Planet* (A. Elvius), p. 211.
- Wölfer L. et al., 2021 *A&A*, 648, A19.

- Wu Y. and Lithwick Y., 2021 *ApJ*, 923, 1, 123.
Xiang-Gruess M. and Papaloizou J. C. B., 2013 *MNRAS*, 431, 2, 1320.
Xie C. et al., 2021 *ApJL*, 906, 2, L9.
Xu W. and Kunz M. W., 2021a *MNRAS*, 502, 4, 4911.
Xu W. and Kunz M. W., 2021b *MNRAS*, 508, 2, 2142.
Yang C.-C. and Johansen A., 2014 *ApJ*, 792, 2, 86.
Yang C.-C. and Zhu Z., 2021 *MNRAS*, 508, 4, 5538.
Yang C. C. et al., 2017 *A&A*, 606, A80.
Yen H.-W. et al., 2019 *ApJ*, 880, 2, 69.
Youdin A. N., 2011 *ApJ*, 731, 2, 99.
Youdin A. N. and Goodman J., 2005 *ApJ*, 620, 1, 459.
Youdin A. N. and Lithwick Y., 2007 *Icarus*, 192, 2, 588.
Yu S.-Y. et al., 2019 *ApJ*, 877, 2, 100.
Yun H. G. et al., 2019 *ApJ*, 884, 2, 142.
Yun H.-G. et al., 2022 *arXiv e-prints*, arXiv:2209.05417.
Zanazzi J. J. and Lai D., 2018 *MNRAS*, 473, 1, 603.
Zapata L. A. et al., 2020 *ApJ*, 896, 2, 132.
Zhang K. et al., 2015 *ApJL*, 806, 1, L7.
Zhang K. et al., 2021 *ApJS*, 257, 1, 5.
Zhang S. and Zhu Z., 2020 *MNRAS*, 493, 2, 2287.
Zhang S. et al., 2018 *ApJL*, 869, 2, L47.
Zhu Z., 2019 *MNRAS*, 483, 3, 4221.
Zhu Z. and Baruteau C., 2016 *MNRAS*, 458, 4, 3918.
Zhu Z. and Stone J. M., 2014 *ApJ*, 795, 1, 53.
Zhu Z. and Stone J. M., 2018 *ApJ*, 857, 1, 34.
Zhu Z. and Zhang R. M., 2022a *MNRAS*, 510, 3, 3986.
Zhu Z. and Zhang R. M., 2022b *MNRAS*, 510, 3, 3986.
Zhu Z. et al., 2012a *ApJ*, 746, 1, 110.
Zhu Z. et al., 2012b *ApJL*, 758, 2, L42.
Zhu Z. et al., 2015a *ApJ*, 801, 2, 81.
Zhu Z. et al., 2015b *ApJ*, 813, 2, 88.
Zhu Z. et al., 2019 *ApJL*, 877, 2, L18.
Zurlo A. et al., 2020 *A&A*, 633, A119.